To the Graduate Council:

I am submitting herewith a dissertation written by Guanghe Liang entitled "A Study of the Atomistic Details of Structure and Dynamics of Polymethylene Crystals via Molecular Dynamics Simulations." I have examined the final copy of this dissertation for form and content and recommend that it be accepted in partial fulfillment of the requirements for the degree of Doctor of Philosophy, with a major in Chemistry.

Bernhard Wunderlich, Major Professor

We have read this dissertation
and recommend its acceptance:

Craig E Barnes

John H Shibata

Donald W Noid

Accepted for the Council:

Associate Vice Chancellor
and Dean of The Graduate School

# A Study of the Atomistic Details of Structure and Dynamics of Polymethylene Crystals via Molecular Dynamics Simulations

A Dissertation Presented for the
Doctor of Philosophy Degree

The University of Tennessee, Knoxville

Guanghe Liang

August, 1993

# DEDICATION

This dissertation is dedicated to my parents

Mr. Shengwei Liang

and

Mrs. Yuyan Lai

who have been giving me unlimited love and

invaluable educational opportunities

# ACKNOWLEDGEMENTS

I am deeply grateful to my major professor Dr. Bernhard Wunderlich for providing me the wonderful opportunities and guidance in this education. It is my honor to acknowledge my great indebtedness to him for his dexterous advice, making invaluable suggestions and constructive criticisms, and taking great pains in correcting my papers throughout this study. It is my proud privilege to express my great gratitude to my advisor Dr. Donald W. Noid who has guided me with great patience, given me incessant encouragement and ebullient inspiration, provided me monetary support, taught me wide knowledge from classical mechanics to chaos dynamics and from computer programming to molecular dynamics simulations, and made my dream of being able to do theoretical studies come true. Words cannot express my full gratitude to him. I would like to thank the other committee members, Dr. Craig E. Barnes, Dr. Roberto S. Benson, and Dr. John H. Shibata, for their comments and assistance over the past several years. I feel honored and obliged to Dr. John H. Shibata for his special encouragement and assistance besides this study in the past six years. I would also like to thank Dr. Bobby G. Sumpter of the Chemistry Division at Oak Ridge National Laboratory, for his important help throughout this research. I would like to thank Mr. Ross Toedte of the Visualization Lab, Computing and Telecommunication Division, Oak Ridge National Laboratory, and Mr. Mark Spining of the Computer Science Department at the University of Tennessee in Knoxville, for their help in the animation process used in this work. I would also like to thank Ms. Gail Wauford, our Computing Consultant at the University of Tennessee in Knoxville, for her

excellent computing assistance. I would finally like to thank the Chemistry Department of the University of Tennessee in Knoxville for providing the financial aid via an initial Teaching Assistantship, and the US Department of Energy and the National Science Foundation for research funds. There are many colleagues, friends, and well-wishers who have helped me and given me cheerful inspiration. The paucity of space does not permit me to mention them, but I will never forget. Last, but not least, I would like to express my sincere appreciation to my wife Rong Yang and my son Timothy Berean Liang, and my brothers and sisters and other family members in China, for their patience, understanding, and strong support.

# ABSTRACT

A series of molecular dynamics simulations on a supercomputer of the molecular motion of pentacontylene ($-C_{50}H_{100}-$) crystals containing 9600 (implicit hydrogen model) to 28,800 (explicit hydrogen model) atoms have been carried out for different temperatures and under various conditions of constraint. Bending, stretching, and torsional motions are allowed in these simulations. Such a system is sufficiently large to serve as a model of a macroscopic crystal. It can also serve as a model for polyethylene. The details in trajectory analyses and the links between microscopic and macroscopic properties are described. Reasonable agreements with experimental data on density, defect concentration, heat capacity increase, melting temperature, and speed of sound have been reached. The large volume of detailed information of the structure and motion permits a new level of understanding. Information about the atomistic details of the structure and dynamics of these crystals, such as crystal appearance, pseudo-symmetric crystal structures, picosecond time-scale formation of conformational defects, collective twist of chains, mass transport, longitudinal and transverse vibration of the crystal, dynamic multi-domains, and the beginning of the melting process at instantaneous superheating, is presented. Chaos in the polymethylene crystals and the applicability of potential functions for explicit hydrogen interactions are also discussed.

## TABLE OF CONTENTS


CHAPTER PAGE

1. Introduction . . . . . 1

1.1 Physical Properties and Structures of Paraffins . . . . . 3

1.2 Physical Properties and Structures of Polymethylene . . . . . 7

1.3 Dynamic Disorder in Paraffin and Polyethylene Crystals and Defect Theories . . . . . 9

Point Defects . . . . . 11
Kink Defects . . . . . 12
Twist Defects . . . . . 13
Soliton or Twiston Explanations . . . . . 14
Experimental Studies . . . . . 15
Computer Modeling and Simulations . . . . . 17

2. Theoretical Background and MD Simulation Methods . . . . . 21

2.1 Molecular Dynamics Simulations . . . . . 22

2.1.1 Classical Mechanics Formulation . . . . . 23

2.1.1.1 Newtonian Mechanics . . . . . 24
2.1.1.2 Lagrangian Mechanics . . . . . 24
2.1.1.3 Hamiltonian Mechanics . . . . . 26

2.1.2 The Potential Energy Functions and Simulation Models . . . . . 27

2.1.2.1 Model A . . . . . 28
2.1.2.2 Model B . . . . . 29
2.1.2.3 Model C . . . . . 30
2.1.2.4 Model D . . . . . 30

2.1.3 Algorithms . . . . . 31

2.2 Links Between Microscopic and Macroscopic Properties ..... 32

2.2.1 Statistical Ensembles and Thermodynamic Properties ..... 33

2.2.2 Radial Distribution Function and Structures ..... 35

2.2.3 Crystal Vibrational Spectra and Frequency Distribution Function ..... 38

2.2.3.1 Normal Mode Approximation ..... 39
2.2.3.2 Einstein Approximation ..... 41
2.2.3.3 Debye Approximation ..... 42
2.2.3.4 Lattice Dynamics and Dispersion Curves ..... 45

2.3 Visualization and Animation ..... 46

3. The Hexagonal Structure of Unconstrained Polymethylene Crystals ..... 48

3.1 Results ..... 50

3.2 Discussions ..... 56

3.2.1 Steady States ..... 58

3.2.2 Disorder, Gauche Defects, and Chain Dynamics ..... 60

3.2.3 Distribution of Lattice Parameters and Multi-domain Structures ..... 62

3.3 Conclusions ..... 64

4. Atomistic Details of Disordering Processes in Superheated or constrained Polymethylene Crystals ..... 65

4.1 Results ..... 66
4.2 Discussions ..... 69
4.3 Conclusions ..... 76

5. Dielectric Relaxation and Defect Motion in Polymethylene Crystals ..... 78

5.1 Results ..... 80
5.2 Discussions ..... 81
5.3 Conclusions ..... 84

6. Dynamics and Structure Simulation of Polymethylene Crystals with Explicit Hydrogen Atoms ..... 85

6.1 Results ..... 86
6.2 Discussions ..... 88
6.3 Conclusions ..... 90

7. Chaos in a Polymethylene Crystal ..... 92

7.1 Results ..... 95
7.2 Discussions ..... 96
7.3 Conclusions ..... 97

8. Concluding Remarks ..... 98

References ..... 108

Appendices ..... 120

Appendix A: Figures ..... 121
Appendix B: Summary on Experimental Gauche Bond Determination ..... 141
Appendix C: Tables ..... 152
Appendix D: A Fortran Program for the Calculation of Crystal Lattice Parameters ..... 170
Appendix E: A Fortran Subroutine to Generate Atom Coordinates in initial Crystals ..... 177

Vita ..... 185

## LIST OF TABLES


TABLE PAGE

1. Force field parameters for the united-atom simulations . . . . . 152

2. Computer simulation units and conversion to SI units . . . . . 152

3. Average density and *gauche* concentration as functions of time and temperature. . . . . 153

4. Standard deviations of the positions of the $CH_2$-groups in nm as a function of temperature . . . . . 153

5. Lattice parameters as functions of initial structure and temperature . . . . . 154

6. Lattice parameters (Run 8: MONO, 234 K) as a function of time (ps) . . . . . 155

7. Time and temperature range in the simulations of superheated and constrained crystals . . . . . 156

8. The lattice parameters of a four-side-constrained ORTH crystal (Run S14 in Table 7) as a function of time . . . . . 157

9. Flipping time (ps) of the dipole in various conditions . . . . . 158

10. Temperature, density, and *gauche* concentration as a function of time in the full atom simulations . . . . . 159

11. Time averaged volume and densities calculated with two different methods . . . . . 160

12. Standard deviations (nm) from initial structure in the full atom simulations . . . . . 160

13. Lattice parameter distributions as a function of time in the full atom simulation XR01 . . . . . 161

14. Lattice parameter distribution as a function of time in the full atom simulation XR02 ..... 162

15. Lattice parameter distribution as a functions of time in full atom simulation XR04 ..... 163

16. Location of *gauche* bonds in the crystal of XR04 at different times ..... 164

## LIST OF FIGURES


FIGURE PAGE

1. The 2-D lattice representations (a) and the initial crystal structures (b). In (b), each cross represents the carbon position and each chain contains 50 $CH_2$-groups. . . . . 121

2. Fluctuation of temperature as functions of time and initial crystal structure . . . . . 122

3. Concentration of *gauche* bonds as a function of temperature. The simulations are given by circles and the IR measurement by the squares (from ref. 35). . . . . 122

4. Fluctuation of density as functions of time and initial structure . . . . . 123

5. Radial distribution function of MONO crystal versus time . . . . . 123

6. Radial distribution functions at different temperatures and initial structures . . . . . 124

7. Structures of the MONO crystal in the *x*-*y* projection at different temperatures after 10 ps of simulation . . . . . 124

8. Structure of the MONO crystal in the *x*-*z* projection at 10 ps and 234 K . . . . . 125

9. Structure of the MONO crystal in the *y*-*z* projection at 10 ps and 234 K . . . . . 125

10. The time evolution of the dynamics of the center chain in the MONO crystal at T = 316 K from 0 to 10 ps . . . . . 126

11. The dynamics and coupling of chain motion in a surface layer of the MONO crystal at 403 K . . . . . 126

12. The positional difference of each atom in a MONO crystal taken from time averaged coordinates (between 5 and 10 ps) at 234 K and initial coordinates. The abscissa represents the number of the atom, and the ordinate represents the difference in *x* (a), *y* (b), and *z* (c) dimension . . . . . 127

13. Histogram of lattice parameter of the MONO crystal at 234 K (steady-state average between 5 and 10 ps) ..... 127

14. Lattice parameters as functions of lattice position *n* under the same condition as Figs. 12 and 13 ..... 128

15. Temperature and density as a function of time in the unconstrained crystals. Solid line: ORTH (Run D05 in Table 7), dotted line: MONO (Run D10 in Table 7) ..... 128

16. The *x*-*y* projection of the unconstrained ORTH as functions of time and temperature (Run D05 in Table 7) ..... 129

17. The *x*-*y* projection of the unconstrained MONO as functions of time and temperature (Run D10 in Table 7) ..... 129

18. The orientation of molecules in a single layer in the *x*-*y* projections (ORTH: Run D05 in Table 7, MONO: Run D10 in Table 7) ..... 130

19. Shift of the 9600 $CH_2$-units in the unconstrained ORTH crystal after 100 ps simulation at 332 K (Run D05 in Table 7). (Note that after 400 steps one layer is completed) ..... 130

20. The *x*-*y* projections of 4-SC ORTH crystal (Run S14, 340–227 K in Table 7), (a) after 10 and (b) after 66 ps of simulations ..... 131

21. The *x*-*y* projections of 3-SC MONO crystal (Run S11, 442–255 K in Table 7), (a) after 5 and (b) after 100 ps of simulations ..... 131

22. The *x*-*y* projection of 3-SC MONO crystal (Run S12 in Table 7) after 100 ps of simulation (144 K) ..... 132

23. The *x*-*z* projection of the dynamic chains in the eighth layer of 4-SC MONO crystal (Run S10 in Table 7) after 10 ps of simulation ..... 132

24. Average setting angle in the MONO crystal at 316 K (Run 9 in Table 3) after 5 ps of simulation ..... 133

25. Average setting angle in the MONO crystal at 316 K (Run 9 in Table 3) after 10 ps of simulation ..... 133

26. Schematical illustration for various types of defects found in the simulations ..... 134

27. Center of mass coordinates (solid line: $x$, dotted line: $y$, dash line: $z$) of the center chain in the MONO crystal at 316 K (Run 9 in Table 3) as a function of time ..... 134

28. End-to-end distance of the center chain (solid line) and the edge chain (dotted line) in the MONO crystal at 316 K (Run 9 in Table 3) as a function of time ..... 135

29. Radial distribution function versus time (from the bottom to the top: 0, 2, 3, 4, and 5 ps) in the simulation XR01 (Table 10) ..... 135

30. Radial distribution function versus time (from the bottom to the top: 0, 5, 6, 7, 8, 9, and 10 ps) in the simulation XR02 (Table 10) ..... 136

31. Radial distribution function versus time (from the bottom to the top: 0, 2, 3, 4, 5, 6, and 7 ps) in the simulation XR04 (Table 10) ..... 136

32. The $x$-$y$ projection of the crystal at 112 K after 5 ps of simulation in the run XR01 (Table 10) ..... 137

33. The $x$-$y$ projection of the crystal at 247 K after 6 ps of simulation in the run XR02 (Table 10) ..... 137

34. The $x$-$y$ projection of the crystal at 309 K after 7 ps of simulation in the run XR04 (Table 10) ..... 138

35. Lattice parameter distribution in the ORTH crystal at 309 K after 7 ps of simulation in the run XR04 (Table 10) ..... 138

36. Average setting angle in the crystal at about 310 K (Run XR04 in Table 10) after 2 (a) and 7 (b) ps of simulations ..... 139

37. The $x$-$z$ projection of the surface layer in the crystal at about 310 K (Run XR04 in Table 10) as a function of time (left: after 2 ps, right: after 7 ps) ..... 139

38. The $x$-$z$ projection of the center layer in the crystal at about 310 K (Run XR04 in Table 10) as a function of time (left: after 2 ps, right: after 7 ps) ..... 140

39. Trajectory separation as a function of time ..... 140

# CHAPTER 1

# INTRODUCTION

Knowledge about molecular motion is fundamental for the understanding of mechanisms of many dynamic processes in polymeric materials. The link between macroscopic properties of matter and the microscopic nature of molecular motion on an atomic level, which are in a nanometer length scale and a picosecond time scale, is an important issue of recent materials research. Experimental techniques such as electron microscopy, X-ray diffraction, and neutron scattering are, however, of limited use in the elucidation of molecular dynamics. Computer simulation techniques have recently offered hope for progress in this field.

Molecular Dynamics (MD) is a computer simulation technique using classical mechanics[1] to study the dynamic and structural behavior of systems on a molecular or atomic level. There are two other major computer simulation techniques, *Monte Carlo* and *Molecular Mechanics*, but only MD can provide direct, realistic time-dependent results. The MD technique was first developed in the late 1950s by *Alder* and *Wainwright* for the study of phase transitions in hard sphere liquids.[2] Since then, the fundamental applications of the MD simulation has expanded.[3] There have been many reviews on the development and application of MD simulations.[4–11] In the past few years, it has been demonstrated that MD simulation is a very useful technique in polymer research.[12–20]

Paraffins and polyethylene (PE) form a homologous series of hydrocarbons, and their crystal structures and dynamic properties are related. In addition, the study of paraffins

and PE offers a model for other polymers. Furthermore, a general knowledge of dynamic and structural properties of paraffins and PE is fundamental to understanding the behavior of many systems, such as biomembranes and micelles,[21,22] liquid crystals,[23,24] and crystals and mesophases.[25–34] Currently, many details of the dynamics and structure of PE still remain unclear, such as polymorphic phase transitions, defect formation, and the melting process.

Due to the simplicity of the structure and the well known potential energy function, polymethylene, $(-CH_2)_n$, has been a very useful candidate in simulations for the model of paraffins and PE[12–20] and it will serve as our model in the simulations presented in this dissertation. Although the terminal methyl groups will affect the type of packing of paraffins in crystals, this effect will become negligible as the molecular mass increases, especially when one places the focus on the study of the general dynamics of $CH_2$-sequences and the packing in terms of subcell units.

This dissertation involves MD simulations of polymethylene crystals with the aim to further the understanding of the dynamics and structure of paraffins and PE crystals at different temperatures and various conditions of constraint. In this chapter, the literature on the subjects of structure and dynamics of paraffin and PE crystals will be reviewed. The theoretical background and methods of MD simulations will be summarized in the next chapter, and the results will be presented and discussed in Chapters 3–7. Chapter 8 will list the conclusions drawn from this dissertation work.

## 1.1 PHYSICAL PROPERTIES AND STRUCTURES OF PARAFFINS

Paraffins, or paraffinic hydrocarbons, are named after the Latin *parum affinis* (meaning "little affinity" or "little reactivity") for alkanes ($C_nH_{2n+2}$) or cycloalkanes ($C_nH_{2n}$) which are saturated hydrocarbons consisting of only carbon and hydrogen atoms. Substances containing mixture of various paraffins of sufficient length are called paraffin waxes and are solid at ambient temperature. Linear, unbranched paraffins are called normal or *n*-paraffins. In this dissertation the paraffins mentioned are all normal paraffins unless explicitly indicated otherwise.

At room temperature and atmospheric pressure, the normal paraffins butane ($C_4$, b.p. 273 K) and smaller are gases; those between pentane ($C_5$, b.p. 309 K) and heptadecane ($C_{17}$, m.p. 295 K) are liquids; octadecane ($C_{18}$, m.p. 301 K) and those containing more then 18 carbons are solids. The highest molecular mass, naturally occurring alkane that was isolated in pure form is hectane ($C_{100}H_{202}$, M.P. 388 K).[32] Longer chain normal paraffins have been synthesized for polymer modelling. For example, $C_{192}H_{386}$ can be synthesized by the hydrogenation of acetylene compounds catalyzed by Pd/C.[35] Solid paraffins always are crystalline. In those with carbon numbers between 8 and 50, there is an odd-even alternation effect in melting points and heat capacities.[31,34] A branched-chain isomer has a lower melting point than its straight-chain counterpart. The density increases with size, but tends to level-off at about 0.8.

In hydrocarbon molecules, different arrangements of atoms can be given by the rotation of carbon-carbon bonds. These arrangements of atoms that can be converted into one another by rotating about single bonds are called *conformations*. Due to van der

Waals repulsion and intrinsic energetics, there are barriers for the rotation of carbon-carbon bonds and the energy required to overcome a rotational barrier is called *torsional energy*. In the Newman projection, the arrangements with all groups in closest proximity are called *eclipsed conformations* and are unstable; the arrangements with groups 60° rotated are called *staggered conformations* and have potential energy minima; and those intermediate conformations are said to be in *skewed conformations* with various amounts of *torsional strain.*[36] In *staggered* conformations, as in the case of butane, there is one *anti* (or *trans*) conformation in which the two alkyl groups are 180° rotated to a zig-zag conformation (dihedral angle 180°) and two *gauche* conformations in which the two alkyl groups are 60° rotated. Both *anti* and *gauche* conformation are free of torsional strain, but the *anti* conformation in butane is more stable by 3.35 kJ/mol than the *gauche* conformation.[36] Changing from the *anti* to the *gauche* conformation requires 14.23 kJ/mol of torsional energy to overcome the non-*cis eclipsed* barrier, and changing from one *gauche* to another by the way of passing the *cis eclipsed* conformation requires 18.41–25.52 kJ/mol which makes their path less likely.[36]

The study of the detailed structure of crystalline paraffins began in the 1920s with the X-ray diffraction method.[37] The chain structure of paraffins in crystals is best summarized as follows:[21] in the most stable state, the paraffin chain forms an all-*trans*, planar zig-zag; the carbon-carbon bond length is 0.1533 nm (similar to the carbon-carbon distance in diamond); the carbon-carbon bond angle is about 112°; the distance between every other carbon atom along the zig-zag is 0.254 nm (which is the *c*-dimension in the unit cell of paraffins).

The X-ray diffraction studies found that paraffin crystals pack with specific chain interactions (often noted as β phases in the literature[31]): 1. orthorhombic, in which the molecular axes are normal to the basal plane defined by the positions of the terminal methyl groups; 2. triclinic, the molecular axis is tilted by about 73° with respect to a basal plane defined by the position of methyl groups[31] and the subcell is triclinic; and 3. monoclinic, in which chains are tilted by approximately 61° with respect to the basal plane defined by the methyl groups and the subcell is orthorhombic.[31] At higher temperatures, paraffin crystals can also form a fourth packing with non-specific chain interactions (noted as α phases[31]). These are hexagonal or pseudohexagonal, in which the hexagonal packing has no setting-angle (the angle between the zig-zag plane and the *a*-axis of the lattice) restriction while the pseudohexagonal packing has a similar packing as the orthorhombic crystal with a limited degree of zig-zag planar rotation.[21] Figure 1a* illustrates the orthorhombic, monoclinic, and hexagonal unit-cell packing viewed along the chain axis. In Fig. 1a the small open and filled circles represent the $CH_2$ groups and the large open circle in the hexagonal packing indicates that the zig-zag plane can rotate freely about its chain axis. Besides these basic structures, a variety of chain packing with so-called hybrid lattices have been suggested.[40]

The form of chain packing of paraffins is chemical structure, temperature, and pressure dependent.[38–46] Even-numbered paraffins and odd-numbered behave differently with respect to packing because of their overall different molecular symmetry.[21] In general, all odd-numbered paraffins have an orthorhombic packing, even-numbered

*All figures are shown in the Appendix A.

paraffins with 24 carbons and below are triclinic, and $C_{26}$ and higher mass even-numbered ones are monoclinic.[32,34] The packing also depends on the purity of the sample. For example, in the presence of about 2% impurities of neighboring homologs in the sample, the hexatriacontane ($C_{36}$) may have orthorhombic structure.[46]

In all tightly packed crystal structures of paraffins, the area perpendicular to the chain is about 0.189 $nm^2$ per $CH_2$-group and the mean volume per $CH_2$-group is about 0.024 $nm^3$. The mean area perpendicular to the chain and the mean volume per $CH_2$-group for hexagonal or pseudohexagonal paraffins are $\approx$0.20 $nm^2$ and $\approx$0.025 $nm^3$, respectively, and for liquid paraffins are $\approx$0.23 $nm^2$ and $\approx$0.0295 $nm^3$, respectively. A corresponding, abrupt volume increase can be observed in the phase transitions.[21]

The even-numbered paraffins from $C_{22}$ to $C_{44}$ and the odd-numbered paraffins from $C_9$ to $C_{43}$ show hexagonal or pseudohexagonal phases in a narrow temperature below ultimate melting.[31] In the hexagonal or pseudohexagonal crystals the chain packing is less dense and specific chain-chain interaction is lost due to disorder of the $CH_2$-groups. This type of packing may exist as a stable state at higher temperatures than the more tightly packed phases, or as a supercooled metastable state on cooling from the molten state at temperatures below the melting of the more tightly packed phases.[21]

X-ray diffraction data indicate that as temperature increases there are distinct changes in the two-dimensional lattice parameters *a* and *b* corresponding to differential scanning calorimetry (DSC) curves in phase transitions.[47–50] In the tightly packed crystal structures, the dimensions of *a* and *b* change little with temperature. In the pseudohexagonal phases, the dimension *a* (of the orthorhombic lattice) increases, but *b* (of the orthorhombic lattice)

decreases as temperature increases in a rate such that the ratio *a*/*b* increases to, but remains less than $3^{1/2}$, and reaches $3^{1/2}$ in true hexagonal phases. The solid-solid phase transitions are also called premelting. The word premelting may mean a gradual change without transitions or a small transition before melting, but it is customarily referred to the latter.[33] Some paraffins, such as $C_{25}$–$C_{29}$, have more than two solid-solid phase transitions[51], whereas paraffins, such as $C_{44}$, $C_{50}$, and $C_{60}$, do not show premelting.[33,52] However, longer chain paraffins, such as $C_{80}$,[53], $C_{94}$,[52], $C_{100}$,[54] $C_{192}$,[35] and $C_{246}$ have been observed to undergo premelting transitions.[55]

## 1.2 PHYSICAL PROPERTIES AND STRUCTURES OF POLYETHYLENE

Expressed by the smallest repeating unit, $(CH_2–)_n$, polyethylene (PE, source-based name) has the same structural formula as poly(methylene) (structure-based name). Commercially available PE has typical value for *n* from 800 to 100,000. PE has been the largest-volume commercial polymer in the world. In 1989, the PE outputs were $22{,}894.0\times10^6$ tons worldwide and $7{,}319.9\times10^6$ tons in the US (Industrial Statistics Yearbook 1989, Vol. II, United Nations, New York, 1991). PE forms a partially crystalline solid, made up of regions of small crystals, called crystallites, embedded in an amorphous matrix. The smallest crystalline units are lamellae, which when crystallized in bulk which consist of chains that are perpendicular to the small dimension and fold back and forth. A PE lamella usually has dimension of 5–20 nm. The density of 100% crystalline PE is calculated from X-ray data to be 1.00 $Mg/m^3$ and that of amorphous PE is ≈0.855 $Mg/m^3$. Linear PE has often a crystallinity of 70–90% with a density of

0.957–0.986 g/cm$^3$.[56]

The only stable crystal form for PE is orthorhombic.[57,58] In these crystals, the zig-zag planes of neighboring chains are in approximately mutually perpendicular orientation (setting angle, the angle between the zig-zag plane of chain and the *bc* plane of the crystal lattice varying between 41.2°–48.8° for differently grown crystals).[59–62]

The study of the thermal expansion of orthorhombic PE shows that the primary change occurs along the *a* axis ($a$ = 0.7414 nm at 303 K and 0.7706 nm at 411 K).[60] The *b* and *c* axes do not expand appreciably, in fact, the *c*-axis decreases in length. The ratio *a*/*b* is 1.46 at 77 K, 1.50 at 303 K, and 1.56 at 411 K. It never reaches $3^{1/2}$, the value corresponding to a hexagonal lattice, unless it is extrapolated to a temperature of about 514 K, which is far above the melting point.[58]

The X-ray diffraction studies[61] of melt-crystallized PE showed that the *a* and *b* lattice dimensions were independent of annealing time or crystallization temperature. The lattice dimension *c* was found also to be invariant with experimental conditions (308–402 K). Neutron scattering data[62] of the orthorhombic unit cell parameters *a*, *b*, *c* and the setting angle were 0.7121 nm, 0.4851 nm, 0.2548 nm and 41°, respectively, at 4 K (liquid He), and 0.7161 nm, 0.4866 nm, 0.2546 nm, and 41° at 90 K (liquid $N_2$).

The monoclinic phase of PE is metastable and can be found in deformed PE.[63] Below the melting point, the monoclinic phase transforms back to the orthorhombic form on annealing.[58] The monoclinic PE is similar to triclinic packing in paraffins, but has a mirror plane normal to the chain axis. According to Hermann-Mauguin's symbols, the symmetry of the monoclinic crystal is 2/*m* which means that there exists a twofold axis

and a mirror plane normal to it. Unlike monoclinic paraffin crystals, in the monoclinic PE the chain axis is *b* rather than *c* and the unit cell is doubled in the *a* direction. One may say that the monoclinic unit cell in PE consists of two triclinic unit cells. That is why it was earlier, before the added symmetry was detected, thought to be triclinic. The monoclinic crystal has a higher symmetry than the triclinic due to the existence of the mirror plane.[57] In paraffin crystals, the effect of methyl groups on packing makes triclinic and monoclinic packing distinguishable.

A pseudohexagonal structure in PE with orientational disorder due to a random arrangement of skeletal zig-zag planes about the chain axis was also suggested in 1953.[64a] The phase diagram shows that the hexagonal or pseudohexagonal phase of PE is stable only in a narrow region of high temperature (above 500 K) and high pressure (above 400 MPa) region.[27] To stabilize hexagonal PE at atmospheric pressure, the sample must be heated under sufficient constraint or contain defects caused by irradiation or copolymerization (with propylene, for example).[66b]

## 1.3 DYNAMIC DISORDER IN PARAFFIN AND POLYETHYLENE CRYSTALS AND DEFECT THEORIES

The dynamic disorder in crystals of chain molecules has become an important field of study.[65] In molecular crystals, conformational, rotational, and even diffusional motion can start at temperatures considerably below the melting or disordering transition.[27] Defect motion was thought to be responsible for many mechanical and dielectrical processes in polymers, such as the diffusion of polymer chains observed during deformation and annealing, the transfer of free volume, accommodation of structural

singularities, and the approach of reactive sites.[66]

The earliest defect model is the so-called "rotator phase" proposed by Müller[67] from X-ray diffraction studies on paraffins in which it was found that in the hexagonal phase, after a solid-solid phase transition there is an increase in the interchain distances. It was suggested that in the hexagonal or pseudohexagonal packing of paraffins the chains rotate freely about their long axis. Later studies indicate that the rotation of the chain as a whole does not readily occur and it was suggested that the motion may consist of discrete short vibrations about the axis of the molecules.[21,70] More recent studies suggest that the hexagonal or pseudohexagonal phase is a mesophase with dynamic conformational disorder, or a condis phase, but long-range positional and orientational order.[26,27]

The studies via the Advance THermal Analysis System (ATHAS)[69] found that the there is a significant increase in heat capacity in the range of stability of the hexagonal phase.[70] This heat capacity increase is considered to be due to the contribution of conformational disorder that could be discussed in terms of the commonly used "rotational isomeric states" model of linear macromolecules.[71-73] In this model, the defects are *gauche* conformation of higher energy, causing the measured heat capacity increase. On the basis of atomistic calculations, a detailed rotator model was analyzed for the condis phase of flexible macromolecules using a cooperative statistical treatment.[74] The introduction of *gauche* conformations into the backbone chain was thought to be responsible for the formation of the condis crystal and the transition from orthorhombic to condis phase is considered not to involve a reorientation of the molecular chains as a whole but segmental motion.[27] Various other defect theories have been previously

proposed. The following will summarize some related theoretical approaches and experimental measurements on defect.

**Point Defects**

A special point defect in polymers was suggested by Reneker and coworkers[75] in 1962 and is also called the Reneker defect.[25] This concept comes from the defect theories in metals. It is assumed that point defects can exist at any time in a polymer crystal at equilibrium concentrations. In the Reneker defect, a segment of a polyethylene chain is compressed at both ends causing a buckling of the chain at some localized position with the uncompressed region of the chain remaining in crystallographic register. The buckle is accommodated by a small distortion of the neighboring chains and results in twisting of the molecule by 180° about the chain axis with incorporating one additional methylene in the compressed region.

For the explanation of lamellar thickening, a point defect was assumed to form at a chain end and move along the chain. On reaching the chain fold, such motion would result in a length increase of the buckle segments joined at the fold by half a repeating distance. Further explanation of chain rotation is needed for relaxation processes and translation involved in lamellar thickening. More recent molecular mechanics calculation by Reneker *et al.*[76] proposed five types of defects for an isolated crystalline PE chain: two dispirations, two dislocations, one disclination, and three partial defects (two chain twist boundaries and a partial dislocation boundary which cannot exist alone but can combine to form a defect). The energy is computed to be 50–200 kJ/mol for the defects and

30–60 kJ/mol for the partial defects. Minimum energy calculations were performed on a model that includes 19 chains of $C_{60}H_{122}$. The end of the center chain that contains the defect is fixed at the orthorhombic lattice site and the other 18 chains are all-*trans* and fixed in orthorhombic positions. The excess energy is taken as the energy difference between the perfect crystal and the crystal containing the defect.

In the MD simulations presented in this dissertation, it was observed that the defects are largely delocalized and involve neighboring chains with cooperative motion.

**Kink Defects**

The kink model was developed by Pechhold in 1963.[79] One of the simplest kink defects in polyethylene is a 2g1 kink that is represented by the sequence of *gauche* conformations $g^+tg^-$ ($g^+$: $\tau = 300°$; $g^-$: $\tau = 60°$) and *trans* (t: $\tau = 180°$), where 2g represents the number of *gauche* conformations and the second numeral represents the amount of shortening of the chain in multiples of half of the *c* dimension of a subcell. It was suggested that disorder is achieved by the introduction of kink isomers into an ideal crystal. In this model some bonds are always away from their equilibrium positions, but the chains are essentially parallel, so that the largely extended low-energy macroconformation remains. A kink that reaches a neighboring lattice position is called a jog. The crystal melts when the kinks reach a certain critical concentration. In the melt, short-range order is usually observed which is explained in the kink model by assuming that the chains are still parallel.

The motion of kinks was used to propose a mechanism of lamellar thickening. As the temperature increases, the kinks produced do not ultimately disappear, rather, they are thermally activated and move through the crystal causing segmental diffusion. In addition, kinks might hop by changing from left-handed ($g^+tg^-$) to right-handed ($g^-tg^+$), giving rise to relaxation processes.

However, the major difference observed in the MD simulations in this dissertation research is that *kink* defects exist only on the surface of the crystal and in small amounts and they do not move along the chains.

**Twist Defects**

The properties of the twist defects, as is called "Utah twist",[66] were studied by conformational energy calculations based on the "rotation-translation-twist-tension" model (RT-TT) by Mansfield and Boyd,[25] to explain mechanical and dielectric relaxation in PE crystals.[78–80] The model has the following basis:[25]

> "1) The twist introduces 180° rotation of the stems relative to each other; 2) the twisted region is quite localized (in ≈12 $CH_2$ units); 3) the twisted region consists of a fairly uniform succession of only slightly twisted bonds (180° total/12 $CH_2$ = 11° twist/bond); 4) there is negligible shortening of the chain due to introduction of the twisted region; 5) the introduction of the 180° aggregate twist (without chain shortening) necessarily results in *translational* lattice mismatch in the stems; 6) the translational mismatch is localized on one side of the twisted region (*i.e.*, in one stem—the rotated one); 7) the twist propagates through the crystal rather smoothly with no evidence of a local hopping barrier; 8) in thick crystals, the crystal forces, as a result of the stem mismatch, produce a tension (or equally likely a compression) on the entire chain (both stems and twist region) gradually forcing the chain into lattice register far away from the twisted region; and 9) it is the translational mismatch of the stems that results in the strong dependence of activation free energy on crystal thickness or chain length."

In short, the model suggests that the PE molecule crystallizes in the all-*trans* planar zig-zag conformation. If a single three-carbon zig-zag unit is rotated through 180° about

its long axis and then translated by one half the unit cell dimension it will be returned to crystallographic register. The twisted region occupies about 12 $CH_2$ units, and the translational mismatch may extend over 100 $CH_2$ units.

The differences between Reneker defect and the Utah twist are that although both models involve relatively localized 180° twist, the latter is smooth instead of buckled and is only an intermediate state so that there are no equilibrium concentrations.

The shortcoming of the Utah twist model is that the twist motion is artificially regulated since all the reference chains are assumed to be static, resulting in the so-called crystallographic mismatch between the twisting chain and the static chains which give rise to a high defect energy. The results in this dissertation research show that the twist motion is irregular and coupled with neighboring chains.

**Soliton or Twiston Explanations**

Theoretically, the Utah twist motion was proposed to be the motion of a torsional wave which propagates along the chain through the crystal and moves the chain site by site within the crystal and was interpreted in term of solitons[81] or twistons.[82]

The word "soliton", coined by Zabusky and Kruskal[83] in 1965, is a brief notation for solitary waves which correspond to particular solutions of some nonlinear equations describing the propagation of excitations in continuous media with both dispersion and nonlinearity.[84] Solitons are special wave pulses which interact with one another so as to keep their identity and so they act as particles.[85] The solitons describing the collective motion and conformational defect in PE are termed twistons.[82] The concept of soliton has

been used to explain many new phenomena in different fields of physics and other sciences. For example, to explain thermal conductivity, a statistical mechanics theory based on weakly interacting solitons and phonons gave better results than a phonon-phonon interaction theory.[85] It has been possible to show that the flow of heat in solids is closely related to the flow of solitons.[85] In the study of strong interactions of phonons it was found that the phonons did not come to thermal equilibrium, but rather they underwent nearly periodic variations[86] which was explained in terms of solitons by Zabusky and Kruskal.[83] However, recent studies suggest that solitons are not necessary to explain this phenomenon.[85,87] In the more recent MD simulation of twist motion in PE crystals, it was suggested that in the polymer system, the chaotic dynamics may destroy coherent motion required for solitons.[66] The subject of soliton travelling through a material is still under development,[84,88-90] and involves nonlinear dynamics and chaos theory.[85]

In Chapter 7, the preliminary work on the characterization of chaos in the system is presented. The result suggests that the system is chaotic.

**Experimental Studies**

The IR and Raman spectroscopic measurements of *gauche* defects by Zerbi and coworkers support the kink model and suggest that the chains tilt at the end due to end *gauche* defects (the penultimate bond is *gauche*) and the interior of the crystal is ordered.[91] Different results were reported by Snyder and coworkers[33, 92-95] from their IR studies by which distribution of *gauche* defects along the chains were observed and the

disordering mechanism was suggested to involve longitudinal diffusion.[33] More details in *gauche* defect determination have been reviewed in the Appendix B.

Thermal analysis of hydrocarbons from paraffin to polyethylene in the solid state has been reported recently.[34] The results show that the heat capacity increase is in line with the gradual increase in conformational disorder.

Through the NMR study of $C_{32}H_{66}$, Olf *et al.*[96] interpreted "rotator phase" as a result of molecular motion coupled with longitudinal translation and rotation. All molecules in the crystal participate in the motion. The X-ray diffraction, neutron scattering, dielectric measurement, IR, Raman, and NMR spectroscopies studies of $C_{33}H_{68}$ by Strobl *et al.*[97–99] show that rotational disorder destroys the sublattice structure, in which the rotational 180° jump destroys the long range order of the zig-zag skeletal plane orientation, but preserves a short range order between 327.5 K and 338.5 K, screw jumps are superimposed which involve longitudinal shifts of the chains in between 338.5 K and 341 K, and there is an additional introduction of intrachain defects with diffusion along the chains between 341 K and the melting point (344.8 K).[97-99] The coupling of translational and rotational motion was also suggested.[99] Neutron scattering study of paraffins also indicate the substantial translational and rotational diffusion.[100–102] The results of X-ray diffraction, DSC, and IR spectroscopy studies by Ungar[103] indicate that all molecules are seen as being equivalent in the "rotator phase" by diffraction experiments which give information on the long-time/long-range average of molecular orientations, whereas the IR and Raman spectra show that all molecules are not equivalent in local arrangement in "rotator phase" because there is splitting in certain C–H vibration bands due to interaction between

nonequivalent neighbors. Ungar suggested that the "rotator phase" is a multiphase in which the average lattice is trigonal with a hexagonal subcell.[103] The nonequivalent molecules result in a crystal with different domains as has been observed in the X-ray diffraction, IR and Raman spectroscopy, and DSC measurements on a solid solution of heneicosane ($C_{21}$) and tricosane ($C_{23}$).[104] Each domain is ordered, encompassing tens of molecules in which each chain has only four equivalent orientations around its chain axis, and there is negligible conformational disorder.[105]

For the conformational defect in the high-pressure hexagonal phase of PE, no IR data are available so far. Rather, the defect concentration is usually estimated from the contraction along the chain axis during the orthorhombic-hexagonal transition, assuming the contraction is due to kink formation.[105] However, an attempt has been made before to relate the "rotator phase" in paraffin crystal to the high-pressure hexagonal phase of PE by bridging them with radiation-induced hexagonal PE.[105]

The results of MD simulations give a full picture of real time molecular motion and crystal structure in the picosecond time-scale. These results have been able to provide detailed information on the life-time and the exact position of a conformational defect which complement experimental measurements.

**Computer Modeling and Simulations**

The dynamics and defect structure in paraffin and PE crystals have been subjected to computer modeling and simulations, such as molecular mechanics calculations,[106,107] *Monte Carlo* simulations,[108–111] molecular dynamics simulations,[18,28,30,112–114],

conformational energy calculation of a single chain in cylindrical potentials,[115] soliton analyses,[82,88,90,116] and other calculations.[24,117]

The *Monte Carlo* simulations of paraffins by Yamamoto,[108,109] in which the chains are assumed to be rigid and all-*trans*, show that crystals in the "rotator phase" are composed of many more or less ordered domains within which the chains tend to be parallel to their zig-zag planes,[108] and the overall molecular motion in the "rotator phase" is described in terms of the movement of the boundaries of the ordered domains.[109] Ryckaert *et al.* carried out MD simulations with either periodic boundary conditions in the chain direction[30] or a bilayer crystal of tricosane, $C_{23}$, (30 chains in each layer). The molecular chains in the "rotator phase" have only four well-defined orientations (setting angles). The longitudinal translational diffusion and rotational diffusion are of the jump type and the former one occurs at lower temperature than the latter (the two types of motion are uncoupled from each other).[30,112] Note, that in their simulations, the bond lengths are fixed and the chains are rigid for rotation about their long axis. Other MD simulations have been carried out with molecular modeling software and are limited to single-chain dynamic simulations.[113]

In the last five years, more realistic models have been developed by Noid and coworkers.[19,20] These molecular dynamics (MD) techniques have been playing a significant role in our research group in the studies of atomistic details on the dynamics and structure of polymers. Many links have been made between microscopic and macroscopic properties of polymers, such as conformational disorder and heat capacities,[12,14,28] molecular motion and the vibrational spectrum,[13,118] stress-induced

frequency shift and conformational change,[3a,119] twist motion and α-relaxation,[66,120] molecular motion and lamellar thickening,[15,18,29] and melting processes of polyethylene crystals.[16-18] The results have also provided us with a better understanding of the correlation of rotational isomers and defect generation and motion in polyethylene crystals.[121]

This dissertation research is an extension of these MD simulations by our research group to larger sized models and longer times to study the atomistic details of the structure and dynamics of polymethylene crystals, to provide geometric and topological information on the molecular behavior in the phase transitions and the melting processes.

The model used throughout this dissertation research consist of 9600 $CH_2$-groups sitting in orthorhombic, monoclinic, and hexagonal crystal positions. The size of each crystal is about 227 $nm^3$, which can serve also as a reasonable model for a PE crystal (since the crystallization of high molecular weight molecules is kinetically hindered because of the random coiling of the molecule and entanglements, so that the initial crystals usually have dimensions of only 5 to 20 nm in the chain direction).[57] Stretching, bending, and torsional motion of the molecules are included in this realistic simulation. For the purpose of studying the phase transition, the simulations were carried out with different initial structures and at different temperatures. To investigate the dynamic nature of the molecules, unconstrained crystals have been simulated. Further studies have been carried out with various static shells surrounding the crystal in order to understand the effect of the constraint (and pressure). The simulations have been conducted in two ways, first with implicit hydrogens (*i.e.* by uniting the $CH_2$-groups into a single atom of

mass 14.03) and with explicit hydrogens enabling the full understanding of hydrogen effects. A total number of 25 simulation were carried out on the CRAY/X-MP supercomputer at Oak Ridge National Laboratory, and IMB/3090 and VAX/9000 supercomputers at the University of Tennessee using a total of about 1500, 1000, and 2400 hours of CPU time on the CRAY/X-MP, IBM/3090, and VAX/9000, respectively. An effort is made in this dissertation to establish a link between the molecular, picosecond time-scale large-amplitude motion to the macroscopic properties of paraffins, polyethylene, and polymers in general.

The MD computer programs used in this dissertation were written by Dr. D. W. Noid using new efficient programming strategies,[19,20] which enable these large scale simulations to run in reasonable wall-clock times (for a typical run of a model of 9600 $CH_2$-groups with implicit hydrogen interactions, there are 28,800 second order differential equations to be solved for each time step and 100 ps simulation required about 150 hours of CPU time on a Cray/X-MP; if the hydrogens are explicitly included, the time increases by a factor of about twenty).

Through these studies, a series of trajectories have been established and animated. A movie is available for viewing. Many of the results from the analyses of the trajectories are in good agreement with experimental observations. A new level of understanding of molecular behavior, dynamics and structure of nanophases, and the phase transitions has been achieved.

Before going to the details, it is necessary to introduce some basic theories and techniques involved in the MD simulations which will be done in Chapter 2.

# CHAPTER 2

# THEORETICAL BACKGROUND AND MD SIMULATION METHODS

Molecular dynamics (MD) simulations use a mathematical framework consisting of the fundamental laws of physics to numerically calculate by computer the time evolution of the model system in question.[122] The time evolution of the sufficiently large system as given by its trajectories and velocities or the dynamics of the constituent particles can then be interpreted and should be linked to the macroscopic properties.[10] The key issue is, thus, to connect the microscopically small analyzed system and short, picosecond time spans to the macroscopic materials in the experimental time that is often measured in seconds.

To construct a model, one must know the chemical structure of the molecules (the atoms, molecular structure, and bonding), the potential energies for bonding and nonbonding interactions, and external forces (if there are any, *e.g.* for deformation and non-equilibrium processes). Next, it is necessary to develop an efficient computer code using an algorithm to solve the equations of motion and to generate the trajectories or dynamics of the particles in times available on present-day supercomputer. Finally, the data must be interpreted for the description of the microscopic and macroscopic properties.

## 2.1 MOLECULAR DYNAMICS SIMULATIONS

In classical mechanical MD simulations, atoms making up the system are treated as the particles of motion and the laws governing the system are those of classical mechanics that can be written in the form of the Newtonian formulation, Lagrangian formulation, or Hamiltonian formulation.[1] Sometimes the basic equation of motion is taken to be the Langevin equation as well,[123] which uses Brownian motion theory to reduce the complexity of the problem at the cost of classical rigor and trajectory detail.[10]

The first step in a MD simulation is to construct the statistical ensemble that best suits the problem to be solved. The number of particles contained in the model must be sufficient to mirror the physical system. To save computation time, one often simplifies the model by using physically justified periodic boundary conditions. Without periodic boundary condition the number of particles in the model must be increased.[122] In the present set of problems periodic boundary conditions were not acceptable since the analysis is to include the simulation of the crystal interior as well as its surfaces.

The second step is to numerically solve the classical equations of motion that govern the time evolution, starting with initial conditions, such as the atom positions and velocities. The initial velocities are naturally chosen to be consistent with the temperature to be analyzed, and are assigned randomly and immediately renormalized, so that the simulated system will have a net zero linear momentum. If the velocities are too high, one can frequently renormalize the velocities to the given input temperature by removing the excessive energy to ensure that the system reaches the chosen equilibrium state.[10]

The computation must be carried out with sufficient time steps to properly image real systems. Most time-consuming is the calculation of the long-range forces. For a system that consists of $N$ particles, each computing time step is proportional to $N^2$ for the nonbonding interactions. For large systems it saves considerable time (and, in turn, permit the simulation of larger systems) if the nonbonding interaction is limited within a suitable chosen cut-off distance. This simplification is usually acceptable since the long-range interactions decay rather rapidly with distance. It was suggested that time steps of the order of $10^{-14}$ s give simulations of stable energies.[122] In practice, however, due to limited computer power, the phase space might not have to be sampled fully in size and time to meet an acceptable accuracy.

Polymer MD simulations, because of the complexity of the interaction terms describing the particles and the large numbers of atoms, have the largest computational requirements. As the computer power and programming efficiency increases, these shortcoming can continually be reduced.[11] The simulations shown in this dissertation are a significant step towards full polymer crystal simulations. Although we do not expect full agreement with experiment, the generic behavior of short-time motion will be displayed for the first time without significant limitations.

### 2.1.1 Classical Mechanics Formulations

The fundamental physical laws that govern the time evolution of a system are contained in the Newtonian mechanics. For the convenience of calculation, the alternative formulations such as Lagrangian and Hamiltonian equations of motion might be used,

depending on the models constructed. In the following sections these will be summarized.

### 2.1.1.1 Newtonian mechanics

For the non-relativistic systems, the motion of a particle $i$ in an inertial reference frame can be correctly described by the Newtonian equation of motion,

$$\mathbf{F}_i = \frac{\mathrm{d}}{\mathrm{d}t}(m_i\mathbf{v}_i) = m_i\frac{\mathrm{d}^2\mathbf{r}_i}{\mathrm{d}t^2} \qquad (1)$$

where $\mathbf{F}_i$ is the net force acting on particle $i$, $m_i$ is its mass, independent of time, $\mathbf{v}_i$ is the velocity, and $\mathbf{r}_i$ the position. If the force is known, the equation of motion can be solved. For a conservative system, the force can be derived from the potential $V_{\mathrm{pot}}$ by $\mathbf{F}_i = -\nabla_i V_{\mathrm{pot}}$.

For the motion of a constrained particle, the forces of constraint may be so complicated that it is difficult or even impossible to obtain explicit expressions for the forces of constraint required in the Newtonian formulation.[124]

### 2.1.1.2 Lagrangian mechanics

Lagrange's equations of motion are the results of Hamilton's principle which is said, together with Einstein's postulates of relativity, to be two of the most elegant and far-reaching principles of the theory of physics.[124] Lagrangian mechanics is not a new theory of mechanics, but an alternative method of dealing with complicated problems in a general manner. For the dynamics of particles, Lagrange's equations are equivalent to Newton's equations. The Lagrange equations of motion in generalized coordinates for

a system with $n$ particles and $m$ equations of constraint can be expressed as:

$$\frac{\partial L}{\partial q_j} - \frac{d}{dt}\frac{\partial L}{\partial \dot{q}_j} = 0, \qquad j = 1,2,...,s \tag{2}$$

where $q$ is the generalized coordinate, $s$, the number of degrees of freedom, specified as $s = 3n - m$ (the system is thus said to have $s$-dimensional space or $s$-configuration space), $\dot{q}$ is the generalized velocity, and the quantity $L$ is called the Lagrange function or the Lagrangian for the system: $L = K(q_j, \dot{q}_j, t) - V(q_j, t)$ where $K$ is the kinetic energy and $V$ is the potential energy.[124]

Another advantage of this description is that the Lagrangian is a scalar function which is invariant with respect to coordinate transformations. No matter what generalized coordinates are chosen for the description of a system, the Lagrangian will have the same value for a given condition of the system.[124]

If the potential energy of a system is velocity-independent, then the generalized momenta $p_j$ can be expressed as:

$$p_j = \frac{\partial L}{\partial \dot{q}_j} \tag{3}$$

and the Lagrange equations of motion have the form:

$$\dot{p}_j = \frac{\partial L}{\partial q_j} \tag{4}$$

The work presented in this dissertation uses the Lagrangian formulations.

### 2.1.1.3 Hamiltonian mechanics

The Hamiltonian of a system is defined as:

$$H = \sum_j p_j \dot{q}_j - L \tag{5}$$

The Hamiltonian is always considered as a function of the $(q_k, p_k, t)$ set, whereas the Lagrangian is a function of $(q_k, \dot{q}_k, t)$ set. The Hamilton equations of motion are

$$\dot{q}_k = \frac{\partial H}{\partial p_k}, \quad \dot{p}_k = -\frac{\partial H}{\partial q_k} \tag{6}$$

If a system is scleronomic (the equation of transformation connecting the rectangular and generalized coordinates is independent of time) which assures that the kinetic energy is a homogeneous quadratic function of the generalized velocities, and if the potential energy of the system is velocity-independent, the Hamiltonian of the system is equal to the total energy $E = H = K + V$.[124]

Hamilton's equations of motion are usually called canonical equations of motion because of their symmetrical appearance, in which the generalized coordinate $q_k$ and the generalized momentum $p_k$ are said to be canonically conjugate quantities. In Lagrangian mechanics there are $s$ second-order differential equations to be solved while in Hamiltonian mechanics there are $2s$ first-order differential equations (canonical equations) to be solved for trajectories.

### 2.1.2 The Potential Energy Functions and Simulation Models

A MD simulation requires prior knowledge of the interaction potentials between atoms. For a system of $N$ particles, the total interaction potential has the form:

$$V = V_{ex} + V_b + V_{nb} \tag{7}$$

where $V_{ex}$ represents the effect of external fields on the system (including, for example, the container walls), $V_b$ represents the bonding potentials, and $V_{nb}$ represents nonbonding interactions. In paraffins or polyethylene the bonding potential includes two-body bonding interaction (such as C–C or C–H stretching motion), three-body bonding interaction (such as C–C–C bending motion), and four-body bonding interaction (such as C–C–C–C torsional motion). The non-bonding interaction $V_{nb}$ can be written as:

$$V_{nb} = \sum_{i>j} V(r_i,r_j) + \sum_{i>j>k} V(r_i,r_j,r_k) + \cdots \tag{8}$$

where the first term is known as pair-wise additive approximation or pair potential, and the remaining terms of the series are often referred to as nonadditive corrections and termed as triplets *etc.* The $i>j$ notation indicates a summation over all distinct pairs $i$ and $j$ without counting any pair twice (*i.e.* as $ij$ and $ji$), and the same care must be taken for triplet *terms etc.*[5,10]

There are two ways to obtain interaction potential functions: *ab initio* calculations and the *empirical* or *semi-empirical* approach.[10,125,126] The *ab initio* methods are quantum mechanics calculations. Empirical or semi-empirical potentials are obtained by fitting parameters in the potential expressions to some known experimental or theoretical results.

As the electron number increases, the *ab initio* calculations become exceedingly difficult. Though there are some cases of using *ab initio* calculations for MD simulations,[126] most MD simulations use empirical or semi-empirical potentials.

To save computation time in polymer MD simulations, some modes are often frozen and the nonbonding interactions are truncated to a certain cut-off distance. Systems containing ionic materials require special treatment because the Coulomb interactions have poor convergence properties.[127,128] Boundary conditions are often used depending on the model used.[5,128]

There are four different models used in the simulations of the present work. In the basic three models (A, C, D), the crystals are suspended in a vacuum and, except for the simulation of the electric field induced defect motion, no external forces are introduced. The simulation models then a constant pressure condition. Model B corresponds to full or partial volume restraint. For each model different potentials are introduced from the literature and will be described next.

#### 2.1.2.1 Model A

In Model A, hydrogens are treated only implicitly, *i.e.* the $CH_2$ is condensed into a united atom. Stretching, bending, and torsional motion of the united $CH_2$-atoms in the molecules are allowed. The simulations presented in Chapters 3, 4, 5 and 7 use this model.

The two-body bonded interaction representing the stretching vibration of adjacent, bonded atoms ($CH_2$-groups) is written as a Morse function:[129]

$$V_{2b}(r_{i,i+1}) = D\{1 - \exp[-\alpha(r_{i,i+1} - r_e)]\}^2 \quad (9)$$

The three-body bonded interaction for the bending of a three-atom sequence is written as:[130]

$$V_{3b}(\theta_{i,i+1,i+2}) = \frac{1}{2}K_\theta(\cos\theta_{i,i+1,i+2} - \cos\theta_0)^2 \quad (10)$$

The four-body bonded interaction representing internal rotation is written as:[131]

$$V_{4b}(\cos\tau_{i,i+1,i+2,i+3}) = 8.37 - a\cos\tau_{i,i+1,i+2,i+3} + b\cos^3\tau_{i,i+1,i+2,i+3} \quad (11)$$

The interaction between any two nonbonded atoms is taken as the Lennard-Jones potential:[132]

$$V_{nb}(r_{ij}) = 4\varepsilon[(\sigma/r_{ij})^{12} - (\sigma/r_{ij})^6]. \quad (12)$$

The parameters for Eqs. (9–12) are listed in Table 1*.

### 2.1.2.2 Model B

Model B is the same as A, except that in Model B some or all of the surface chains are static, *i.e.* all modes of motion in a static chain are frozen. The nonbonding interaction between dynamic and static chains, however, remain active. The case of all surface chains being static, corresponds to a constant volume simulation. For partially fixed surfaces, it corresponds to partial restraint.

*All tables are shown in Appendix C.

### 2.1.2.3 Model C

This model is designed to simulate the motion of defects induced by an electric field,[25] as presented in Chapter 6. The model is identical to Model A, except that one of the $CH_2$-groups in the crystal is replaced by a dipole, such as C=O, for example. The potential energy representing the interaction of the dipole and the external electric field is written as:

$$V_{ex} = \boldsymbol{\mu}_i \cdot \boldsymbol{\varepsilon}, \qquad \boldsymbol{\mu}_i = \frac{\mathbf{r}_{i-1} \times \mathbf{r}_i}{|\mathbf{r}_{i-1} \times \mathbf{r}_i|} \tag{13}$$

where $\boldsymbol{\mu}_i$ is the dipole moment of C=O, $\boldsymbol{\varepsilon}$ is the external electric field, the $\mathbf{r}_{i-1}$ is the vector from atom $i-1$ to $i$, and $\mathbf{r}_i$ is the vector from atom $i$ to $i+1$. The cross-product is the vector-normal associating with a plane formed by atoms $i-1$, $i$, and $i+1$.

### 2.1.2.4 Model D

Model D is modified from the Model A with hydrogen atoms being now explicitly included in the simulation. The C–C two-body bonding interaction is the same as Eq. (9) in Model A. The C–H bonding interaction is written as:[133]

$$V_{C\text{-}H} = D_{C\text{-}H}\{1-\exp[-\alpha_{C\text{-}H}(r_{i,i+1} - r^e_{C\text{-}H}]\}^2 \tag{14}$$

where $D_{C\text{-}H}$ = 446.4 kJ/mol, $\alpha_{C\text{-}H}$ = 17.5 $nm^{-1}$, and $r^e_{C\text{-}H}$ = 0.109 nm.

The C–C–C bonding interaction is:[133]

$$V_{C\text{-}C\text{-}C} = 320.5(\cos\theta_{i,i+1,i+2} - 1.955)^2 \tag{15}$$

The C–C–H bonding interaction is:[133]

$$V_{C\text{-}C\text{-}H} = 175.1(\cos\theta_{C\text{-}C\text{-}H} - 1.900)^2 \quad (16)$$

The H–C–H bonding interaction is:[133]

$$V_{H\text{-}C\text{-}H} = 162.76(\cos\theta_{H\text{-}C\text{-}H} - 1.907)^2 \quad (17)$$

The C–C–C–C torsional potential energy uses Eq. (11) in the Model A. The nonbonding interaction is written as:[133]

$$V_{nb}(r_{ij}) = -ar^{-6} + be^{-cr} \quad (18)$$

where the parameters are: $a = 0.250 \times 10^{-15}$ N nm$^7$, $b = 17.77 \times 10^{-9}$ N nm, and $c = 37.4$ nm$^{-1}$ for H...H nonbonding; $a = 2.014 \times 10^{-15}$ N nm$^7$, $b = 99.49 \times 10^{-9}$ N nm, and $c = 36.7$ nm$^{-1}$ for H...C nonbonding, and $a = 3.716 \times 10^{-15}$ N nm$^7$, $b = 1036.4 \times 10^{-9}$ N nm, and $c = 36.0$ nm$^{-1}$ for C...C nonbonding interactions.

The units used in the expressions presented in this dissertation are SI units. In the computer programming the units are converted into the scales shown in Table 2 of Appendix C.

### 2.1.3 Algorithms

When the model and the potential energy functions are specified, the next step is to solve the ordinary differential equations (ODE) using numerical integration algorithms on computers. This process involves the values of positions and velocities at time $t$ to predict their values at a later time $t + \delta t$ within a desired accuracy. The step size $\delta t$ will affect the stability of trajectory and energy.

There are many algorithms commonly used for MD simulations, such as the Gear predictor-corrector algorithm,[134,135] the Verlet algorithm,[136] and the Runge-Kutta algorithm.[137] Besides, there are many subroutines in computer software libraries such as IMSL and NAG that enable the numerical integration of ODEs. Models using Newtonian and Lagrangian mechanics require a second-order ODE solver and Hamiltonian Mechanics requires fist-order ODE solver. The comparison of different algorithms has been discussed in great detail in the literature.[138]

In the simulations presented in this dissertation, an optimized twelfth order ODE[139] is used to solve the second-order differential equations. The Fortran codes are programmed using optimized techniques.[19,20]

## 2.2 LINKS BETWEEN MICROSCOPIC AND MACROSCOPIC PROPERTIES

The description of materials properties involves macroscopic thermodynamics and macroscopic mechanics. Thermodynamics, containing temperature as a state variable, deals with the processes involving thermal energy transfer though heat, and mechanical energy transfer through work; while the mechanics focuses on the description of the details of processes such as bending, stretching, and fracture.[128]

Computer simulation generates information at the microscopic level and the conversion of this very detailed information into macroscopic terms is the province of statistical mechanics[5] in which averaged macroscopic processes and properties, such as mechanical and thermal equations of state, are related to a microscopic molecular point of view, such as the dynamics of molecules.[128,140] The formulation for the link between

microscopic and macroscopic properties depends on the kind of statistical ensemble that is used in the simulation model.

### 2.2.1 Statistical Ensembles and Thermodynamic Properties

A statistical ensemble is a collection of thermodynamic states in a system of $N$ particles (volume $V$, pressure $P$, temperature $T$, energy $E$, and chemical potential $\mu$). The statistical ensembles commonly recognized are the microcanonical ensemble (constant-*NVE*, with isolated systems useful for theoretical discussions), the canonical ensemble (constant-*NVT*, in which each system is enclosed in a container whose walls produce a heat conducting, closed system), the grand canonical ensemble (constant-$\mu VT$, in which each system is enclosed in a container whose walls are both, heat conducting and permeable to mass transport, producing an open system), and the isothermal-isobaric (constant-*NPT*) ensemble. Different ensembles give different partition functions. However, since ensembles are essentially artificial constructs depending on the problems to be studied and the convenience of the approach, they can be transformed from one to another.[5]

When the partition function is constructed for an ensemble, all thermodynamic functions of state can be derived.[5,128,140] For a system not subjected to external forces, the linear momentum **p** is conserved, and so the MD simulation is said to be dealing with a subset of the microcanonical ensemble, the constant-*NVE***p** ensemble.[5] In fact, energy is not always constant,[5] but rather, it is allowed to fluctuate about the average values because the numerical integration is discretized.

In the case of a microcanonical ensemble, the probability density is proportional to $\delta(H(\Gamma) - E)$ in which $\Gamma$ represents the set of particle positions and momenta, $H(\Gamma)$ is the Hamiltonian, and the delta function selects out of the states of an $N$-particle system in a container of volume $V$ that have the desired energy $E$. When the set of states is discrete, $\delta$ is just the Kronecker delta, taking values of 0 or 1; when the states are continuous, $\delta$ is the Dirac delta function.[5]

The partition function, $Q_{NVE}$ of the microcanonical ensemble is the summation over the probability density:

$$Q_{NVE} = \sum_{\Gamma} \delta(H(\Gamma) - E) \tag{19}$$

In the quasi-classical expression for $Q_{NVE}$ in an atomic system, a factor of $1/N!$ is used to recognize the indistinguishability of atoms:

$$Q_{NVE} = \frac{1}{N! h^{3N}} \int \delta(\mathrm{H}(r,p) - E)\, dr dp \tag{20}$$

in which $h$ is Planck's constant and the integration is carried out over all $6N$ phase-space coordinates. The thermodynamic functions of state can be expressed in terms of the partition function. For example, the entropy of the system, $S$, has the form:

$$S = k_{\mathrm{B}} \ln Q_{NVE} \tag{21}$$

According to the equipartition principle, the temperature of the system can be calculated from the kinetic energy averaged over time steps by the relation:[10]

$$\frac{3}{2}Nk_BT = <\frac{1}{2}\sum_{i}^{N} m_i \dot{r}_i^2> \quad (22)$$

The internal pressure of the system is calculated from the Virial theorem:

$$P = \frac{1}{V}(Nk_BT + W) \quad (23)$$

where $W$ is the virial of the system,[10]

$$W = -\frac{1}{3}\left\langle \sum_{i}^{N} \sum_{j>i}^{N} \mathbf{r}_{ij} \frac{\partial V_{ij}}{\partial \mathbf{r}_{ij}} \right\rangle \quad (24)$$

where $V_{ij}$ is the potential energy function between particles $i$ and $j$.

The constant volume heat capacity can be obtained from time averaged potential or kinetic energy fluctuations:[141]

$$C_v = \frac{nR}{2}\left[1 - \frac{<K^2> - <K>^2}{(n/2)Nk_B^2T^2}\right]^{-1} \quad (25)$$

where $n$ is the degrees of freedom per particle and $K$ the kinetic energy of the system computed at each time step.

Once the heat capacity and temperature are computed, other thermodynamic functions such as enthalpy and free energy can be easily expressed as a function of heat capacity.[69]

### 2.2.2 Radial Distribution Function and Structures

The radial distribution function, g($r$), can be simply thought of as being the number of atoms within a distance $r$ from a given atom, compared to the number within the same

distance in an completely random distribution (such as an ideal gas distribution) at the same density.[5] It can be determined experimentally by X-ray diffraction or neutron scattering.

Theoretically, for a system of $N$ particles in a volume $V$ and at a temperature $T$, the probability that any particle 1 is within $d\mathbf{r}_1$ of $\mathbf{r}_1$, ..., and any particle n is within $d\mathbf{r}_n$ of $\mathbf{r}_n$, irrespective of the configuration of the rest of the particles, is:

$$P^{(n)}(\mathbf{r}_1,\cdots,\mathbf{r}_n) = \frac{N!}{(N-n)!}\frac{\int\cdots\int e^{-U(\mathbf{r}_1,\ldots,\mathbf{r}_N)/k_BT}d\mathbf{r}_{n+1}\cdots d\mathbf{r}_N}{Z_N} \qquad (26)$$

where $U(\mathbf{r}_1,\ldots,\mathbf{r}_N)$ is the potential energy of the system and can be fairly well approximated by a sum of pair-wise potentials which are often assumed to depend only on the distance $r_{ij} = |\mathbf{r}_i - \mathbf{r}_j|$ between the two particles so that

$$U(\mathbf{r}_1,\ldots,\mathbf{r}_N) = \sum_{i<j} u(\mathbf{r}_{ij}), \qquad (27)$$

and $Z_N$ is the configuration integral (there are $N$ choices for the first particle $N-1$ for the second, *etc.*).[5,140]

The simplest distribution function is $P^{(1)}(\mathbf{r}_1)d\mathbf{r}_1$, which is the probability that any one particle will be found in $d\mathbf{r}_1$. For a crystal this is a periodic function of $\mathbf{r}_1$ with sharp maxima at the lattice sites. For a random distribution, such as is found in an ideal gas, all points within volume $V$ are equivalent and so $P^{(1)}(\mathbf{r}_1)$ is independent of $\mathbf{r}_1$. Therefore, the integration for an ideal gas leads to a constant:

$$\frac{1}{V}\int_1^N P^{(1)}(\mathbf{r}_1)d\mathbf{r}_1 = \frac{N}{V} = \rho \tag{28}$$

where $\rho$ is the number density of the random distribution, independent of particle positions.

If the particle distribution is a function of position, it is related to the random distribution by a factor $g^{(n)}$ in the form:

$$P^{(n)}(\mathbf{r}_1,\cdots,\mathbf{r}_n) = \rho^n g^{(n)}(\mathbf{r}_1,\cdots,\mathbf{r}_n) \tag{29}$$

where $\rho^n$ is the random distribution density, and the factor $g^{(n)}(\mathbf{r}_1,...,\mathbf{r}_n)$ is a correlation function since, if the particles were independent of each other, $P^{(n)}$ would equal $\rho^n$, and so the factor equals one. By rearranging the above equations, the correlation function has the form:

$$g^{(n)}(\mathbf{r}_1,\cdots,\mathbf{r}_n) = \frac{V^n N!}{N^n(N-n)!}\frac{\int\cdots\int e^{-U(\mathbf{r}_1,\ldots,\mathbf{r}_N)/kT}d\mathbf{r}_{n+1}\cdots d\mathbf{r}_N}{Z_N} \tag{30}$$

and it is also called a radial distribution function. The two-dimensional radial distribution function $g^{(2)}(\mathbf{r}_1,\mathbf{r}_2)$ depends only upon the relative distance between particle 1 and 2, which is usually expressed as $g^{(2)}(r_{12}) = g(r)$, and it is thus called the pair distribution function. Three-body correlation, $g^{(3)}(\mathbf{r}_1,\mathbf{r}_2,\mathbf{r}_3)$, is called triplet distribution function.[128] The integration of higher-order correlation functions becomes complicated.[140]

In numerical calculations, the pair distribution function can be computed by dividing the interval within $r = 0$ and the cut-off radius into segments of size $\delta r$ and counting the number of atomic pairs, $n(r)$, with a distance falling in a given range $r_i$ to $r_i + \delta r$, then

averaging the results over different time steps to obtain:[10]

$$g(r) = \frac{V}{N}\left\langle \frac{n(r)}{4\pi r^2 \delta r} \right\rangle \tag{31}$$

where $V$ is the simulation volume (for variable volume simulations of crystal systems, the total volume can be taken as the summation of lattice volume).[142,143]

All thermodynamic functions of a system can be written in terms of $g(r)$.[140] The pair distribution function can also be related to the X-ray diffraction pattern[10,58,142–145] and used to compare the theoretical model and the structures determined by X-ray diffraction.

An alternative to compare crystal structure resulting from MD simulation with the one obtained from X-ray measurement is to use the particles coordinates directly, without computing $g(r)$. Fourier transformation of the particle coordinates in a crystal yields the structure factor ($F_{hkl}$) by the following equation:

$$F_{hkl} = \int_{v} \rho(x,y,z) e^{2\pi i(hx+ky+lz)} dv \tag{32}$$

where ρ is the electron density per unit volume.[142]

### 2.2.3 Crystal Vibrational Spectra and Frequency Distribution Function

The vibrational spectra of crystals are an important subject in MD simulations since they contain information on crystal structure and the dynamics of motion. There are many theoretical approaches to the vibrational spectra, such as the normal mode approximation, the Einstein approximation, the Debye approximation, and the full description of the lattice dynamics. Once the frequency distribution is established, many

macroscopic properties can be derived from it.[140]

### 2.2.3.1 Normal mode approximation

Consider a crystal of $N$ atoms with each atom vibrating about its equilibrium lattice point with a small amplitude $\delta r_i$. If the interatomic forces are conservative, the total potential energy is, in the general case, a function of the displacement of the $N$ atoms from their equilibrium positions and can be written in a Taylor series:

$$U(\delta r_1,\delta r_2,\cdots,\delta r_N) = U(0,0,\cdots,0) + \sum_{j=1}^{N}\left(\frac{\partial U}{\partial \delta r_j}\right)_0 \delta r_j + \frac{1}{2}\sum_{i=1}^{N}\sum_{j=1}^{N}\left(\frac{\partial^2 U}{\partial \delta r_i \partial \delta r_j}\right)\delta r_i \delta r_j + \cdots \quad (33)$$

where the zero subscript on the derivatives indicates that they are to be evaluated at the point at which all $\delta r_j$ are zero (equilibrium positions). Using a harmonic approximation, the potential energy is a quadratic function of the displacements which corresponds to the Hooke's law approximation. By introducing the set of force constants $k_{ij}$ and ignoring third- and higher-order terms, the potential energy can be written in Cartesian coordinates as:

$$U(x_1,x_2,\cdots,x_N) = U(0,0,\cdots,0) + \frac{1}{2}\sum_{i}^{3N}\sum_{j}^{3N} k_{ij}(x_i - x_j)^2 + \cdots \quad (34)$$

The first term $U(0, 0, ..., 0)$ is a function of the lattice spacings at the equilibrium positions, and thus a function of density $\rho$, $U(0, 0, ..., 0) = U(0; \rho)$. When terms such as $(x_i - x_j)^2$ are multiplied out, cross terms results in the form $x_1x_2$, $x_1x_3$, and so on. These cross terms represent coupled harmonic oscillators and make the potential energy and the

Hamiltonian a complicated mixture of $x_i$ and $x_j$. However, these vibrational motions can be rigorously decomposed into a set of independent harmonic oscillators by introducing normal coordinates $Q_i$ which are defined as the linear combinations of the coordinates $\delta r_i$ and bring the potential and kinetic energies simultaneously into the diagonal forms:

$$V = \frac{1}{2}\sum_{i-1}^{3N} \omega_i^2 Q_i^2, \quad K = \frac{1}{2}\sum_{i-1}^{3N} \dot{Q}_i^2, \quad \dot{Q}_i = \frac{\partial K}{\partial \dot{Q}_i} = P \tag{35}$$

and the solutions of Hamilton's equations in normal coordinates are

$$Q_i = Q_i^{\circ}\sin(\omega_i t + \delta_i) \tag{36}$$

and the determination of normal coordinates is called a normal coordinate analysis.

A general solution may be given from the linear combination of normal coordinates. When $Q_1$, ..., $Q_{r-1}$, $Q_{r+1}$, ..., $Q_{3N}$ are all zero and $Q_r \neq 0$ then the system is vibrating in a normal mode and the motion of each particle is periodic with the same frequency $\omega_r$ and with the same phase.

If there are $N$ atoms in the crystal, there are $3N$ degrees of freedom, of which there are $3N - 6$ vibrational degree of freedom (since three of them are counted for the translational motion of the whole crystal, and another three are accounted for the rotation of the crystal). But for large $N$, the approximation $3N - 6 \approx 3N$ does not introduce a noticeable error and the result of normal coordinate analysis would yield about $3N$ vibrational frequencies:

$$\nu_j = \frac{1}{2\pi}\sqrt{\frac{k_j}{\mu_j}}; \qquad j = 1,2,\cdots,3N-6 \approx 3N \tag{37}$$

where $k_j$ and $\mu_j$ are an effective force constant and an effective reduced mass, respectively.[140]

Under the normal mode approximation, the frequencies are evenly distributed so the frequency distribution function $g(\nu)$ has the property of

$$\int_0^\infty g(\nu)d\nu = 3N \tag{38}$$

and if the function $g(\nu)$ can be determined, the thermodynamic properties of the crystal can be calculated by:[140]

$$E = U(0;\rho) + \int_0^\infty \left[\frac{h\nu e^{-h\nu/kT}}{(1 - e^{h\nu/kT})} + \frac{h\nu}{2}\right] g(\nu)d\nu \tag{39}$$

and

$$C_V = k\int_0^\infty \frac{(h\nu/kT)^2 e^{-h\nu/kT} g(\nu)d\nu}{(1 - e^{-h\nu/kT})^2} \tag{40}$$

Exact calculation of $\mathbf{g}(\nu)$ requires the lattice dynamics theory.[140] Useful and well known approximation to $g(\nu)$ are given by the Einstein and Debye approximations.[69]

### 2.2.3.2 Einstein approximation

The classical theory of heat capacity predicts on the basis of equipartition of energy that the molar heat capacity at constant volume is $3Nk = 3R = 25.104$ J/(K mol). This prediction is in good agreement particularly with the observed heat capacity of many metals at sufficiently high temperatures, often even down to room temperature. The agreement fails, however, completely for many covalent compounds and even for metals

at low temperatures.[140] The constant volume heat capacity at low temperature was first explained and approximated by the Einstein's theory.[146]

Einstein assumed that each atom in the crystal is an independent oscillator in the *x*-, *y*-, and *z*-directions with the same frequency $\nu$. The energy of each of these $3N$ independent oscillators is quantized so that the frequency spectrum $g(\nu)$ is a delta function at one frequency:

$$g(\nu) = 3N\delta(\nu - \nu_E) \tag{41}$$

where $\nu_E$ is the single frequency (Einstein frequency) assigned to all $3N$ independent oscillators of the crystal. The Einstein frequency is then a characteristic constant for a given crystal. The constant volume heat capacity can be expressed as:

$$C_v = 3Nk\left(\frac{\Theta_E}{T}\right)^2 \frac{e^{-\Theta_E/T}}{(1 - e^{-\Theta_E/T})^2}, \qquad \Theta_E = \frac{h\nu_E}{k} \tag{42}$$

where $\Theta_E$, the Einstein temperature, is the adjustable parameter to fit the experimental heat capacity curve. An expansion of the Einstein approximation is possible by choosing more than one "Einstein frequency". Ultimately one can compute the heat capacity by adding the contributions of all the various frequencies as shown by Eq. (40).[69,140]

### 2.2.3.3 Debye approximation

In the normal mode approximation, the normal frequencies are not due to the vibrations of single atoms, but are a concerted harmonic motion of all atoms. In the Debye theory[147] the normal frequencies are treated by reasoning that those normal modes

whose wavelengths are long compared to the atomic spacing do not depend upon the detailed atomic character of the solid and could, thus, be calculated by assuming that the crystal is a continuous, elastic body, with the elastic constants of a body being quantities such as the compressibility and Young's modulus.

The frequency distribution derived by Debye has the form:

$$g(\nu) = \frac{12\pi V}{v_0^3}\nu^2, \qquad \frac{3}{v_0^3} \equiv \frac{2}{v_t^3} + \frac{1}{v_l^3} \tag{43}$$

where $v_t$ is the transverse velocity (there are two transverse waves in which the medium vibrates perpendicular to the direction of wave vector **k**), $v_l$ is the longitudinal velocity (there is one longitudinal wave in which the medium vibrates in the same direction as the wave is propagated), and $\nu_0$ is the average velocity.[140] Debye defined a maximum frequency $\nu_D$ such that the integral of $g(\nu)d\nu$ from 0 to $\nu_D$ equals $3N$, since the total number of normal frequencies is $3N$ so that the integration

$$\int_0^{\nu_D} g(\nu)d\nu = 3N \tag{44}$$

gives the maximum frequency

$$\nu_D = \left(\frac{3N}{4\pi V}\right)^{1/3} v_0 \tag{45}$$

The frequency $\nu_D$ is called the Debye frequency. In terms of $\nu_D$, the distribution function $g(\nu)$ is

$$g(\nu)d\nu = \frac{9N}{\nu_D^3}\nu^2 \qquad 0 \le \nu \le \nu_D$$
$$= 0 \qquad \nu > \nu_D \tag{46}$$

According to the Debye theory, the constant volume heat capacity can be expressed as:

$$C_V = 9Nk\left(\frac{T}{\Theta_D}\right)^3 \int_0^{\Theta_D/T} \frac{x^4 e^x}{(e^x - 1)^2} dx, \qquad \Theta_D = \frac{h\nu_D}{k}, \qquad x = \frac{h\nu}{kT} \tag{47}$$

where $\Theta_D$ is the Debye temperature. The integral in Eq.(47) cannot be evaluated in closed form and must be evaluated numerically. By defining a function $D(T/\Theta_D)$, well-tabulated as function of $T/\Theta_D$:[69]

$$D\left(\frac{T}{\Theta_D}\right) = 3\left(\frac{T}{\Theta_D}\right)^3 \int_0^{\Theta_D/T} \frac{x^4 e^x}{(e^x - 1)^2} dx \tag{48}$$

the heat capacity becomes $C_V = 3NkD(T/\Theta_D)$. The values of $\Theta_D$ are those which give the best overall fit to the experimental data.[140]

If the vibration out of the plane are prohibited, there is a maximum of $2N$ vibrations for the two-dimensional vibrator and the frequency distribution and constant heat capacity becomes

$$g(\nu)d\nu = \frac{4N\nu}{\nu_2^2}, \qquad C_V = 2NkD_2\left(\frac{\Theta_2}{T}\right) \tag{49}$$

where $\nu_2$ is the maximum two-dimensional frequency, $D_2$ is the two-dimensional Debye function, and $\Theta_2$ is the two-dimensional Debye temperature. For one-dimensional

vibration, the frequency distribution is a constant depending only on the maximum frequency $\nu_1$, so that,

$$g(\nu)d\nu = \frac{N}{\nu_1}, \qquad C_V = NkD_1\left(\frac{\Theta_1}{T}\right) \tag{50}$$

where $D_1$ and $\Theta_1$ are one-dimensional Debye function and the Debye temperature, respectively.[69]

### 2.2.3.4 Lattice dynamics and dispersion curves

Lattice dynamics is the object of the study of the motion of particles about their equilibrium positions using classical mechanics.[140] Depending on the lattice model, once the Hamiltonian is constructed (via the kinetic and potential energies), the equation of motion can be derived and their solutions are in wave forms as functions of frequency $\omega$ ($\omega = 2\pi\nu$), wave vector $k$ ($k = 2\pi/\lambda$), and time $t$. The value of $\omega/k$ is the velocity of the wave, $\lambda\nu$, the so-called phase velocity. Since different wavelengths travel with different velocities, a dispersion of the waves occurs as they pass through a prism. The relation between the frequency and the wave vector is thus called a dispersion curve. Experimentally, the dispersion curve can be determined by inelastic neutron scattering. The importance of dispersion curves lies in their easy link to the frequency distribution and the thermodynamic properties.

Since each normal mode vibration of the $3N$ oscillators is independent, the vibrations of the lattice are quantized and called phonons. The phonons are essentially quanta of the lattice vibrations, just as photons are quanta of electromagnetic vibrations. The

magnitude of the wave velocities are found to be on the order of magnitude of the sound velocity (the initial slope of the dispersion curve), so phonons can be thought of as quanta of sound waves passing through the crystals.[140]

Although a one-dimensional lattice dynamics calculation is easy, the actual two- and three-dimensional lattice dynamics calculations become more difficult.[140] Moreover, the vibrational motion is, particularly at higher temperature and in polymer crystals, sufficiently anharmonic to destroy the ease of separation of the normal modes.[14]

## 2.3 VISUALIZATION AND ANIMATION

Using the statistical mechanics principles introduced above, one can link the microscopic properties to macroscopic properties mathematically. However, to understand the atomistic details of the "invisible" microscopic world, one may need to "slow down" the atomistic process to be able to see it. Visualization and animation are important steps in MD simulations to bring this microscopic world vividly to the macroscopic level.

It is true that "one picture is worth a thousand words." But in MD simulation, a massive amount of time sequent coordinates with hundreds of thousands of pictures is likely needed to be produced. It is often difficult to piece them together and analyze them in time sequence. Computer animation has overcome this difficulty. In the simulations described in this dissertation, the massive data of trajectories has been converted in to graphics using Matlab, or molecular models using MacMolecules, and animated by Macromind Director on the Macintosh computer in our laboratory. The movies have also been converted to video tape for common uses and presentation in the

ViSCLab at Oak Ridge National Laboratory. It is now also true that a disk or tape is worth a thousand pictures or a million words.

With the aid of visualization and animation, the twist motion of molecular chains, the formation and the change of domains in the crystals, and the surface melting have been analyzed in three dimensions and become visible for better understanding of the mechanism of molecular motions and phase transitions. A VHS tape will be shown during the dissertation defense and is available at later time on request.

# CHAPTER 3

# THE HEXAGONAL STRUCTURE OF UNCONSTRAINED POLYMETHYLENE CRYSTALS

In this chapter the atomistic details of the dynamics and structure-changes in unconstrained paraffin and PE crystals below the melting temperature will be presented. In this simulation the nonconstrained, zero pressure Model A, described in Sect. 2.1.2.1 is discussed. In order to investigate the structural dependence of the dynamic processes and the transitions to the stable structure, three types of initial arrangements of the $CH_2$-chains were used in these simulations: **1.** an orthorhombic arrangement with placement of chains in the positions of the experimentally known stable polyethylene crystal structure at room temperature [(ORTH): $a = 0.74$, $b = 0.49$, $c = 0.25$ nm (with $c$ being the chain axis)];[59] **2.** a monoclinic arrangement, as is frequently found on deformation of the stable orthorhombic crystals of polyethylene during drawing and compression [(MONO): $a = 0.81$, $b = 0.25$, $c = 0.48$ nm, and $\beta = 108°$ (with $b$ being the chain axis)];[63] **3.** an arrangement with random rotation of the zig-zag planes of the molecules in the orthorhombic positions, to perhaps simulate a hexagonal structure (HEXA). The initial crystal structures ORTH and MONO are illustrated in Fig. 1b in a projection along the chain-axes. The double crosses mark the zig-zag positions of the carbon atoms in the all-*trans* chain. In Fig. 1b each crystal contains 192 chains of all-*trans* zig-zag chains and each chain consists of 50 $CH_2$-groups, *i.e.* there are 9600 $CH_2$-groups in each crystal with an initial dimension of about $6.0 \times 6.0 \times 6.3 = 227$ nm$^3$. Each of the 9600 $CH_2$-groups

was treated as a united atom with a mass of $m$ = 14.03 amu to reduce the computation time.

The Lagrangian operator $L$ for the system is described as:

$$
\begin{aligned}
L = & \sum_{i=1}^{N} \frac{1}{2}(m\dot{x}_i^2 + m\dot{y}_i^2 + m\dot{z}_i^2) \\
& - \sum_{i=1}^{N-1} V_{2b}(r_{i,i+1}) - \sum_{i=1}^{N-2} V_{3b}(\theta_{i,i+1,i+2}) \\
& - \sum_{i=1}^{N-3} V_{4b}(\cos\tau_{i,i+1,i+2,i+3}) - \sum_{|i-j|\geq 4}^{N} V_{NB}(r_{ij})
\end{aligned}
\tag{51}
$$

where the first term is the kinetic energy, and the other terms are the potential energy functions derived for the description of the $CH_2$-groups, and described in Eqs. (9–12). The Lagrangian equations of motion [Eq. (2)] were then solved on a CRAY/X-MP at Oak Ridge National Laboratory using an optimized twelfth order RKH for second order differential equations.[19,20] The subsequent calculation of the crystal lattice parameters and *gauche* concentrations were performed on the IBM/ 3090, and further data analyses and plots were carried out using Matlab on a VAX/ 8800 at The University of Tennessee in Knoxville.

To start the simulations, a given amount of momentum was distributed randomly throughout the initial crystal and the system was subjected to a zero center-of-mass velocity constraint. The system was allowed to expand or contract under zero pressure. The structure and physical properties of the simulated systems were evaluated periodically during the simulations. Twelve simulations were run for 10 or 25 ps, each, with the nonbonded interactions being cutoff at 1.0 nm. The error of the integrations was controlled to be less than $10^{-4}$. There are a total of 28,800 second order differential

equations to be solved for each time step. A typical 10 ps simulation requires about 15 hours of CPU time on the CRAY/X-MP at Oak Ridge National Laboratory.

## 3.1 RESULTS

The simulations are identified by their run number, initial structure, temperature, and run time in Table 3. The global results, as expressed by average crystal density and the concentration of *gauche* bonds, are also given in Table 3. The effective temperatures of the simulations were calculated every 0.1 ps using the relationship:

$$\frac{3}{2}NkT = \frac{1}{2}m\sum_{i-1}^{N}(\dot{x}_i^2 + \dot{y}_i^2 + \dot{z}_i^2) \qquad (52)$$

where $k$ is Boltzmann's constant and $\dot{x}_i$, $\dot{y}_i$, and $\dot{z}_i$ are the Cartesian velocities of the atoms $i$, and $N$ is the total number of atoms in the crystal. The results are shown in Fig. 2.

Each dihedral angle $\tau$ was calculated and found to deviate in various degrees from the initial 180° of the all-*trans* chain. Once the angle $\tau$ deviated by more than 90° from the *trans*-angle, the conformation was counted as *gauche*. In Table 3 the average *gauche* concentrations (percentage of *gauche* bonds in the entire crystal) are given over a time-period of 5 ps after steady-state had been reached, and the results are compared with IR measurements shown in Fig. 3. In these (relatively low temperature) simulations it has been observed that the *gauche* bonds usually do not form blocks, rather, they can be found in isolated positions close to the chain-ends or in surface chains. The life-time of a *gauche* "conformer" is only a few picoseconds. A detailed study of the rate of

formation and life-time of *gauche* conformers for polyethylene-like crystals was made earlier.[29]

The density calculations were performed by counting the number of atoms inside a chosen cubic box multiplied by the mass of the $CH_2$-groups and divided by the volume of the box. Since the system undergoes volume fluctuations, the placement of the cubic box affects the calculated densities to some degree. To minimize surface effects, the cubic box was placed in the center of the crystal. The density at any time was then taken as the average of ten evaluations with ten concentric cubic boxes with side lengths increasing from 3.2 nm to 5 nm. Typical deviations for these series of calculations were $\pm 0.04$ Mg/m$^3$. The results are plotted as a function of time as shown in Fig. 4.

The radial distribution functions of the $CH_2$-groups were calculated every 0.1 ps for each simulation. All plots of $g(r)$ stabilized after a few picoseconds, and the $g(r)$ of ORTH, MONO, and HEXA became almost indistinguishable. Figure 5 shows a typical example (MONO at 159 K) of the radial distribution function as a function of time. The temperature and initial structure dependence of $g(r)$ are compared in Fig. 6.

The spatial coordinates of each $CH_2$-unit were plotted in picosecond intervals in $x$-$y$, $x$-$z$, and $y$-$z$ projection, respectively, where $z$ is parallel to the chain direction. During the first picosecond, all crystals show expansion along the $x$-axis and shrinkage along the $y$-axis. This tendency persists for a few picoseconds, depending on the temperature and initial structure, then the motion reverses leading to a volume breathing-vibration mode. Figure 7 summarizes the $x$-$y$ projection of the MONO crystal at 10 ps at four different temperatures, revealing an obvious domain structure relative to the setting angle of the

zig-zag plane. Figures 8 and 9 are examples of snapshots at 10 ps in $x$-$z$ and $y$-$z$ projection of a MONO crystal at 234 K (run 8, Table 3). Of particular interest in these latter figures is the change in crystal perfection and unit cell dimensions on going to the surfaces of the crystal.

The dynamic details of the single chain, were studied by spatial plots of the center and the surface chain at different temperatures in the time interval of 0.05 ps. Figure 10 shows the results of the $y$-$z$ projection of the center chain in the MONO crystal at 316 K (run 9, Table 3). As can be seen from Fig. 10, each chain undergoes rapid twist motion resulting in changes of the orientation of the zig-zag plane of the molecule. After about 1.5 ps the chain is rotating via segmental motion, starting at the top of the crystal. Within about 0.5 ps the chain has turned by about 90°. Similarly, a new side-on view of the zig-zag develops between 7 and 8 ps, indicating another overall 90° rotation, turning roughly back to the initial orientation. As temperature increases, the frequency and amplitude of this motion increases.

The surface chains have larger amplitudes of motion than the center chains. In order to understand the mechanism of the formation of disorder, the atom positions for each crystal were plotted separately layer by layer in $x$-$y$, $x$-$z$, and $y$-$z$ projection at every picosecond. Figure 11 shows an example of such a plot. The detailed correlation of the motion between neighboring chains is not apparent from these large-interval snapshots; however, it is clear that the rapid twist motion causes the individual chain to move in the $z$ direction, and that the bending is coupled to the motion of the neighboring chains. This coupling increases with temperature and has become significant at the 403 K simulation

depicted in Fig. 11. Actual melting will be described on longer-time simulations in Chapter 4. The movement of each $CH_2$-group from the initial position (shown in Fig. 1b) to the average reached between 5 and 10 ps at 234 K is shown in Fig. 12. The counting of the $CH_2$-groups starts at the bottom of the lower left corner of the MONO in Fig. 1b (#1), continues to the top of the crystal (#50), jumps to the bottom of the right neighboring chain in the $x$-$z$-plane (#51), and continues to the end of the first $x$-$z$-plane (#800), to start with the bottom left of the second $x$-$z$-plane (#801) and finishes with the upper right corner of the 12$^{th}$ $x$-$z$-plane (#9600).

Each streak of the Δx-plot in Fig. 12 represents thus the 800 $CH_2$-groups of one $x$-$y$ plane of 16 $C_{50}$-chains. The center chains have not moved, but the crystal expands uniformly along the $x$-axis (compare with Fig. 8). The Δy-plot, similarly shows the movement of the lower and upper 6 planes away from the center (compare with Fig. 9). The Δz-plot, finally shows the more random upward and downward movement of the $C_{50}$-chains.

For a quantitative description of the amount of disorder developed in the crystals as a function of temperature, the standard deviations of the coordinates were calculated using Eqs. (53–57),

$$\Delta x = \sqrt{\frac{\sum_{i}^{n} (x_i^a - x_i^o)^2}{n}} \qquad (53)$$

$$\Delta y = \sqrt{\frac{\sum_{i}^{n} (y_i^a - y_i^\circ)^2}{n}} \tag{54}$$

$$\Delta z = \sqrt{\frac{\sum_{i}^{n} (z_i^a - z_i^\circ)^2}{n}} \tag{55}$$

$$\Delta xyz = \Delta x + \Delta y + \Delta z \tag{56}$$

$$\Delta r = \sqrt{\Delta x^2 + \Delta y^2 + \Delta z^2} \tag{57}$$

where $x_i^a$, $y_i^a$, and $z_i^a$ represent the Cartesian coordinates of each individual $CH_2$-group in the crystal averaged between 5 and 10 ps, $x_i^\circ$, $y_i^\circ$, and $z_i^\circ$ represent the Cartesian coordinates of each individual $CH_2$-group in the initial crystal, and $n$ is the total number of $CH_2$-groups in a crystal. The results are shown in Table 4.

More details about the steady-state crystal structure can be gained from the lattice parameters, evaluated from the time-averaged spatial coordinates of the simulated crystals. The results are shown in Figs. 13 and 14. Since the setting angle is variable, due to the twist motion observed from Fig. 10, a primitive unit cell was taken as the parallelepiped composed of the eight appropriate mid-points of the C–C-bonds calculated from the coordinates of every two adjacent bonded atoms throughout the entire crystal. This choice avoids the introduction of extra positional variation due to torsional vibrations. The details of the method for the calculation of lattice parameters is shown in the Fortran code in Appendix D. This Fortran code depends on the structure of the I/O data-set

format that contains the carbon coordinates which are derived with another Fortran code, listed in Appendix E. In this evaluation, the *c*-dimension in the lattice is taken in the chain direction (*z*-direction). The sliding of chains in the *z*-direction, seen in Fig. 12, that would cause major changes in the lattice dimensions was corrected for. The lattice parameters *a*, *b*, *c*, $\alpha$, $\beta$, and $\gamma$, calculated in this way for the initial ORTH structure of Fig. 1b are 0.49, 0.44, and 0.25 nm, and 90, 90, and 124°, respectively. For the initial MONO structure of Fig. 1b the parameters are 0.41, 0.48, and 0.25 nm, and 90, 90, and 108°, respectively. The maxima in the distribution curves of Fig. 13 suggest a hexagonal lattice with $a \approx b \approx 0.465$ nm and $\gamma \approx 120°$. Figure 14 shows the spatial distribution of the functions of the unit cell parameters. The distribution is relatively uniform with major deviations concentrating at the surfaces.

The same evaluation as in Fig. 13 was carried out for the instantaneous structures in time steps of one picosecond, as well as for the crystal structures averaged over time at the different temperatures after having reached steady-state (5–10 ps). This evaluation of the simulated crystals starting from ORTH, MONO, and HEXA, reveals that the lattice parameters averaged over time, as well as at fixed moments in time, have changed from their initial, single values to closely similar broad distributions. Broadening occurs even at temperatures as low as 53 K and increases with temperature. Tables 5 and 6 shows the change in lattice parameters and their standard deviations as functions of temperature and time.

## 3.2 DISCUSSIONS

The crystals discussed in this chapter were designed to probe the dynamics of molecular chains in which all modes of motion are active without constraints. The dynamics and structures of crystals subject to constraints, such as by a container or perhaps even an amorphous environment will be discussed in Chapter 4. Much more limited work on the explicit influence of the structure of the hydrogen atoms (full atom simulation) will be discussed in Chapter 6. The simulations presented in this paper contain the results for a flexible, linear chain crystal without side-chains. Besides giving results on the dynamics, the simulations are also useful in the understanding of the surface effects.

Although the simulation times are short, in the picosecond time scale, they give information about the elementary steps of large-amplitude motion common to all polymer crystals. A first attempt to link these with, the by a factor $10^{-9}$ slower, macroscopic dynamics will be made in the present discussion. A more specific example, that of the behavior of a dipole attached to a chain in a crystal, will be treated in Chapter 5.

The simulations have, in themselves, a "generic" importance. They represent the first large scale MD calculation on a crystal of a size that approaches that of the smallest-size crystals typically found in melt-crystallized polymers.[57] The question of how close the simulation can come to "real" paraffin or polyethylene crystals can be judged from the input parameters of Table 1. One expects a close modeling of all chain effects that are largely governed by Eqs. (9–12), such as conformational isomer dynamics, intramolecular vibration spectra, and torsional defects. Indeed, the concentration of *gauche* defects

(Table 3) and their location at the crystal surface are closely matched by the IR measurements on paraffins.[33] The deviation of the heat capacity prior to melting matches also the energetics of the *gauche* defects.[12,34] The skeletal vibrational spectrum and its change on increasing the temperature due to anharmonicity[13,14] and its variation with strain[119] could be modeled. Even melting is properly reproduced.[29] In this Chapter it is shown, in addition, that density and sonic velocity are close to the experimental data.

Less correspondence to experiment is expected for effects based on the van-der-Waals terms of Eq. (12). Two simplifications that involve the use of Eq. (12) are expected to remove the simulations from exact correspondence to experiment. First, the united atom approximation changes the close-range geometry of the $CH_2$-group. Instead of a three-center attraction, it yields a single-center attraction. Second, the limitation of Eq. (12) to distances $r_{i,j} \leq 1.0$ nm can lead to the elimination of more subtle packing effects, and also causes difficulties in the simulation when parts of the surface chains drift into vacuum. The major observation in the present simulations is that for all chosen temperatures a close-to-hexagonal structure arises. The experimental existence-range of the hexagonal phases, however, is limited, in contrast to the simulations. For some paraffins there is a small temperature range of stability of the hexagonal phase before melting, and for polyethylene, there exists a high temperature hexagonal phase that reaches below melting only at elevated pressure.[27] The reason for this discrepancy is likely to be the difference in close-range packing that was shown by Kitaigorodskii[148] to be essential for the stability of a given crystal structure. As shown in Chapter 2.3.6 of ref. 57, the proper crystal structure of $CH_2$-groups relies on a close match of the hydrogen atom shape of one

molecule into the hollow created by the appropriate three hydrogen atoms of the neighboring chains, something not contained in the present simulation. At higher temperatures, the dependence on special shape decreases as the vibrational motion averages the atomic contours, so that one expects that the hexagonal phase observed here can be used as a reasonable model for the experimentally observed high-temperature hexagonal phase.

### 3.2.1 Steady States

The initial crystal structures, ORTH and MONO, represent perfect crystals constructed with unit cell parameters derived from X-ray diffraction data for polyethylene. The X-ray data are, in turn, time-averages at room temperature. In case the crystal contains domains of different structures of dimensions less than the X-ray beam diameter, the results are also domain averages. A typical X-ray beam diameter is in the μm range, *i.e.* about $10^6$ times larger than the cross-section of the crystals simulated here. The initial HEXA structure is a model that was originally designed to probe the dynamics of the so-called "rotator phase" of a hexagonal paraffin, but was found to yield little additional information since all initial states approached the same steady state.

In the simulations, the initial total energy is purely kinetic, but it rapidly reaches a Boltzmann distribution as is indicated by the quick approach to steady-state, shown in the temperature plots in Fig. 2. One can see that for the simulations below the experimental melting point of pentacontane (365.3 K) all crystals reach thermal steady-state in one to two picoseconds. The simulations that start with different initial structures,

but with the same initial momentum give closely similar temperature curves (runs 1, 6, and 11; runs 2 and 7; runs 3 and 8; runs 4, 9, and 12; and runs 5 and 10 in Table 3 are groups with the same starting momentum). The constancy of temperature documents also the precision of the simulation. Runs 5 and 10 show some decrease in temperature, a sign of the beginning of fusion which is a topic that will be discussed in more detail in Chapter 4 with additional long-time simulations.

The density plots in Fig. 4 show oscillations about the average values listed in Table 3 which are close to the experimental density of polyethylene (0.977 at 300 K). At about the same temperature, different initial structures have slightly different density fluctuations in direction and amplitude, but with about the same frequency ($\approx 3\times10^{11}$ Hz). Assuming one sees the first fundamental vibration of the crystal with a wavelength of about 12 nm, one can estimate the speed of the wave to be about 4 km/s which is close to typical speeds of sound measured in polymers (1.4–5.9 km/s).[149]

On a smaller scale, the $g(r)$ plots shown in Fig. 5 indicate that a steady-state structure is reached quickly. As soon as temperature reaches its steady-state (Fig. 2), a steady-state structure is established. Most interesting is that different starting structures reach indistinguishable statistical distributions, as illustrated in Fig. 6. As the temperature increases (see Fig. 6), $g(r)$ at steady-state shows little temperature dependence. All simulations lead to the same average structure.

By combining the results of temperature, radial distribution, and density plots, one reaches the conclusion that similar steady-states are reached for all simulations. To understand the structure and dynamics, it is necessary to know the atomistic details of the

crystals at steady-state, to be discussed in the next sections using spatial plots and lattice parameter analyses.

### 3.2.2 Disorder, Gauche Defects, and Chain Dynamics

The steady-state structures of the crystals can be made out from Figs. 7–9. At 57 K (Fig. 7a) the crystal structure deviates already from its initial perfect structure (Fig. 1b). Not only are the projections of the $(CH_2-)_{50}$ chains broadened due to the vibrations, one can also see a break-up into at least two domains, separated by boundary layers of two to three chain layers. The domains are characterized by different orientations of the zig-zag plane (setting angles). At 234 K the crystal becomes more disordered (see also Figs. 8 and 9) and develops more easily recognizable domains (Fig. 7c). The disorder increases with temperature and becomes significant at 316 K (Fig. 7d), about 50 K below experimental melting point. The scale of disordering is not uniform throughout the entire crystal, but seems to vary from one domain to another.

To obtain more detail about the development of the domain structure, average setting angles were computed for each chain in the crystal at each picosecond and plotted. For simulations starting in a compressive as well as an expansive mode (see Fig. 4), the chains have gone through the first major rotation within about 2 ps (see also Fig. 10). By about 5 ps all zig-zag chains achieve an approximate alignment in the $x$-$z$-plane. This predominantly parallel alignment of the zig-zag planes coincides with a minimum in the crystallographic $b$-dimension at 5–6 ps (see Table 6). By about 10 ps the domain structure is fully developed, as shown in Fig. 7. Two types of dynamically interchanging

domains can be recognized, those of largely parallel zig-zag chains and those with major disorder in the setting angles. The coincidence of parallel zig-zag chains with compression at right angles to the zig-zag plane suggests a close coupling of the transverse lattice vibrations with the setting angle.

Inspection of Figs. 7c, 8 and 9 (234 K) reveals that the surface layer of the crystal to a depth of 1–2 nm is more disordered than the core. Similarly, an inspection of the dynamics of chain rotation reveals faster and more frequent changes in the setting angle of the zig-zag planes of the surface chains. The lattice dimensions expand approaching the surface and, occasionally, chain segments actually leave the crystal surface, particularly at temperatures close to melting. The shown projections are part of a set of 6000 printouts that document the generality of this behavior.

From the present simulations it is found that the *gauche* defects become noticeable at about 230 K, as is shown in Table 3. There is an exponential increase of *gauche* concentration with temperature which is consistent with the IR experimental results as shown in Fig. 3. By converting the concentration from *gauche* bonds per chain to *gauche* bond percentage of all dihedral angles (there are 47 dihedral angles in a chain), the experimental *gauche* concentration for $C_{50}$ is 0.21% at 323 K and 1.7% at 365 K.[33] Obviously, the small number of *gauche* bonds is insufficient as a cause of the domains of the disordered phase, but it is sufficient to explain the initial heat capacity increase detected by DSC. For $C_{50}H_{102}$ the heat capacity starts to show a first increase beyond the vibrational heat capacity at 260 K. Close to melting, the heat capacity increase has reached about 20%.[34]

Although the majority of bonds are at any one time close to *trans* "conformers", each of them is found to frequently deviate somewhat from a perfect *trans* 180° conformation. Overall, the zig-zag chain often obtains a twist if sequential small deviations are in the same rotation direction. In the time sequence of chain conformations shown in Fig. 10 one can see that larger-amplitude transverse vibrations start early. Somewhat later (about 1.2 ps) a twist is created, starting at the top of the crystal. At about 2 ps it has generated, for the first time, 90° rotation of the upper chain end, visible in the projection by a change of the zig-zag into a line. Between 2.5 and 7 ps the whole chain is turned by almost 90°. Small blocks of (in the projection) unturned chain segments appear, however, from time to time and travel through the chain, as well as change in size. After about 7 ps the chain is rotated again, resuming largely the initial conformation. This sequence of chain conformations illustrates the detailed mechanism of the segmental motion needed to make a "rotator" phase. Cooperative motion in neighboring chains lead to the domain structure, all being driven, as outlined above, by the transverse, intermolecular vibration modes. The larger mobility of the chain ends is also documented by this time-sequence of conformations of the center chain. The even larger motion of the surface chains can be seen from Figs. 11 and 12.

### 3.2.3 Distribution of Lattice Parameters and Multi-domain Structures

The details of multi-domain structures in hexagonal crystals are provided by analysis of the distribution of the lattice parameters in the time-averaged steady-state structures, as is shown in Figs. 13 and 14 and the data in Tables 5 and 6. Spatial plots such as Fig.

7 and their averages prove that the constant twist motion of the molecular chains of constant setting angles exist only over a short range, and deviations from the initial crystallographic lattice point are significant even in the steady-state structures. Therefore, the ideal crystallographic sense of a repeating symmetry no longer exists in the crystals simulated here. The overall space- and time-average positions and arrangements of atoms in three dimensions, illustrated by Tables 4 and 5, yield an overall hexagonal structure. The crystal motif, the ($CH_2$–)-group, can be placed in a high-symmetry lattice only because of the long-time average and positional average seen by X-ray diffraction.

The crystal analyzed in Fig. 13 started as MONO at 234 K, *i.e.* the angle $\gamma$ shifted from 108° to a mean of 120.5°. The $\alpha$ and $\beta$ angles remain always close to 90°, as expected for all three crystal structures. The mean *a* and *b* dimensions (0.468 and 0.461 nm) are very similar and far from the values for MONO or ORTH crystals (0.49 and 0.44; 0.41 and 0.48 nm). The broad distributions permit, however, local and instantaneous MONO as well as ORTH structures, and even fully disordered neighbors (see Figs. 7–9).

The "rotator phase" of paraffins is on the basis of the present simulations to be described as a nanometer-scale domain-structure that changes setting angles on a picosecond time scale to average to hexagonal crystal symmetry. The main motion involved in the dynamics of domains is a segmental twist that can ultimately rotate the full chain in a picosecond. The conformational disorder, originally thought to be of major importance,[27] is only of minor significance in the explanation of the hexagonal structure of the paraffins. The concentration of the conformational defects increases, however,

exponentially with temperature and may reach the melt level for the high-temperature hexagonal phase of polyethylene which is stable at elevated pressure.[27] Some experimental evidence for such high defect concentrations has also been discussed in ref. 27. These observations explain also why the difference in *gauche* conformations is small for hexagonal paraffins and orthorhombic or monoclinic paraffins.[33] It is thus perhaps acceptable to keep the traditional name "rotator" phase for the low temperature hexagonal phase of the paraffins (with a low concentration of conformational disorder, and with the understanding that the rotation is not that of a rigid zig-zag chain, but a segmental twist).

## 3.3 CONCLUSIONS

The present detailed simulation of the structure and dynamics of a chain crystal at constant pressure has illustrated the fundamental atomistic, picosecond, and large-amplitude motion. Due to the simplification of the geometry of the $CH_2$-groups only the hexagonal phase could be analyzed. The dominant motion at the root of the hexagonal structure dynamics could be shown to be a picosecond, segmental twist that, coupled with long-wavelength intermolecular, transverse vibrations, leads to a dynamic nanometer-scale domain structure. Conformational *gauche* defects have been found, in good agreement with experiment. These are, however, only for the high-temperature phase of polyethylene of sufficient concentration to make the crystal truly conformationally disordered (condis crystal). The quality of the simulation is sufficient to give results in close correspondence with experiment for density, heat capacity, melting, defect concentration, and sound velocity.

# CHAPTER 4

# ATOMISTIC DETAILS OF DISORDERING PROCESSES IN SUPERHEATED OR CONSTRAINED POLYMETHYLENE CRYSTALS

Polymer crystals exhibit inherently slow melting that leads often to superheating of larger crystals before fusion is complete.[57,150] Reorganization and recrystallization, as well as relaxation of strained tie molecules, may further obscure the melting process. Only well-crystallized, extended-chain crystals of polymers melt slowly enough so that the melting kinetics can be followed via microscopy, such as was done in the studies of melting for polyethylene, poly(tetrafluoroethylene), polymethylene, selenium, and polyoxyethylene.[151] These experimental methods were, however, limited to heating through conduction from the outside of the crystal and provided no atomistic details of the structural and dynamic changes that occur during melting from the superheated state. Even more important is the understanding of a superheated crystal for the description of laser-induced melting.[152] Computer simulations of melting from the superheated state should provide the means to obtain such information. Only recently has sufficient computer power become available for simulation of the beginning of the melting processes.

Single chain MD simulations of the mechanism and kinetics of melting processes in a polyethylene-like crystal showed that the end-to-end distances and radii of gyration had during melting a simple dependence on time.[16,17] The melting rate was found to increase with increasing temperature and decrease with increasing molecular length[16,17] and could

increase or decrease with increasing number of chain folds depending on the level of superheating, $\Delta T_m$ (= temperature – equilibrium melting temperature).[17]

In order to gain the information on the melting and crystallization processes on an atomistic level, the simulations have been extended to longer times using the unconstrained Model A (*i.e.* simulating constant, zero pressure dynamics) and the full or partial surface-constrained Model B, presented in Chapter 2.

## 4.1 RESULTS

In the unconstrained models, the simulations were carried out starting with $CH_2$-chains, as before, in orthorhombic (ORTH) or monoclinic (MONO) structures, as has been discussed in Chapter 3. The models are illustrated in the *x*-*y* projection in Fig. 1b.

In the surface-constrained models, the outermost chains are frozen, (*i.e.* are not permitted to participate in any motion, but contribute to the van der Waals interaction with the dynamic chains). Three different cases of simulations were carried out: four-side constraint (4-SC) in which layers of the surface chains of both of the *x*-*z* and *y*-*z* surface planes in Fig. 1b are static; three-side constraint (3-SC) in which two surface layers of the chains on *y*-*z* surface planes and only one side of *x*-*z* planes are static; and two-side constraint (2-SC) in which two surface layers of the chains, one in a *x*-*z*-plane and one in *y*-*z*-plane are static. The chain ends of the dynamic chains are not constrained, *i.e.* the chains are free to diffuse out of the *x*-*y*-plane. The Lagrangian operator *L* for the system has been described Chapter 3.

To start the simulation, the crystal was, as before, heated to a certain temperature by randomly distributing an appropriate set of momenta among the atoms of the dynamic chains in the crystal. The simulations were then run for 15–100 ps. The nonbonded interactions were cut off at 1.0 nm to shorten the computation time. The error of the integrations was controlled by the RKH solver[137] to be less than $10^{-4}$ using the CRAY/X-MP at Oak Ridge National Laboratory.

The temperature and density are calculated using the same methods described in Chapter 3. The information on the initial crystal structure, the constraint type, the simulation time, and the temperature-range are indicated in Table 7.

Figure 15 shows examples of temperature and density as a function of simulation time. The temperature plots of unconstrained ORTH and MONO overlap, the densities show a small difference. After about 10 ps, after steady state is reached, the temperature keeps decreasing continuously. This decrease is caused by the cumulative truncation errors in numerical integration, mainly due to the need of frequent updating of the neighbor-list because of motion out-of or into the 1.0 nm range due to the large-scale motion observed in these high-temperature simulations. The decrease in temperature due to macroscopic melting is a minor effect because of the limited amount of surface melting observed. Ultimately, the temperature drops below the melting temperature. It is thus possible, due to the limit in the computation method, not only to analyze the behavior of a superheated crystal, but also to study the beginning of recrystallization.

The spatial coordinates were plotted every picosecond and animated with the *MacroMind Director* program for a study of the structure change in time evolution. A

movie on VHS video is available for inspection and was presented for the first time in July 1992. Figures 16 and 17 show selected time-temperature sequences in the *x-y* projections of the ORTH and MONO crystals. Surface melting, progressive disordering, following by recrystallization and renewed ordering is visible.

To see the details of the motion of each chain from their initial positions, spatial plots were taken for each layer of the crystal array. For instance, the bottom 8 chains of the orthorhombic crystal in Fig. 1b are considered to be the first *x-y* layer (surface layer) and subsequent layers are treated accordingly. A printout of the *x-y*-projections of these layers avoids the overlapping seen in the overall crystal *x-y* projections of Figs. 16 and 17 (caused by large amplitude of twisting and bending motion of the chains). Figure 18 shows some of these projections. Figure 18a illustrates the *x-y* projection of the chains in the center layer of the ORTH crystal and Fig. 18b MONO crystal. Figures 18c and 18d show the orientation of surface chain layers of the ORTH crystal and MONO crystals. Times and temperatures are listed in the figures.

Many $CH_2$ groups are found to leave their initial positions within the lattice during the simulations. The displacements from the initial lattice positions exceed the unit cell dimension. Figure 19 shows the change in coordinate of the individual $CH_2$ units in the ORTH crystal from their initial structure of Fig. 1b (Run D05, Table 7). The number *n* in Fig. 19 indicates the position of a $CH_2$ unit. In Fig. 1b, n is counted in sequence from the bottom-left chain in the lowest layer (8 chains) to the right and then to the upper layers, always counting from the bottom to the top within the chain and from left to right within a layer.

The constrained crystals were observed to have a different dynamic behavior and crystal structures in which the large-amplitude bending motion is restricted, particularly in the vicinity of the static chains. When all surface chains (4-SC) are constrained, as shown in the *x-y* projections of the crystals shown in Fig. 20 (Run S14, Table 7). In the cases of a 3-SC crystal, as is shown by the *x-y* projections of a MONO crystal (Run S11 in Table 7) at 5 and 100 ps in Fig 21, some chains can be seen to move perpendicular to the chain axis toward the open side (unconstrained side). This occurs even at temperatures initially below the melting point, as indicated in Fig. 22 (Run S12, Table 7).

## 4.2 DISCUSSIONS

The simulation of a crystal at temperatures above the experimental melting temperature should give information on the initial melting process. Experimentally, *n*-paraffins with 50 carbon atoms (pentacontane $C_{50}H_{102}$) melts at about 365 K with a heat of fusion of 169.4 kJ/mol. Supplying sufficient energy to raise the temperature of the crystal above their melting temperature should lead to fusion until the temperature is reduced to the melting point. The equilibrium state expected is thus a partially molten and partially crystalline sample. The heat capacity of solid pentacontane in the 300-400 K temperature range is about 25 J/(K mol) per $CH_2$-unit,[34] so that in the simulation D05 that reached initially 465 K (see Table 7), about 2.5 kJ/mol $CH_2$ would be available for fusion of the superheated crystal. This should lead ultimately to an equilibrium at the melting temperature, 365 K, of about 70% melt and 30% crystal, since the heat of fusion is about 3.4 kJ/mol of $CH_2$.

Melting rate of polymers have also been studied experimentally.[151] Typical values of the linear crystal melting rate reached μm/s for about 10 K superheating, so that one would estimate a time of the order of magnitude of microseconds for the achievement of equilibrium, a factor of $10^4$ longer than the present simulation times. The time of randomization of an isolated single chain was simulated,[29] in turn, and found to take only picoseconds to nanoseconds.

These considerations lead to the conclusion that the present simulations can show the initial stages of melting only as far as they involve unimpeded surface chains. It will be shown, however, that considerable internal disorder is involved along with this initial surface melting. The internal disorder comes about because of the initial conditions that cause an instantaneous superheating. Experimental melting by heating through conduction, in contrast, would restrict the superheating because the interface would act as a heat sink and slow-down the superheating of the interior.

In the earlier simulations at lower temperature, presented in Chapter 3, we have seen that in unconstrained crystals the breathing mode of the crystal couples with the twisting mode of the molecular chains and the transverse mode of vibrations of neighboring chains, to result in an overall hexagonal crystal structure consisting of dynamic nanometer-size domains. This type of molecular motion is also observed in the early times of the high-temperature simulations in the unconstrained crystal, as can be seen in Figs. 16 and 17. Both simulations (ORTH and MONO) have the same temperature dependence (Fig. 15), which indicates that the kinetic parts of molecular motion are the same, regardless of initial crystal structure, as was also observed in the simulations

discussed in Chapter 3. The density fluctuations shown in Fig. 15 reveal a breathing mode of the crystal that reaches steady state after about 20 ps. The velocity of sound could be estimated from its frequency to be about 4 km/s, as before. In the beginning, the crystal excites a relatively large amplitude of the breathing mode giving the density a minimum since the initial positions are arranged according to the experimental lattice parameters at room temperature. Comparing ORTH and MONO, it is obvious from Fig. 15 that the two density curves stay separated throughout the whole simulation. This difference must be linked to somewhat different disordering mechanisms, since it was demonstrated earlier, that below the melting temperature, crystal structure as well as the density of crystals simulated starting from different initial positions are reaching the same steady state distribution function for the $CH_2$-groups (see Chapter 3).

As has been discussed in the previous simulations (Chapter 3) at low temperatures, the disorder increases with temperature. *Gauche* defects develop from about 231 K and concentrate mainly on the crystal surface. Twists in the chain, that are the most dominant feature, and cause the overall hexagonal crystal structure, are observed already at 57 K under unconstrained conditions. At about 315 K, the chains begin to show translational diffusion in the $z$–direction. In addition, the surface chains start to coil after leaving their original crystal positions. Beyond 365 K, the experimental melting temperature, the crystals show large amount of surface melting, as can be seen from Figs. 16 and 17.

A study of Fig. 16 indicates that the ORTH crystal shows less significant surface melting than the MONO crystal in Fig. 17. The melting starts in the present example of ORTH from the upper right of the crystal, propagating toward the lower left, which keeps

a domain of the original crystal structure and causes the chains in the upper right to align around it. At 42 ps (383 K), the lower left domain forms a distinctly hexagonal structure, while the upper right of the crystal is a strongly disordered domain. In-between these, there are two additional domains in the upper left and the lower right which have lost their original crystal structures, but are not fully randomized, and could be characterized as transition states. The hexagonal structure of the lower left domain seems to act as a crystallization site to compete with the disordering. It starts to lose its hexagonal crystal structure at about 55 ps (374 K). At 100 ps the lower left hexagonal domain has disappeared and the whole crystal has taken a completely new alignment as the temperature has decreased to 332 K, somewhat below the experimental melting point. The inner part of the crystal remains at about the same density throughout these changes (see Fig. 15), but note that the surface chains are not considered when determining density.

The MONO crystal changes somewhat differently from the ORTH crystal. It seems that it has initially undisturbed crystal sites located both in the left and right, as is shown in Fig. 17 after 14 ps. Major melting is distinctly preferred on the left and right surfaces of the crystal. Actually the surface chains start, as shown in Fig. 17, to peel off beginning at 10 ps and at 14 ps the surface chains start already to reorganize and form a disordered packing close to the surface layers, showing evidence of a competing process. At 23 ps, the temperature has decreased by only 3 K, but a hexagonal-like structure becomes obvious, and the overall structure becomes more similar to the ORTH

crystal. At a later time, the crystal follows the same sequence as that of ORTH. At 100 ps, the crystal is hardly distinguishable from that of ORTH at 100 ps (Fig. 16).

The mechanisms of the domain formation and structure change can be followed from trajectory plots as are sampled in Fig. 18. As has been documented in the previous chapter, torsional waves cause the molecular chains to bend and reorient, and chains in the same $x$-$z$-layer reorient to different degrees. The same is seen in Fig. 18. It becomes clear that the overall process, documented by Figs. 16 and 17, is accompanied by the reorientation of each individual chain and reorganization between neighboring chains. Overall, the crystals tilt and rotate. The multidomain structure is based on chains that are differently oriented in different domains and the dynamics of the domains give the appearance of "phase transitions".

The diffusion of the chains during the simulation is significant as can be seen in Fig. 19. The relative coordinate in $z$ indicates the magnitude of longitudinal translation and that of $x$ and $y$ represents the magnitude of the transverse translation. The majority of the atoms shift in by more than one unit cell dimension, suggesting that the crystal has been transformed to a structure entirely different from the initial one.

From the experimental superheating, it is obvious that the time frame in these simulations is still too short. However, these simulations might mimic the fast melting processes involved in laser melting.[152] In these cases the superheating is similarly instantaneous and homogeneous throughout the crystal.

The new observation from the simulations reveals that fusion of a superheated crystal involves two competing processes, a fast internal disordering and a slow conformational

disordering of the chains, starting from the outside of the crystal. As the temperature is lowered in the simulation (mainly due to computational energy loss), the conformational disordering of the surface chains is reduced, but the internal disorder is slower in perfection than it was in initial formation. The final state in Figs. 16 and 17 is much more disordered than in constant temperature simulations at similar temperatures, described in Chapter 3. Finally, it can be observed that the conformational disordering in the surface layer is rather quick to respond to the lowering of the temperature (see Figs. 16 and 17). Overall, the cooling through the melting process is an illustration of the Ostwald rule of stages that states that on crystallization, metastable states will be traversed before the final equilibrium state is reached.[57] The concentration of *gauche* conformations, because of their link with the skeletal vibration, reaches equilibrium in a very short time interval (picosecond or less).

The second set of experiments (series S in Table 7) was designed to test the effects of a more restrictive crystal environment as it may be found at higher pressure or within a larger crystal. The fully enclosed crystal, shown in Fig. 20 (4-SC), largely restricts the motion of chains in the $x$- and $y$-direction and the structure in the $x$-$y$ projection seems to remain close to orthorhombic and reduces the conformational defects with time. The pressure in the 4-SC crystal, due to the initial choice of room temperature chain separation, is estimated to be about 500 MPa at 410 K. However, there are still two unconstrained surfaces (the chain end surfaces) which allows migration to release the pressure build-up. Figure 23 shows the results of such chain migration in the $z$-direction on the 8th layer of 4-SC MONO crystal (Run S10 in Table 7) at 10 ps. The calculated

lattice parameters of the 4-SC crystals show that the average lattice parameters stay about the same as in the initial crystals. However, the lattice-parameter distributions are even broader than in the unconstrained crystals at similar temperature. Table 8 shows an example of the lattice-parameter distribution in the 4-SC ORTH crystal (Run S14 in Table 7). From Table 7 one can see that although the mean values (MEAN) are the same as for a perfect ORTH crystal, the range between maximum (MAX) and minimum (MIN) values are wider and the standard deviations (STD) are larger than those found in unconstrained crystals. This broad distribution can be explained by the fact that even though the overall dimension of crystal is fixed, there is still local disordering within the crystal in both the chain direction and perpendicular to the chains, as shown in Fig. 11. Besides, the segmental twist motion of the chains results in different setting angles within the same chain, so that a single chain can belong to different domains. Comparing the results to other molecular dynamics[30,112] and Monte Carlo simulations[108,109] in which the domains consist of rigid chains,[108,109] or in which only four well-defined orientations (setting angles) are allowed,[104] one finds that in the full MD simulation, the domain boundaries may go across the chains and, naturally the domains are dynamic and change with time.

In Figs. 21 and 22 one can see that the transverse migration of chains is accompanied by large-amplitude disordering and the transverse migration is not reversible. Figures 21 to 23 indicate that the chains tend to migrate to the unconstrained surfaces. This type of motion might be linked to the mechanism for the lamellar thickening during the crystallization.

## 4.3 CONCLUSIONS

In polymethylene crystals the molecular motion is sufficiently fast so that the beginning of melting and recrystallization can be followed via steady state arrangements in picosecond time scales which can, in turn, be followed by our molecular dynamic simulations.

In an unconstrained environment (the system is not subjected to external forces, such as pressure and container walls), the melting process of extended chain polymethylene crystals can be described as a sequence of three steps. First, disorder develops in the entire crystal and the crystal expands quickly to the steady state volume. Second, the primarily kinetic energy enables the translational and orientational motion. Finally, the crystal symmetry is destroyed and melting (or recrystallization) starts from the surface. The molecular motion is coupled between neighboring chains and the melting processes are cooperative throughout the entire crystal. Recrystallization is found to compete with the melting processes. The crystallization sites are found to already exist in the crystals at the melting temperature with the pseudo-hexagonal symmetry existing in a superheating crystals. This explains why the pseudo-hexagonal structure is often found experimentally at premelting.

The simulations confirm that the overall hexagonal structure consists of dynamic nano-domains and is the dominant form of unconstrained, flexible molecular crystals simulated by the united-atom model. The experimentally observed orthorhombic or monoclinic structures are the result of specific H–H interaction and can also be achieved by constraint. At high temperatures all molecules become mobile resulting in the so-

called "rotator phase", as demonstrated in the unconstrained model. The observed transverse and longitudinal motions contribute to the mass transport which can also be involved in the mechanism of lamellar thickening during the crystallization processes or on annealing.

# CHAPTER 5

# DIELECTRIC RELAXATION AND DEFECT MOTION IN POLYMETHYLENE CRYSTALS

Molecular motion is the key to understanding mechanical and dielectric relaxation in polymeric materials.[153] The relaxation is coupled to a steep decrease in modulus or dielectric constant over a short time or temperature interval when the material is subjected to a constant mechanical force or electric field. When the material is under oscillatory stresses or an alternating electric field, the relaxation is frequency dependent at a given temperature. The dielectric permittivity of a material is proportional to the polarizability of the material. In the presence of an electric field, nonpolar molecules may acquire an induced dipole moment as the result of electron polarization (caused by the distortion of their electronic distribution), nuclear polarization (from the distortion of nuclear positions), and interface polarization (if the material is not homogeneous, *e.g.* phase separation exists, electrons may accumulate at the interfaces). In response to an applied electric field, the induced dipole (as well as permanent dipoles in polar materials) tend to align themselves with the electric field, causing the weakening of the electric field, usually measured as dielectric loss tangent, tan$\delta$ (the ratio of the capacitor current to the resistor current). The alignment of the permanent dipoles depends on the molecular motion that can best be followed by molecular dynamics simulation.

The experimentally determined relaxation maxima in the dielectric loss *vs.* temperature or dielectric loss *vs.* frequency plot are usually labeled by $\alpha$, $\beta$, $\gamma$, *etc.* in the order of decreasing temperature or increasing frequency. The high temperature, or $\alpha$

relaxation in semicrystalline polymers is often associated with molecular motion in the crystal phase, as for example, in the dielectric and NMR relaxation in PE crystals.[79,80] The β transition is then connected to the glass transition and if there is a γ-transition it is usually linked to a local mode of large amplitude motion, usually present in the amorphous phase. Many experimental and theoretical studies have in the past been made to probe the mechanism of the α, as well as β and γ, relaxation processes in the paraffins and PE.[75,77,154-155]

Experiments described in the literature involve dielectric relaxation of ketone decorated paraffins[154,155] and oxidized or chlorinated polyethylenes.[156] The samples were dielectrically activated by dissolving long-chain ketone in paraffin crystals[154,155] or by oxidizing polyethylene in air at 160–170 °C or chlorinating polyethylene in a xylene solution.[156] It was found that the α peak disappeared on melting and reappeared on crystallization.[156]

The dielectric relaxation in ketone-decorated paraffins suggested the rigid rotation of the entire molecule about the long axis, and translation of one $CH_2$ to return the chain to crystallographic register.[154,155] This model fails since the observed activation energy is not proportional to the chain length for longer-chain compounds. Based on molecular mechanics calculation, a rotation-translation model (RR-TT) model has been recently developed to explain the α relaxation process of PE crystal and is in good agreement with experimental data.[25] It was also suggested that the involvement of kink defects in the relaxation process might lower the activation energy.[159]

Molecular dynamics simulation has been used before to follow the twist motion in polyethylene, in which a twist in one of seven dynamic chains surrounded by stationary chains was allowed to relax at different temperatures.[66] The results demonstrated that the initially introduced twist defect has a lifetime of no more than 2 ps and the formation of conformational disorder destroys the smooth twist quickly. The simulation was further extended by introducing an electric field to enhance the formation of twist in a carbonyl-decorated polyethylene chain, to copy the experiment,[156] leading to conclusions that a full reorientation of the dipole group requires a large electric field ($10^6$ V/cm) and the dipole can reorient much easier after a larger fraction of conformational disorder.[120]

The present simulation continues to follow the molecular motion during dielectric relaxation in the larger-sized polyethylene crystal model in the presence of an electric field. The initial crystal has orthorhombic structure, consisting of 9599 $CH_2$ units as united atoms and one C=O group as dipole. The model and potential functions have been detailed in the Model C in Chapter 2. In addition, more details in defect dynamics from the simulations on the unconstrained model have also been provided in the earlier chapters. The new results agree with the previous simulations presented refs. [66] and [120].

## 5.1 RESULTS

Three different dipole-decorated initial structures were analyzed: A, the C=O group is located at the center of the crystal; B, the C=O group is located at the seventh carbon in the center chain of the left surface layer of ORTH in Fig.1b; and C, the C=O group

is at the fifteenth carbon of the ninth chain of the bottom layer of ORTH in Fig. 1b. The orientation of the external electric field was always chosen opposite to the initial direction of the dipole. For each structure the trajectories were computed with four different dipole potential wells ($V_{ex}$, the interaction between the dipole and the external electric field): 2.092, 4.184, 8.368, and 16.736 kJ/mol (0.5, 1.0, 2.0, and 4.0 kcal/mol, respectively), and at four different temperatures: 55, 156, 230, and 330 K. Each simulation was run for 5 ps. The polar angles of the dipole moment on the $x$-$y$ plane projection were plotted against the simulation time and analyzed for the flipping time ($t_f$) at which the polar angle of the dipole moment varies by 180°. The results are summarized in Table 9 in which NF (no flipping) represents a change of the polar angle of the dipole moment less than 180° within the simulation time.

## 5.2 DISCUSSIONS

The flipping of the dipole moment depends upon the temperature, the position of the dipole, and the strength of the electric field. At 55 K, dipole A did not flip with the chosen electric field strengths (run number 101 through 104), while dipole B and C flipped in all electric field strengths considered and the flipping time decreased as the electric field strength increased (run number 117 through 123). For dipole A the flipping time decreased with increasing temperature and electric field strength. However, dipoles B and C did not show the same trend as dipole A. For dipole B, the flipping time decreased with the electric field-strength, but seemed to be independent of temperature. The flipping time of dipole C seemed to increase with electric field strength and decrease

with temperature.

For the high temperature case where the α relaxation occurs, the crystal has already transformed itself to the "rotator phase". As it has been discussed in Chapters 3 and 4, the "rotator phase" has a dynamic global defect due to constant segmental twist motion. By dynamic global defect it is meant that the overall crystallographic symmetry with specific chain-chain interaction has been lost and the crystal has broken up into multi-domains that undergo dynamic exchange. Figures. 24 and 25 show the average setting angles of each chain (averaged *x*-*y* projection of each chain) after 5 and 10 ps, respectively, from the Run 9 in Table 3. At 5 ps, most chains tend to align parallel with the *x* axis, causing the expansion in the *x*-dimension and shrinkage in the *y*-dimension, whereas at 10 ps most of the chains tend to change their alignment 90°, resulting in a shrinkage in the *x*-dimension and expansion in the *y*-dimension relative to that at 5 ps. Macroscopically, the overall result of the domain exchange has been observed in the density fluctuations characterized by the breathing mode already discussed in Chapter 3. From 5 to 10 ps, as is shown in Figs. 24 and 25, one can see that not only the setting angle changes, but also each lattice dimension change with time. The results, shown in Figs. 24 and 25, are simplified in two dimensions. There is no clear domain boundary, as demonstrated in two-dimensional MC simulations by Yamamoto.[108,109] The reason is that a chain may tilt, bend, or orient in segments with different degrees. In a three-dimensional view for the domain exchange, one can compare the result with the projection perpendicular to the chain axis as shown in Fig. 11 through which one can see that a chain could belong to different micro-domains and participate, in segments, to

different domain-exchanging at the same time due to the nature of twist motion demonstrated in Fig. 10.

Besides the multi-domain type defect, described above, various other types of defects have been observed to exist in the "rotator phase" and schematically illustrated in Fig. 26. The buckling defect in Fig. 26a is similar to the Reneker defect, but it exists with coupling to neighboring chains. A small fraction of *gauche* defects form and disappear, but no kink motion is observed.

The longitudinal diffusion, as illustrated in Fig. 26c, is found to be the result of the coupling of rotation-translation as was proposed by Mansfield and Boyd.[25] However, in these simulations, it is observed that all chains participate in rotation, as has been observed in NMR experiments, and contribute to overall disordering, and the twist motion is not necessary to be smooth. In addition, there is an accompanying chain-bending, as is shown in Fig. 10, so that it is not necessary to have a chain twist of 180° to return to crystallographic register, as in the molecular mechanics calculations. Compared to the dynamic simulations, defect models proposed by Reneker,[75] Boyd,[80] and Pechhold[77] are still too ordered and localized.

In addition to the twist shown in Fig. 10, the chain has substantial diffusion in the chain direction, as can be seen from the plot of its $z$-component of the center-of-mass as a function of time, shown in Fig. 27. The LAM motion of the chain in Fig. 10 is indicated by its end-to-end distance as a function of time, shown in the solid line in Fig. 28. The dotted line in Fig. 28 is for the chain on the surface of the same crystal, for comparison. It seems that the longitudinally translational motion is coupled to the LAM

motion.

Rotation and LAM motion are not always coupled to give rise to longitudinal diffusion. At temperatures as low as 57 K (Run 6 in Table 3), it has been observed that the LAM motion causes net longitudinal diffusion within one picosecond interval before any rotation occurs. The magnitude of the diffusion has been observed to be $\leq$0.127 nm in one picosecond interval at 57 K. It is suggested that the coupling or rotation may contribute to the magnitude of longitudinal diffusion.

## 5.3 CONCLUSIONS

The interaction of a dipole moment in the crystal with an electric field does not show simple relationship, rather, it is complicated. This is due to a variety of dynamic defects and coupling of the molecular motions. It is over-simplified to describe the $\alpha$ relaxation process by a single, localized defect model. Instead, various types of molecular motions, such rotational, translational, and bending motions are involved in the $\alpha$ relaxation process. At high temperature, the molecular motions are coupled between modes and between neighboring chains as the results of domain motion and breathing mode motion. In general, the $\alpha$ relaxation process involves the dynamic global defect.

# CHAPTER 6

# DYNAMICS AND STRUCTURE SIMULATION OF POLYMETHYLENE CRYSTALS WITH EXPLICIT HYDROGEN ATOMS

Due to the limit of computer power, united atom models in which hydrogen atoms are implicitly included, have been commonly used in MD simulations of polyethylene-like crystals, especially in the simulations of disordered phases. Explicit inclusion of hydrogen atoms in the crystal can be expected to increase the stiffness of the molecular chains. There were some MD simulations of polyethylene-like molecules with explicit hydrogens, however, these included some other sacrifices, such as decreasing the crystal size or freezing some mode of motion.[30,160,161] For a better understanding of the applicability of united atom models, it is necessary to simulate the same size crystal with explicit hydrogens while all modes of motion remain active.

In this chapter, the results of simulations of an unconstrained polymethylene crystal consisting of 9,600 carbons and 19,200 hydrogens (total 28,800 atoms) will be presented. The physical size of the crystal, the distance of nonbonding interaction cutoff, and the error-tolerance of the integrator are the same as that used in the united-atom simulations presented in Chapter 3. All modes of motion, including the motion involving hydrogens, are allowed. The details of the model and the potential functions have been described as Model D in Chapter 3. The equations of motion were solved on the UTK VAX/9000 computer using an RKH integrator[137] with restart/checkpoint capability. It took about 56 to 86 hours CPU time per picosecond, depending on the how occupied the computer is

(the VAX/9000 CPU time depends on how many persons are engaging the computer at the same time).

## 6.1 RESULTS

Three simulations for different temperatures were carried out on a crystal with chains initially sitting in orthorhombic lattice positions, as have been described as ORTH in Chapter 3. In the initial structure, the C–H bond length is 0.1069 nm, the C–C bond length is 0.153 nm, the H–C–H bonding angle is 107°, and the C–C–C bonding angle is 112°. To initiate crystal temperature, a certain amount of momentum is properly scaled and split for the sets of carbon and hydrogen atoms and distributed among carbons and hydrogens guided by a random number generator so that there is negligible net angular momentum, and the system is heated up homogeneously.

The results of temperature, density, and *gauche*-bond concentration as a function of time are listed in Tables 10 and 11. The radial distributions as a function of time in three simulations are shown in Figs. 29 to 31.

By studying the snapshots of spatial plots of the whole crystal in each picosecond, it was observed that the crystal deviates from its initial structure in all simulations in the manner that chains moved laterally in different degrees and rotated. In all cases, the crystal shrinks in the $y$-direction for more than one $b$ lattice dimension and expands slightly in the $x$-direction for less than half an $a$ lattice dimension. The snapshots in the $x$-$y$ projection of the whole crystal at the end of each simulation are shown in Figs. 32–34. After 2 picoseconds of simulation time, the crystal structure does not show

significant time dependence.

To analyze how much each crystal deviates from its initial structure, the standard deviation was calculated using Eqs. (53)–(57) shown in Chapter 3. The results are shown in Table 12. The lattice parameter distributions on the crystal structure were calculated in each picosecond and the results are shown in Tables 13–15. Figure 35 gives an example of a histogram of lattice parameters in the crystal structure in the simulation XR04 after a 7 ps simulation.

After about 2 ps, most of the molecules align parallel along the *y*-*z* plane and then stabilize. Figure 36 shows for the simulation XR04 the average setting angle of each chain (the coordinates of 50 carbons in each chain are averaged into a single C–C and then projected in *x*-*y* plane). To reveal the segmental twist motion that might affect the average setting angle in Fig. 36, the spatial coordinates of the crystal were also plotted in *x*-*z* projection layer by layer. Little large-amplitude motion is observed after 2 ps simulation. Figures 37 and 38 show the *x*-*y* projections of the surface and the center layers as a function of time in simulation XR04.

To characterize the formation, distribution, and the motion of conformational defects, more detailed information on the positions and life-time of each *gauche* conformations is listed in Table 16. In Table 16 each position of *gauche* is labeled by the three-dimensional matrix indices, *ix*, *iy*, and *iz* which represent the position of each torsional bond (between four consecutive carbons). The chain position is established by counting *ix* from left to right and *iy* from bottom to top in Fig. 1b, and *iz* indicates the position of the torsional bonds along the chain, for example $iz = 1$ marks the torsional bond $C_2$–$C_3$.

The life-time of each *gauche* bond can be estimated by finding the same number of $n$ in different time steps.

## 6.2 DISCUSSIONS

The simulations show that temperature and density stabilize quickly with only small fluctuations as can be seen in Table 10. This quick stabilization is also indicated by the radial distributions shown in Figs. 29–31. The system reaches steady-state after 2 ps at all temperatures. Compared to the united-atom results, the g($r$) plots show longer-range correlation.

As has described in Chapter 3, the densities of Table 10 were calculated with the box-sampling method. The densities with explicit hydrogens are larger than measured by X-ray diffraction at room temperature. For the simulations XR01 and XR02 this increase in density is partially due to the fact that the system is at a lower temperature. However, the magnitude of the density increase is too high. In the simulation XR04 with the temperature about 15 K above room temperature, there should be only a little change from the experimental density of 1.00 Mg/m$^3$. To check if this discrepancy is inherent in the computation method, an alternative method of density calculation, based on the average lattice parameters has been tried and the results are compared in Table 11. The two methods of density calculation yield comparable results. Compared with the volume of the initial structure of PE (ORTH), there is still about a 5% volume decrease in RX04.

Hydrogen–hydrogen interaction plays an important role in close packing of hydrocarbons.[57] A projection-to-hollow principle has been suggested before by geometric

analysis in close packing.[148] By this principle, a hydrogen of one molecule must project into the hollow created by the hydrogens in the neighboring molecules. The shape of hydrogens determines the packing. Different sizes of van-der-Waal radus of hydrogen atoms give different packing parameters.[57] The nonbonding interaction potentials in Eq. (18) was revised from the Williams set IV[162a] to fit vibrational frequencies, but the shape of atoms was still assumed to be spherical. The actual nonspherical shape of bonded hydrogens could caused the difference between the calculated and experimental density.[57] Due to thermal motion and large errors in determining hydrogen positions by X-ray diffraction, it is difficult to measure the bonded hydrogen shape precisely.[162b] The repulsion parameters $b$ and $c$ in Eq. (18) are highly correlated so that it is difficult to derive independent values.[162b] In practice, these parameters are based on some reasonable estimation, such as modulus[162a] and vibrational frequencies.[133]

The spatial plots in Figs. 32–34 and the disorder parameters shown in Table 12 indicate that these systems are more ordered phases and do not increase as much in disorder with temperature as the implicit hydrogen models. As pointed out in Chapter 3 the latter simulation should be looked upon as representing the hexagonal, more disordered phases. Although there is an increase of *gauche* concentration with temperature shown in Table 10, the *gauche* bonds do not cause the disordering of the entire crystal. They are mainly located on the surface of the crystal, as will be discussed later.

The lattice parameter distributions shown in Tables 13–15 and Fig. 35 indicate that the crystals also approach average dimensions close to hexagonal. However, the crystal

is different from the hexagonal "rotator phase" simulated with the models of Chapters 3 and 4 in that the majority of the molecular chains have constant setting angles and do not show significant rotations (see Figs. 36 to 38). The average hexagonal dimensions are due to the fact that the crystal consists of domains of different lattice dimensions.

A transition occurs at about 2 ps from the initial orthorhombic setting angles of the $CH_2$-chains to a structure with nearly parallel chains. The new phase is stable for the rest of the simulation time. Not much further disordering or larger-amplitude rotations would be expected at longer times since, for example, in Figs. 36 to 38 there is little motion, especially in the interior region of the crystal. The initial rotational change occurs in about 2 ps, if the system were not stable, the further disordering and rotation should have been observed within the 10 ps simulation time frame.

Table 16 indicates that all *gauche* bonds exist in the surface of the crystal, either toward the chain end or in the surface chain. A significant difference from the previous simulations is the relative longer life-time of the *gauche* bonds. It is interesting to note that even though the crystal has a high degree of order, as many as 7 *gauche* bonds per chain can exist in the surface chain of the crystal.

## 6.3 CONCLUSIONS

Compared with the implicit hydrogen simulations, a different dynamics and different structural changes have been observed in the explicit hydrogen modeling. The molecules are stiffer, and the motions are slower. No significant longitudinally translational motion, bending of molecular chains, and global disordering occur at temperatures up to about 315

K. Both systems show changes in their structure at low temperatures, 57–110 K, however, the change in the explicit hydrogen system occurs from an orthorhombic phase to a parallel chain arrangement instead of to the hexagonal "rotator phase".

The similarity in both implicit and explicit hydrogen systems is found in the temperature at which *gauche* conformations start to appear, the magnitude of the *gauche* concentration, and in the distribution of *gauche* bonds. The life time of *gauche* bonds in the explicit hydrogen system is about three time longer.

To simulate the high temperature "rotator phase" of paraffins and the high pressure hexagonal phase of PE, the implicit hydrogen models are more efficient. However, higher accuracy of simulations for information about dynamics and the structure of the ordered phases, incorporation of hydrogens, including the hydrogens in methyl groups for paraffins, would be necessary.

# CHAPTER 7

# CHAOS IN A POLYMETHYLENE CRYSTAL

Dynamic systems with nonmonotonic evolution, such as oscillation and vibration, can be characterized to be one of three different types: periodic, quasiperiodic, and aperiodic (or nonperiodic). These three types of dynamics can be distinguished by their power spectra which show only one frequency in a periodic system, more than one frequency in a quasiperiodic system, and a continuous spectrum in an aperiodic system. A power spectrum is the Fourier transform of the autocorrelation function of the signal as a function of frequency. If its power spectrum contains a continuous part (a broad band) regardless of the possible presence of peaks, a dynamic system is chaotic.[163] An extensive review on chemical chaos is available in the literature.[164]

The classical mechanics of Hamiltonian systems of coupled oscillators, such as those of vibrating molecules, has been the subject of intense study in recent years. It is now commonly accepted that three different regimes of the dynamics exist: (a) a regime where the classical motion is largely quasiperiodic, (b) a mixed regime of quasiperiodic and chaotic motion at different initial conditions, and (c) a regime of largely chaotic motion.[164]

Chaos can be characterized by an underlying order that consists of an infinite number of unstable periodic motions which shows a strange attractor: no point or pattern of points ever recurs in the plot of time evolution of a chaotic system. In fact, the time autocorrelation function goes to zero in a finite time which means the loss of memory of the signal with respect to itself, so that one cannot make long-time predictions. That is

to say, the use of knowledge of the state of the system for an arbitrarily long time can not predict its later evolution.[163] However, once a regime of chaos is characterized, one can find ways to control chaos by small perturbations to maintain a chaotic system in a stable, periodic state. The controlling of the most well-known chaotic chemical system, the Belousov-Zhabotinsky reaction (the cerium ion-catalyzed oxidation of malonic acid by acidified bromate), has been accomplished recently.[165]

The dynamic nature of the disordered phases of the paraffins and PE has become an object of importance. With increasing excitation or coupling parameters in a system, the transition from quasiperiodic to chaotic motion is furthered.[164] The soliton approach, as has been discussed in Chapter 1, implies that the system is deterministic. However, as was shown before, the vibrational motion is anharmonically coupled,[14] so that the system will become chaotic and the condition underlying soliton wave propagation is destroyed.[66] A full understanding of the dynamic nature of long-chain molecular systems awaits the quantitative characterization of the degree of chaotic behavior.

For systems with two coupled oscillators, there are several different methods that can distinguish chaotic from quasiperiodic motion:[164] (1) The phase-space volume method: A quasiperiodic trajectory occupies only a limited number of the energetically allowed phase space volume elements, while the chaotic trajectory appears to occupy all, or almost all of them. (2) The function-average method: comparing the time averages of functions of the dynamical variables and microcanonical phase space, the averages would not be the same in the quasiperiodic regime, but the same or nearly the same in the chaotic regime. (3) The Noid method: a method of differentiating the two types of classical

motion introduced by Noid *et al.*,[164] involves looking at the frequency spectrum of a dynamic variable or correlation function for a trajectory or for a set of trajectories. (4) The zeroth-order mode method: when energy is initially placed in some zero-order mode for any trajectory, that model energy undergoes regular oscillations in the quasiperiodic regime, but decays intramolecularly in the chaotic regime. (5) The Lyapunov exponent method: divergence of two nearby trajectories (with small perturbation) consists of a linear increase with time in the quasiperiodic regime, but an exponential increase with time for chaotic motion. (6) The Kolmogorov method: method (5) led Kolmogorov to define an entropy of the trajectory which has been found to change fairly rapidly at a critical energy where the dynamics change from largely quasiperiodic to largely chaotic. In practice, one does not numerically calculate the Kolmogorov entropy, but rather an approximation to it, called the *K*-entropy or an entropy-like quantity.

For many-body systems, the characterization of chaos becomes more difficult since for large numbers of degrees of freedom, several of these methods are not applicable and it is computationally difficult to calculate acurate trajectories. For our preliminary study to probe the chaos in a polymethylene system, the Lyapunov exponent method was used, which is a phase-space averaging technique that has been proposed in a recent publication for a system with several degrees of freedom.[166]

For two close trajectories, the phase-space separation d($t$) can be calculated and plotted as a function of time $t$. If d($t$) depends on $t$ exponentially, d($t$) = $e^{\lambda t}$, then the system is said to be chaotic. The exponent $\lambda$ is called Lyapunov exponent whose sign characterizes the type of attrator and whose magnitude measures how fast the trajectories

diverse. The result presented in this chapter involves the calculation of the exponential separation of two close trajectories in a polymethylene crystal of 9600 atoms (28,800 degrees of freedom).

## 7.1 RESULTS

Two sets of trajectories were calculated for the ORTH unconstrained crystal, described as Model A in Chapter 2, with a small perturbation in the initial total momentum inputs. In this calculation, the potential cut-off in nonbonding interactions and the tolerance of integration error have been controlled to the same degree as in the simulations presented in Chapter 3 and the temperature of the system is about 5 K. The perturbation in the initial total momentum for the trajectories in runs 1 and 2 is 0.01% (initial inputs are 1.00000 and 1.00010, in computer units of Table 2, respectively). The simulations were run for 2 ps with trajectory output (Cartesian coordinates) at each time step (0.05 ps).

The averaged trajectory separation between the two runs, d($t$), is calculated with the following equation:

$$\mathrm{d}(t) = \left[ \sum_{i=1}^{9600} (x_1 - x_2)_i^2 + (y_1 - y_2)_i^2 + (z_1 - z_2)_i^2 \right]^{1/2} \qquad (58)$$

where $x_1$, $x_2$, $y_1$, $y_2$, $z_1$, and $z_2$ are the Cartesian coordinates of the same atom $i$ at the same time step $t$ in runs 1 and 2, respectively. Figure 39 shows the plot of d($t$) as a function of time $t$.

## 7.2 DISCUSSIONS

As it can be seen in Fig. 39, an exponential increase of $d(t)$ with time has become obvious within 2 ps. In this simulation, the temperature of the system is relatively low (about 5 K), the main reason to cause exponential separation of the nearby trajectories lies in the coupling effect.

Previously, the system with maximum number of atoms, in which the phase-space trajectory separation technique for calculating Lyapunov exponent was applied, was about 20.[166] The validity of this technique to the system containing as many as 9600 atoms needs justification which is beyond the scope of this dissertation. However, the result is consistent with the chaotic nature of the molecular system in disordered phases,[14,66] and indicates the importance of the study of chaos in polymer systems. If the systems would have been quasiperiodic, they would exhibit a linear separation of two nearby trajectories.

In polymer systems, the question on how chaos affects the physical properties, such as dynamic disordering, microphase structure, vibrational spectra, X-ray and neutron scattering observations, and heat capacities, still remains largely unanswered. Characterization of chaotic regimes in polymer systems is an important first step toward this issue. Once the conditions such as pressure, temperature, and constraints that lead to chaos are known, one can have a better explanation of microscopic observations and can find a way to avoid chaos or control the system for desired purpose.

## 7.3 CONCLUSIONS

The result of this preliminary analysis agrees with other studies[14,66] that chaos exists in polymer systems. The average phase-space trajectory-separation technique for the Lyapunov exponent analysis offers a potential approach for the characterization of chaos in polymer systems. We note that only one other technique could be used to characterize chaos, *i.e.* the power spectral method. Most of the other techniques are not applicable. New methods for high dimensional systems are needed. To our knowledge there are no quantum mechanical studies of chaos for these systems. This work could provide new insight into heat capacities if accurate $g(\omega)$ could be calculated.

# CHAPTER 8

# CONCLUDING REMARKS

Using molecular dynamics simulations of polymethylene crystals at different temperatures and various conditions of constraint, it has been possible to observe the molecular motion of the picosecond time scale into macroscopically visible processes. This technique should become a standard analysis method as larger-scale computation becomes more easily available. For polymer crystals, the detailed tracing of crystal structure changes, the formation of chain defects and their diffusion through the crystals, and ultimately fusion and crystallization will permit a better understanding of the thermal, mechanical, and dielectric properties.

The simulations presented in this dissertation have demonstrated that the programming strategies by Noid and co-workers[19,20] using statement functions, modifying the usual chain-rule derivatives, applying appropriate vector identities, using closure relationships among the required derivatives and vectorizing a variable order, variable step, second order differential equation solver[19,20] are successful in saving computation time for the simulation of crystal sizes close to those experimentally found.[57] In general, good agreements with experimental measurements have been reached, such as the densities of crystals and speed of sound, conformational defect concentration and distribution, properties of the hexagonal rotator phase, mass transport and lamellar thickening, disordering and heat capacity increase, as well as surface melting and recrystallization.

A new level of the understanding of the details of molecular motion and nanophase structure has been achieved. The basic large-amplitude molecular motion and microscopic phase transition are on a picosecond time scale (1 ps = $10^{12}$ s), a factor at least $10^9$ away from direct macroscopic observation. This large-amplitude motion is distinguished from the vibrational motion that, by itself, does not lead to mass transport, but is the cause of the largest part of the heat content of a solid (typical vibration frequencies reach up to $10^{14}$ Hz). The hexagonal rotator phase is the time- and space-average of domains which are nanometer in dimension and are dynamically coupled to the breathing mode of the crystal. The molecular motion is largely coupled between its own different vibrational modes and those of the neighboring chains. The existence and the change of domains are evidence for corporative motion with the domains being the basic units of cooperative motion.

Disordering can begin in the hexagonal or pseudohexagonal phase at temperature about 100 K below the melting point, much lower than that measured experimentally. The reason is that in the disordered phase the majority of molecular chains undergo a constant, soft twist without forming *gauche* conformations. Since the motion of soft twist does not overcome the conformational barrier and is cooperative, it is the favored low energy path. This type of soft twist varies from the Reneker twist[75] and Utah twist.[25] in that, the latter ones are arbitrarily regulated one-time motion in order to return the chain to the crystallographic register since the models assume all the rest chains to be in order, so that higher energy is required. Since high energy is needed for each twist, it is not probable for further twist motion. That is the limitation of molecular mechanics

calculation.

The MD simulation is able to locate the position and calculate the life-time of *gauche* bonds exactly. Conformational analyses using IR and Raman spectroscopy indicate that *gauche* bond concentration increase exponentially toward the chain ends, but can not identify if those *gauche* bonds are distributed toward the center of the chain in the interior or only near the surface of the crystal. The importance of this information lies in the fact that it identifies different types of disordered phases. If only the surface chains contain *gauche* bonds, the overall disordering does not form a condis phase with *gauche* conformations, but disordering due to soft twists. When *gauche* bonds are found in the interior of the crystal, they should exist in the chains of interface of domains and the crystal may be separated by these interfaces into a multi-domain structure. The MD simulation results support the latter situation. However, the increase in *gauche* concentration goes parallel to the overall increase in disorder as temperature increases and explains the heat capacity increase.

Unlike the Pechhold *kink*-defect model,[77] the *kink* concentrations are found to be only a small portion of the total *gauche* concentration. The life-time of the *kinks* are short and they do not move through the chain or the crystal so that they are not the reason for chain diffusion. The chain diffusion is coupled to the longitudinal acoustic mode (LAM) or the coupling of twist with the LAM vibration. Transverse migration of the chains has been observed in these simulations when the crystals are partially constrained. The mass transport in the direction perpendicular to the chain axis does not involve conformational disordering, but large-amplitude torsional vibrations.

In the presence of an electric field, a 180° twist can be observed only if the electric field is strong enough. The relaxation processes are the result of various types of coupled molecular motion. It is not possible to describe the relaxation with a single type of motion.

The simulations have been able to see the beginning of surface melting on the superheating unconstrained crystals. A considerable internal disorder is involved along with this surface melting. Crystallization centers with hexagonal packing are found in the superheated crystals and compete with disordering, resulting in a reorientation of molecular chains and reorganization of the crystals.

The analyses of lattice-parameter distributions reveal the nature of short-time (picoseconds) and small-scale (nanometer dimensions) domain structures which are unable to be detected using X-ray diffraction. They might be the underlying factor for broadening of the X-ray diffraction pattern.

The explicit inclusion of hydrogen atoms in MD simulations slows down the molecular motion and narrows the scale of disordering. The potential functions used in this explicit-hydrogen simulation, results in a density higher than the experimental density. However, they yield a comparable *gauche* concentration and distribution to the experimental results. A rescaling of the nonbonding potential parameters is necessary to fit the experimental density. A change in symmetry may be needed to yield the observed orthorhombic symmetry.

At high temperatures, more molecules are involved in large-amplitude motion and the crystal expands, weakening the short-range intermolecular interactions. To save

computation time, the united atom model can be treated as the limiting case of the disordered phase of crystals at high temperature.

In the disordered phase, the molecular motion is chaotic. Applying chaos theories to disordered systems can yield a better understanding of the dynamic nature and structural changes.

In summary, this dissertation research was successful in application of MD simulations to the study of dynamics and structure of polymer crystals with the most realistic model to date. This achievement includes the generation of large-sized crystal trajectories and the analyses of trajectories, such as lattice-parameter distributions and disorder scaling, the insight into picosecond time-scale motion and animation, and the link between microscopic and macroscopic properties. This research required a large computational effort and involved many fields of science and technology, such as polymer science, classical mechanics, statistical mechanics, computer skills, and large-volume data processing. This dissertation can thus only report on some parts of the results in this relatively new field of research. Some future work is proposed to be done, and it is summarized below.

(1) In the simulations presented in this dissertation, the *gauche* conformations were found to exist only on the surface chains, whereas in earlier simulations[18,29] it was found that *gauche* bonds have no preference in positions in the crystal. The differences in the simulation models between the work in this dissertation and the earlier one[18,29] lie in the fact that different chain lengths and shapes of crystals were used. In the simulations of this dissertation, the chain length is 50% shorter and the crystal is close to square in the

*x-y* array instead of hexagonal. Further simulations should be carried out with different chain length and array to characterize the effect of physical model on conformational distributions and understand this discrepancy.

(2) The results presented in Chapter 4 show that the molecules undergo significant longitudinal motion (under pressure) and lateral migration (under partial lateral constraint). The type of motion, *e.g.* jump or diffusional motion, the rate of motion, and the way the holes being filled, need and are expected to be characterized from the recording of smaller time-step trajectories.

(3) The model for the electric-field induced defect motion (180° twist) was initially proposed to describe the relaxation process and lamellar thickening.[25] The preliminary result of the MD simulation showed that a large field-induced potential (4.1–16.7 kJ/mol, corresponding to $1.4\times10^6$ V/cm) is required to fully reorient the dipole on the time scale of the simulations. As the crystal size decrease, the field strength threshold decreases. However, this threshold is still relatively high compared to the low field strengths used in dielectric relaxation experiments. The discussion on the quantum tunneling effect that might be the reason to cause the molecular dynamics simulations to have high field strength has been reported elsewhere.[11] In fact, there is no need to have 180° rotation for dielectric relaxation. Even a few degrees of rotation will give a maximum dielectric loss tangent (tan $\delta$), but of lower intensity. A more quantitative correlation between the flipping or partial flipping of the dipole and the dielectric loss tangent could be established by measuring the relaxation of the defect when the electric field is turned off. However, the relaxation of the twist defect is generally in the direction that does not lead

to any lamellar thickening. Under the electric field, when a defect is created due to the flipping of the dipole, it will try to move to a more stable location if the defect is energetically not favorable and might result in a diffusion process leading to lamellar thickening. This mechanism can be studied by following the trajectories of the dipole as well as the dipole-containing chain. It is also of importance to see if the formation of defects and the relaxation process involve only soft twists or *gauche* conformations as well.

(4) For simulations with explicit hydrogen interactions, it is necessary to develop a proper set of potential functions that give correct crystal density and other properties. To do this, recently developed force field parameters by Karasawa, Dasgupta and Goddard III (KDG),[167] based on the experimental mechanical properties of the PE crystal, can be tested by the MD simulations. In KDG potential, cross terms of interactions were accounted for, and the importance of the coulombic interaction proposed by Williams *et al.*[162b] was taken into consideration. Based on the MD simulation results, the potential functions should be scaled to fit the density, heat capacity, and vibrational spectra of PE crystal at different temperatures. At the same time, other sets of force field parameters should be surveyed and compared with each other via MD simulation results. When a proper set of potential functions is derived, it is necessary to quantitatively characterize the effects of hydrogens on various macroscopic and microscopic properties so that for the MD simulations of those properties insensitive to explicit hydrogen interactions, united-atom models can be used to save computation time.

(5) To mimic many physical processes, one often needs to use constant-temperature and/or constant-pressure MD methods with dynamic constraints. To keep the temperature of the simulated system constant, one can rescale the velocity. This corresponds to a collision with imaginary heat-bath particles and is called velocity rescaling or stochastic method. However, the velocity rescaling might result in the deviation of trajectories from the Newtonian ones because too high a collision rate will slow down the speed at which the molecules in the system explore configuration space, and too low a collision rate means that the canonical distribution of energies will only be sampled slowly.[5]

Another way to simulate the constant temperature system is to use Nosé dynamics[128] or so-called extended system methods.[5] In the Nosé dynamics, the system is in contact with a thermal reservoir and the simulation is carried out for this "extended system".[168] Nosé introduced a special Hamiltonian in which a new dimensionless variable and its conjugated momentum with unit of action to represent that reservoir so that the microcanonical distribution becomes canonical. In the Nosé model the energy is allowed to flow dynamically from the reservoir to the system and back, the reservoir has a certain "thermal inertia" associated with it, and the whole technique is rather like controlling the volume of a sample by using a piston.[5] This method requires "time scaling," or equivalently "mass scaling" to carry out the momentum integration, so it complicates the interpretation of the corresponding Hamiltonian dynamics.[128]

Instead of introducing a new Hamiltonian, Hoover started out with new equations of motion by introducing a kind of "friction coefficient" to constrain the equations of motion.[128] The constraint is chosen so as to perturb the classical equations of motions as

little as possible by making the friction coefficient a Lagrange multiplier which minimizes the difference (in a least-squares sense) between the constrained and Newtonian trajectories. This method is called constraint methods,[5] or Nosé-Hoover mechanics.[128]

Further work is proposed to use dynamic constraints, such as Nosé or Hoover dynamics, for the simulations of constant-temperature and/or constant-pressure processes. This dynamic constraint method is especially important for the simulation of equilibrium melting processes. Imposing a periodic boundary condition is not suitable for melting simulation and the use of periodic boundary condition in the chain ends will arbitrarily hinder the formation of *gauche* bonds. However, the effect of periodic boundary condition in the lateral direction on the low temperature crystal structure could to be justified.

(7) When the problems of the full-atom force parameters are resolved, the major effort will be concentrated on the link between microscopic and macroscopic properties. With the trajectories of atoms in a crystal known, one can characterize crystal structure and phase transitions. Distributions of lattice parameters from the trajectory analysis has offered a new insight into the statistical description of a crystal. It is of importance to link the lattice-parameter distributions to X-ray diffraction results. A calculation of diffraction pattern from trajectories, as described in Eq. (32), will serve as guidance for the refinement of patterns of X-ray diffraction. Vibrational spectra can also be calculated from trajectories.[3a,11,13,118] The effects of crystal defects on the vibrational spectra can be given from these calculations. The results will help the vibrational spectrum analysis for defects.

(8) For a more quantitative characterization of chaos in polymer crystals, calculations of the Lyapunov exponent need to be carried out for the systems starting with a short, single chain, then going increasing chain length and crystal size, as well as to different constraint conditions.

# REFERENCES

# REFERENCES


1. H. Goldstein, "Classical Mechanics," Addison-Wesley, Reading, Massachusetts, 1980.

2. B. J. Alder and T. E. Wainwright,"Phase transition for a hard sphere system," *J. Chem. Phys.* **27**, 1208 (1957).

3. (a) D. W. Noid and G. A. Pfeffer, "Short time molecular dynamics simulation: Stressed polyethylene results," *J. Polym. Sci.: Part B: Polym. Phys.* **27**, 2321 (1989); (b) C. R. J. Counsell, J. W. Emsley, G. R. Luckhurst, D. L. Turner, and J. Charvolin, "Molecular dynamics of liquid crystals, the frequency and site dependence of spectral densities," *Mol. Phys.* **52** (2), 499, 1984; (c) D. Brown and J. H. R. Clarke, "Molecular dymamics simulation of an amorphous polymers under tension. 1. Phenomenology," *Macromolecules* **24**, 2075 (1991); (d) J. Gao and J. H. Weiner, "Computer simulation of viscoelasticity in polymer melts," *Macromolecules* **25**, 1348 (1992); (e) S. Yashonath, P. Demontis, and M. L. Klein, "Temperature and concentration dependence of adsorption properties of methane in NaY: a molecular dynamics study," *J. Phys. Chem.* **95**, 5881 (1991); (f) B. Jung and B. L. Schürmann, "Molecular dynamics simulations of phenyl-4-(4-benzoyloxy)benzoyloxybenzoate in the crystalline and nematic phase," *Mol. Cryst. Liq. Cryst.* **185**, 141 (1990); (g) P. V. K. Pant and R. H. Boyd, "Simulation of diffusion of small-molecule penetrants in polymers," *Macromolecules* **25**, 494 (1992); (h) J. Sonnenburg, J. Gao, and J. H. Weiner, "Molecular dynamics simulation of gas diffusion through polymer networks," *Macromolecules* **23**, 4653 (1990).

4. W. G. Hoover and W. T. Ashurst, "Nonequilibrium molecular dynamics," in "Theoretical Chemistry," (H. Eyring and D. Henderson, Ed.), Academic Press, New York, pp. 1-51, 1975.

5. M. P. Allen and D. J. Tildesley, "Computer Simulation of Liquids," Clarendon Press, Oxford, 1987.

6. M. L. Klein, in "Computer Simulation of Mater," (Peter Lykes, Ed.), American Chemical Society, Washington DC, 1978.

7. W. G. Hoover, "Nonequilibrium molecular dynamics," *Ann. Rev, Phys, Chem.*, **34**, 103 (1983).

8. G. Ciccotti and W. G. Hoover, Ed., "Molecular-Dynamics Simulation of Statistical-Mechanical Systems," North-Holland Physics Publishing, Amsterdam, 1985.

9. M. L. Klein, "Computer simulation studies of solids," *Ann. Rev. Phys. Chem.* **36**, 525 (1985).

10. E. Clementi, Ed., "Modern Techniques in Computational Chemistry: MOTECC™-89," ECSOOM, Netherlands, 1989.

11. B. G. Sumpter, D. W. Noid, and B. Wunderlich, "Computer simulation and modeling of polymeric crystals," *Trends. Polym. Sci.*, Submitted.

12. D. W. Noid, B. G. Sumpter, M. Varma-Vair, and B. Wunderlich, "Molecular dynamics results for a polyethylene-like crystal," *Makromol. Chem., Rapid Commun.*, **10**, 377 (1989).

13. D. W. Noid, B. G. Sumpter, and B. Wunderlich, "Molecular dynamics calculation of the density of states for poly(ethylene): Collective versus local modes," *Analytica Chimica Acta*, **235**, 143 (1990).

14. B. G. Sumpter, D. W. Noid, and B. Wunderlich, "Theoretical studies of the effects of anharmonicity on polymer dynamics: Temperature dependence of heat capacity," *Polymer*, **31**, 1254 (1990).

15. D. W. Noid, B. G. Sumpter, and B. Wunderlich, "Studies of the lamellar thickening process for polyethylene," *Polymer Communications*, **31**, 304 (1990).

16. D. W. Noid, G. A. Pfeffer, S. Z. D. Cheng, and B. Wunderlich, "Computer simulation of the melting process in linear macromolecules," *Macromolecules*, **21**, 3482 (1988).

17. B. G. Sumpter, D. W. Noid, B. Wunderlich, and S. Z. D. Cheng, "Molecular dynamics study of the rate of melting of a crystalline polyethylene molecules: Effect of chain folding," *Macromolecules*, **23**, 4671 (1990).

18. B. G. Sumpter, D. W. Noid, and B. Wunderlich, "Computational experiments on the motion and generation of defects in polymer crystals," *Macromolecules*, **25**, 7247 (1992).

19. D. W. Noid, B. G. Sumpter, and B. Wunderlich, "Molecular dynamics simulations of polymers: Methods for optimal fortran programming," *J. Comp. Chem.*, **11**, 236 (1990).

20. D. W. Noid, B. G. Sumpter, and R. L. Cox, "Computational strategies for molecular dynamics simulations of polymer processes: numerical integration schemes," *J. Comp. Polym. Sci.*, **1**, 161 (1991).

21. D. M. Small, "The physical chemistry of lipids: from alkanes to phospholipids. Handbook of lipid research," Vol. 4, (D. J. Hanahan, Ed.), Plenum Press, New York, 1986.

22. D. A. Dill and P. J. Flory, "Molecular organization in micelles and vesicles," *Proc. Natnl. Acad. Sci. U. S. A.*, **78**, 676 (1981); H. Wennerström and B. Lindman, "Micelles. physical chemistry of surfactant association," *Phys. Rep.*, **52**, 1 (1979).

23. A. Ben-Shaul, Y. Rabin, and W. M. Gelbart, "On the stretching of alkyl chains by nematics," *J. Chem. Phys.*, **78**, 4303 (1983).

24. D. B. Creamer, R. K. Pathria, and Y. Rabin, "Statistical thermodynamics of polyalkane-like chains in a uniaxial environment," *J. Chem. Phys.*, **84**, 476 (1986).

25. M. Mansfield and R. H. Boyd, "Molecular motions, the α Relaxation, and chain transport in polyethylene crystals," *J. Polym. Sci. Polym. Phys. Ed.*, **16**, 1227 (1978).

26. B. Wunderlich and J. Grebowicz, "Thermotropic mesophase and mesophase transitions of linear, flexible macromolecules," *Adv. Polym. Sci.*, **60/61**, 1 (1984).

27. B. Wunderlich, M. Möller, J. Grebowicz, and H. Bauer, "Conformational Motion and Disorder in Low and High Molecular Mass Crystals," Springer Verlag, Berlin, 1988 (*Adv. Polym. Sci.*, **87**).

28. D. W. Noid, B. G. Sumpter, and B. Wunderlich, "Molecular dynamics simulation of the condis state of polyethylene," *Macromolecules*, **23**, 664 (1990).

29. B. G. Sumpter, D. W. Noid, and B. Wunderlich, "Computer experiments on the internal dynamics of crystalline polyethylene: Mechanistic details of conformational disorder," *J. Chem. Phys.*, **93**, 6875 (1990).

30. J.-P. Ryckaert, I. R. McDonald, and M. L. Klein, "Disorder in the pseudohexagonal rotator phase of n-alkanes: molecular-dynamics calculations for tricosane," *Mol. Phys.*, **67** (5), 957 (1989).

31. M. G. Broadhurst, "An analysis of the solid phase behavior of the normal paraffins," *J. Res. Natl. Stand.*, **66A**, 241 (1962).

32. G. Mózes, Ed., "Paraffin Products: properties, technologies, applications," Elsevier, Amsterdam, 1982.

33. Y. Kim, H. L. Strauss, and R. G. Snyder, "Conformational disorder in crystalline n-alkanes prior to melting," *J. Phys. Chem.*, **93**, 7520 (1989).

34. Y. Jin and B. Wunderlich, "Heat capacities of paraffins and polyethylene," *J. Phys. Chem.*, **95**, 9000 (1991).

35. G. M. Stack, L. Mandelkern, C. Kröhnke, and G. Wegner, "Melting and crystallization kinetics of a high molecular weight *n*-alkane: $C_{192}H_{386}$." *Macromolecules*, **22**, 4351 (1989).

36. R. T. Morrison and R. N. Boyd, "Organic Chemistry," Fourth Eds., Allyn and Bacon, Inc., Boston, 1983.

37. A. Müller and W. B. Saville, "LXXXVIII. Further X-ray measurements on long-chain compounds (*n*-hydrocarbons)," *J. Chem. Soc.* **127**, 599 (1925).

38. S. Abrahamsson, B. Dahlén, H. Löfgren, and I. Pascher, "Lateral packing of hydrocarbon chains," *Prog. Chem. Fats Other Lipids*, **16**, 125 (1978).

39. A. A. Schaerer, C. J. Busso, A. E. Smith, and L. B. Skinner, "Properties of pure normal alkanes in the $C_{17}$ to $C_{36}$ range," *J. Am. Chem. Soc.* **77**, 2017 (1955).

40. A. Müller and K. Lonsdale, "The low-temperature form of $C_{18}H_{38}$," *Acta Crystallogr.*, **1**, 129 (1948).

41. S. C. Nyburg and H. Lüth, "*n*-Octadecane: A correction and refinement of the structure given by Hayashida," *Acta Crystallogr.*, **B28**, 2992 (1972).

42. A. E. Smith, "The crystal structure of the normal paraffin hydrocarbons," *J. Chem. Phys.*, **21**, 2229 (1953).

43. N. Norman and H. Mathisen, "Crystal structure of lower paraffins. V. Cell dimensions of nonane, decane, undecane, dodecane, tridecane, tetradecane, and hexadecane," *Acta Chem. Scand.*, **26**, 3913 (1972).

44. H. Mathisen, N. Norman, and B. F. Pedersen, "The crystal structure of low paraffins. IV. Refinement of crystal structure of pentane and octane," *Acta Chem. Scand.*, **21**, 127 (1967).

45. H. M. M. Shearer and V. Vand, "The crystal structure of the monoclinic form of *n*-hexatriacontane," *Acta Crystallogr.* **9**, 379 (1956).

46. P. W. Teare, "The crystal structure of orthorhombic hexatriacontane $C_{36}H_{74}$," *Acta Crystallogr.*, **12**, 294 (1959).

47. J. Doucet, I. Denicolo, and A. Craievich, "X-ray study of the 'rotator phase' of odd-numbered paraffins $C_{17}H_{36}$, $C_{19}H_{40}$, $C_{21}H_{44}$," *J. Chem. Phys.*, **75**, 1523 (1981).

48. J. Doucet, I. Denicolo, and A. Craievich, "Evidence of a phase transition in the rotator phase of the odd-numbered paraffins. $C_{23}H_{48}$ and $C_{25}H_{52}$," *J. Chem. Phys.*, **75**, 5125 (1981).

49. I. Denicolo, J. Doucet, and A. F. Craievich, "A study of the rotator phase of paraffins (III): Even-numbered paraffins $C_{18}H_{38}$, $C_{20}H_{42}$, $C_{22}H_{46}$, and $C_{26}H_{54}$," *J. Phys. Chem.*, **78**, 1465 (1983).

50. G. Ungar, "Structure of rotator phase in *n*-alkanes," *J. Phys. Chem.*, **87**, 689 (1983).

51. M. Maroncelli, S. P. Qi, H. L. Srrauss, and R. G. Snyder, "Nonplanar conformations and the phase behavior of solid *n*-alkanes," *J. Am. Chem. Soc.*, **104**, 6237 (1982).

52. L. Mandelkern, "Crystallization and Melting of Polymers," in "Comprehensive Polymer Science, Polymer Properties," C. Booth and C. Price, Eds., Pergamon, New York, 1989, Vol. 2.

53. K. Takimizawa, Y. Ogawa, and T. Oyama, "Thermal behavior of *n*-alkanes from *n*-$C_{32}H_{66}$ to *n*-$C_{80}H_{162}$, synthesized with attention paid to high purity," *Polym. J.*, **14**, 441 (1982).

54. J. N. Hay, "Thermal analysis of *n*-hectane," *J. Polym. Sci., Part B, Polym. Lett.*, **8**, 395 (1970).

55. G. Ungar and A. Keller, "Time-resolved synchrotron X-ray study of chain-folded crystallization of long paraffins," *Polymer*, **27**, 1835 (1986).

56. J. I. Kroschwitz, "Concise Encyclopedia of Polymer Science and Engineering," John Willey & Sons, New York, 1990.

57. B. Wunderlich, "Macromolecular Physics, Vols. I–III," Academic Press, New York, 1973, 1976, and 1980.

58. H. Tadokoro, "Structure of Crystalline Polymers," Robert E. Krieger Publishing Company, Malabar, Florida, 1990.

59. C. W. Bunn, "The crystal structure of long-chain normal paraffin hydrocarbons. The 'shape' of the $>CH_2$ group," *Trans. Faraday. Soc.*, **35**, 482 (1939).

60. P. R. Swan, "Polyethylene unit cell variations with temperature," *J. Polym. Sci.*, **56**, 403 (1962).

61. S. Kavesh and J. M. Schultz, "Lamellar and interlamellar structure in melt-crystallized polyethylene. I. Degree of crystallinity, atomic positions, particle size, and lattice disorder of first and second kinds," *J. Polym. Sci. A-2*, **8**, 243 (1970).

62. G. Avitabile, R. Napolitano, B. Pirozzi, K. D. Rouse, M. W. Thomas, and B. T. M. Willis, "Low temperature crystal structure of polyethylene: Results from a neutron diffraction study and from protential energy calculations," *J. Polym. Sci.*, **B13**, 351 (1975).

63. T. Seto, T. Hara, and K. Tanaka, "Phase transformation and deformation processes in oriented polyethylene," *Japan. J. Appl. Phys.*, 7 (1), 31 (1968).

64. (a). W. P. Slichter, "On the morphology of highly crystalline polyethylenes," *J. Polym. Sci.*, **21**, 141 (1956); (b). G. Ungar and A. Keller, "Effect of radiation on the crystals of polyethylene and paraffins: 1. Formation of the hexagonal lattice and the destruction of crystallinity in polyethylene," *Polymer*, **21**, 1273 (1980).

65. N. G. Parasonage and L. A. K. Staveley, "Disorder in Crystals," Clarendon Press, Oxford, 1978.

66. D. W. Noid, B. G. Sumpter, and B. Wunderlich, "Molecular dynamics simultion of twist motion in polyethylene," *Macromolecules*, **24**, 4148 (1991).

67. A. Müller, "An x-ray investigation of normal paraffins near their melting points," *Proc. R. Soc. London Ser.*, **A138**, 514 (1932).

68. J. D. Barnes, "Molecular reorientation and the 'rotator' phase transition in *n*-alkanes," Ph. D. dissertation, Catholic University of America, Washington, D. C., 1972.

69. B. Wunderlich, "Thermal Analysis," Academic press, Boston, 1990.

70. B. Wunderlich and J. Grebowicz, "Do condis crystals exist?" *Div. Poly. Chem. Am. Chem. Soc. Preprints*, **24**(2), 290 (1983); B. Wunderlich and J. Grebowicz, "Characrization of conformationally disordered crystals by DSC," *Am. Chem. Soc. Org. Coatings Appl. Polym. Sci. Preprints*, **50**, 114 (1984).

71. P. J. Flory, "Structural Mechanics of Chain Molecules" , Wiley (Interscience), New York, 1969.

72. T. M. Birshtein, O. B. Ptitsyn, "Conformations of Macromolecules" (Translated from the Russian by S. N. Timasheff and M. J. Timasheff) Wiley (Interscience), New York, 1966.

73. M. V. Volkenstein, "Configurational Statistics of Polymeric Chains" (Translated from the Russian by S. N. Timasheff and M. J. Timasheff) Wiley (Interscience), New York, 1963.

74. H. P. Grossmann, W. R. Pechhold, "The high temperature transition of polyethylene into a condis phase, described on the basis of the cluster-energy hypothesis (CEH)," *Colloid Polym. Sci.*, **264**, 415 (1986).

75. D. H. Reneker, "Point dislocations in crystals of high polymer molecules," *J. Polym. Sci.*, **59**, S39 (1962); D. H. Reneker and J. Mazur, "Crystallographic defects in polymers and what they can do," in "Computer Simulation of Polymers," (R. J. Roe edited), Prentice Hall, Englewood Cliffs, New Jersey, 1991.

76. D. H. Reneker and J. Mazur, "Small defects in crystalline polyethylene," *Polymer* **29**, 3 (1988).

77. W. Pechhold, S. Blasenbrey, and S. Woerner, "Eine niedermolekulare Modellsubstanz für lineares Polyäthylen. Vorschlag des 'Kinkenmodells' zur Deutung des $\gamma$- und $\alpha$-relaxation Prozesses," *Kolloid. Z. Z. Polym.* **189**, 14 (1963).

78. R. H. Boyd and J. A. Sayre, "Dielectric evidence for thermal creation of defects in polyethylene crystals," *J. Polym. Sci. Polym. Phys. Ed.*, **17**, 1627 (1979).

79. R. H. Boyd, "Relaxation processes in crystalline polymers: experimental behaviour – a review," *Polymer*, **26**, 323 (1985).

80. R. H. Boyd, "Relaxation in crystalline polymers: Molecular interpretation – a review," *Polymer*, **26**, 1123 (1985).

81. M. L. Mansfield, "An analysis of the dielectric α-relaxation of crystalline polyethylene in terms of solitons," *Chem. Phys. Lett.*, **69** (2), 383 (1980).

82. G. Zerbi and G. Longhi, "Conformational solitons or twistons in polethylene chains: Lattice dynamics and infrared spectra," *Polymer*, **29**, 1827 (1988).

83. N. J. Zabusky and M. D. Krukal, "Interaction of 'soliton' in a collisionless plasma and the recurrence of initial states," *Phys. Rev. Lett.*, **15**, 240 (1965).

84. A. S. Davydov, "Soliton in Molecular Systems," (Translated by E. S. Kryachko from Russian), Reidel Publishing Company, Dordrecht, Holland, 1985.

85. E. Infeld and G. Rowlands, "Nonlinear Waves, Solitons and Chaos," Cambridge University Press, Cambridge, 1990.

86. E. Fermi, J. Pasta, and S. Ulam, "Studies of non linear problems," in "Collected papers of Enrico Fermi," (E. Segré Ed.), University of Chigaco, **2**, 978-988 (1965).

87. A. Thyagaraja, "Recurrence phenomena and the number of effective degree of freedom in nonlinear wave motions," in "Nonlinear Waves," (L. Debnath Ed.), Cambridge University Press, 308 (1983).

88. W. P. Su, J. R. Schrieffer, and A. J. Heeger, "Soliton excitation in polyacetylene," *Phys. Rev.*, **B22**, 2099 (1980).

89. S. Takeno (Ed.), "Dynamical Problems in Soliton Systems," Springer Verlag, Berlin, 1985.

90. J. L. Skinner and P. G. Wolynes, "Transition state and brownian motion theories of solitons," *J. Chem.Phys.*, **73** (8), 4015 (1980).

91. G. Zerbi, R. Magni, M. Gussoni, K. H. Moritz, A. Bigotto, and S. Sirlikov, *J. Chem. Phys.* **75**, 3175 (1981).

92. R. G. Snyder, M. Macroncelli, S. P. Qi, and H. L. Strauss, "Phase transitions and nonplanar conformers in crystalline *n*-alkanes," *Science*, **214**, 188 (1981).

93. R. G. Snyder, M. Maroncell, H. L. Strauss, C. A. Elliger, D. G. Cameron, H. L. Casal, and H. H. Mantsch, "Distribution of gauche bonds in $C_{21}H_{44}$ in phase II," *J. Am. Chem. Soc.*, **105**, 133 (1983).

94. M. Maroncelli, H. L. Strauss, and R. G. Snyder, "The distribution of conformational disorder in the high-temperature phases of crystalline n-alkanes," *J. Chem. Phys.*, **82** (7), 2811 (1985).

95. K. A. Wood, R. G. Snyder, and H. L. Strauss, "Analysis of the vibrational bandwiths of alkane-ura clathrates," *J. Chem. Phys.*, **91** (9), 5255 (1989).

96. Olf, H. and Peterlin, A., "NMR study of molecular motion in oriented long-chain alkanes. III. Oriented n-$C_{32}H_{66}$," *J. Polym. Sci.*, Part A-2 **8**, 791-797 (1970).

97. G. Strobl, B. Ewen, E. W. Fischer, and W. Piesczek, "Defect structure and molecular motion in the four modifications of *n*-tritriacontane. I. Study of defect structure in the lamellar interface using small angle X-ray scattering," *J. Chem. Phys.*, **61**, 5257 (1974);

98. B. Ewen, E. W. Fischer, W. Piesczek, and G. Strobl, "Defect structure and molecular motion in the four modifications of *n*-tritriacontane. I. Study of molecular motion using infrared spectroscopy and wide-line nuclear magnetic resonance measurements," *J. Chem. Phys.*, **61**, 5265 (1974).

99. E. Ewen, G. R. Stobl, and D. Richter, "Phase transitons in crystals of chain molecules. Relation bewteen defect structures and molecular motion in the four modifications of *n*-$C_{33}H_{68}$," *J. Chem. Soc. Faraday Discuss.* **69**, 19 (1980)

100. B. Ewen and D. Richter, "Study of molecular motion in modification C of the *n*-alkane n-$C_{33}H_{68}$ by means of incoherent quasileastic neutron scattering," *J. Chem. Phys.*, **69**, 2954-2963 (1978).

101. J. Doucet and A. J. Dianoux, "Rotational diffusion in the rotator phase of n-alkanes," *J. Chem. Phys.* **81**, 5043 (1984).

102. F. Guillaume, J. Doucet, C. Sourisseau, and A. J. Dianoux, "Molecular motions in *n*-nonadecane $C_{19}H_{40}$: An incoherent neutron scattering study," *J. Chem. Phys.* **91** (4), 2555-2567 (1989).

103. G. Ungar, "Structure of rotator phase in *n*-alkanes," *J. Phys. Chem.*, **87**, 689 (1983).

104. G. Ungar and N. Masic, "Order in the rotator phase of n-alkanes," *J. Phys. Chem.* **89**, 1036 (1985).

105. G. Ungar, "From plastic-crystal paraffins to liquid-crystal polyethylene: continuity of the mesophase in hydrocarbons," *Macromolecules*, **19**, 1317 (1986).

106. P. E. McMahon, R. L. McCullough, A. A. Schlegel, "Molecular mechanics of point defects in polyethylene," *J. Appl. Phys.*, **38**, 4123 (1967).

107. R. L. McCullough, "An energy approach to the analysis of molecular motions in polymeric solids," *J. Macromol. Sci. Phys.* **B9**, 97 (1974).

108. T. Yamamoto, "Monte Carlo simulation of the crystal structure of the rotator phase of *n*-paraffins," *J. Chem. Phys.* **82** (8), 3791 (1985).

109. T. Yamamoto, "Monte Carlo simulation of the crystal structure of the rotator phase of *n*-paraffins. II. Effects of ratotion and translation of the rigid molecules," *J. Chem. Phys.* **89** (4), 2356 (1988).

110. J. J. Pablo, M. Laso, and U. W. Suter, "Simulation of polyethylene above and below the melting point," *J. Chem. Phys.* **96** (3) 2395 (1992).

111. J. Hahn, A. J. Pertsin, and H. P. Grossmann, "Monte-Carlo simulation of solid-solid transition to conformationally disordered state," *Macromolecules*, **25**, 6510 (1992).

112. J.-P. Ryckaert and M. L. Klein, "Translational and rotational disorder in solid *n*-alkanes: Constant temperature-constant pressure molecular dynamics calculations using infinitely long flexible chains," *J. Chem. Phys.*, **85** (3), 1613 (1986).

113. I. Zúñiga, I. Bahar, R. Dodge, and W. L. Mattice, "Molecular dynamics analysis of transitions between rotational isomers in polymethylene," *J. Chem. Phys.*, **95** (7), 5348 (1991).

114. K.-J. Lee, W. L. Mattice, and R. G. Snyder, "Molecular dynamics of paraffins in the *n*-alkane/urea clathrate," *J. Chem. Phys.* **96** (12), 9139 (1992).

115. T. Yamamoto, "Computer simulation study of the conformational statistics of long chain hydrocarbons in cylindrical potentials," *J. Chem. Phys.* **93** (8), 5990 (1990).

116. K. Fukao, "Disorder in paraffin chains of urea adducts and *n*-paraffins," *J. Chem. Phys.* **92** (11), 6867 (1990).

117. G. J. Moro, "The coupling between librational motions and conformational transitions in chain molecules. A phenomenological analysis," *J. Chem. Phys.* **94** (12), 8577 (1991).

118. R. Roy, B. G. Sumpter, D. W. Noid, and B. Wunderlich, "Estimation of dispersion relations from short-duration molecular dynamics simulations," *J. Phys. Chem.* **94**, 5720 (1990).

119. G. A. Pfeffer, B. G. Sumpter, and D. W. Noid, "Conformational changes in a polyethylene model under tension and compression," *Polym. Engr. Sci.*, **32**, 1278 (1992).

120. D. W. Noid, B. G. Sumpter, G. L. Liang, and B. Wunderlich, "Molecular dynamics simulation of electric field induced motion in crystalline polyethylene," *Proceeding of the SPE 50th Annual Techical Confference & Exhibts*, 1992, p 1982.

121. B. Wunderlich, A. Xenopoulous, D. W. Noid, and B. G. Sumpter, "Defect generation and motion in polyethylene-like crystals analyzed by simulation with supercomputers," *Mat. Res. Soc. Proc.*, **209**, 147 (1991).

122. C. Moser, "New computers for molecular dynamics" in "Molecular-Dynamics Simlation of Statistical-Mechanical Systems," (G. Ciccotti and W. G. Hoover Ed.), North-Holland, Amsterdam, p. 600, 1986.

123. K. Singer, J. V. L. Singer and A. J. Taylor, "Molecular dynamics of liquids modeled by '2-Lennard-Jones centres' pair potentials II. Translational and rotational autocorrelation functions," *Mol. Phys.* **37**, 1239 (1979).

124. J. B. Marion, "Classical Dynamics of Particles and Systems", Academic Press, New York, 1965.

125. A. D. Buckingham, P. W. Fowler, and J. M. Hutson, "Theoretical studies of van der Waals molecules and intermolecular forces," *Chem. Rev.* **88** (6), 963 (1988).

126. M. J. Field, P. A. Bash, and M. Karplus, "A combined quantum mechanics potential for molecular dynamics simulations," *J. Compt. Chem.* **11** (6), 700 (1990).

127. S. K. Knudson, D. W. Noid, and B. G. Sumpter, "Dynamics of charged polymers. 1," *Macromolecules* **25**, 331 (1992).

128. W. G. Hoover, "Computational Statistical Mechanics," Elsevier, Amsterdam, 1991.

129. R. P. Wool, R. S. Bretzlaff, B. Y. Li, C. H. Wang, and R. H. Boyd, "Infrared and Raman spectroscopy of stressed polyethylene," *J. Polym. Sci.* **24B**, 1039 (1986).

130. D. Brown and J. H. R. Clarke, "Molecular dynamics computer simulation of polymer fiber microstructure," *J. Chem. Phys.* **84** (5), 2858 (1986).

131. R. H. Boyd and S. M. Breitling, "The conformational analysis of crankshaft motions in polyethylene," *Macromolecules* 7 (6), 855 (1974); R. A. Sorensen, W. B. Liam, and R. H. Boyd, *Macromolecules* **21**, 194 (1988).

132. E. Neusy, S. Nosé, and M. L. Klein, "Molecular dynamics calculations for solid bicyclo (2,2,2) octane." *Mol. Phys.* **52**, 269 (1984).

133. J. Barnes and B. Fanconi, "Critical review of vibrational data and force field constants for polyethylene," *J. Phys. Chem. Ref. Data*, 7 (4), 1309 (1978).

134. C. W. Gear, "The numerical integration of ordinary differential equations of various order," Report ANL 7126, Argone National Laboratory (1966).

135. C. W. Gear, "Nemerical Initial Value Problems in Ordinary Differential Equations," Prentice-Hall, Englewood Cliffs, N.J., 1971.

136. L. Verlet, "Computer 'experiments' on classical fluids. I. Thermodynamical properties of Lennard-Jones molecules," *Phys. Rev.* **159**, 98 (1967).

137. R. W. Brankin, I. Gladwell, J. R. Dormand, P. J. Prince, and W. L. Seward, "Algorithm 670 – A Range-Kutta-Nystrom code," *ACM Transactions on Mathematical Software* **15** (1), 31 (1989).

138. H. J. C. Berendsen and W. F. van Gunsteren, "Pratical algorithms for dynamic simulations," in "Molecular Dynamics Simulation of Statistical Mechanical Systems," (G. Ciccotti and W. G. Hood Eds.), North Holland Physics Publishing, Amsterdam, New York, 1985, pp. 43-65.

139. L.F. Shampine and M. K. Gordon, "Computer Solution of Ordinary Differential Equations: The Initial Value Problem," Freeman, San Franciso, 1975.

140. D. A. McQuarrie, "Statistical Mechanics," Harper & Row Publishers, New York, 1976.

141. P. S. Y. Cheung, "On the calculation of specific heats, thermal pressure coefficients and compressibilities in molecular dynamics simulations," *Mol. Phys.* **33**, 519 (1977).

142. G. H. Stout an L. H. Jensen, "X-ray Structure Determination: A Practical Guide," TheMacmillan Company, New York, 1968.

143. D. E. Sander, "Introduction to Crystallography," W. A. Benjamin, Inc., New York, 1969.

144. M. F. C. Ladd, "Symmetry in Molecules and Crystals," Ellis Horwood Limited, New York, 1989.

145. G. C. Lie, E. Clementi, and M. Yoshimine, "Study of the structure of molecular complexs. XIII. Monte Carlo simulation of liquid water with a configuration interaction pair potential," *J. Chem. Phys.* **64**, 2314 (1976).

146. A. Einstein, "Die Plancksche Theorie der Strahlung und die Theorie der Spezifischen Wärme," *Ann. Physik*, **22**, 180 (1907).

147. P. Debye, "Zur Theorie der Spezifischen Wärmen," *Ann. Physik*, **39**, 789 (1912).

148. (a) A. I. Kitaigorodskii, "Organicheskaya Kristallokhimiya," Acad. Sci. USSR, Moscow, 1955 ("Chemical Organic Crystallography," English Translation, Consultants Bureau: New York, 1961); (b) A. I. Kitaigorodskii, "Molecular Crystals and Molecules," Academic Press, New York, 1973.

149. J. Brandrup, and E. H. Immergut, "Polymer Handbook," J. Willey, New York, 1989.

150. B. Wunderlich, "Molecular nucleation segregation," *Faraday Dis.*, **68**, 239 (1979).

151. E. Hellmuth and B. Wunderlich, "Superheating of linear high-polymer polyethylene crystals," *J. Appl. Phys.* **36**, 3039 (1965); E. Hellmuth, B. Wunderlich, and J. M. Rankin,"Superheating of linear high polymers. Polytetrafluorethylene," *Appl. Polym. Symp.* **2**, 101 (1966); M. Jaffe and B. Wunderlich, "Superheating of extended-chain polymer crystals," in "Thermal Analysis," E. F. Schwender and P. D. Garn Eds, Vol. 1, pg 387, Academic Press, New York, 1969; B. Wunderlich and P. H.-C. Shu, "The crystallization and melting of selenium," *J. Cryst. Growth* **48**, 227 (1980); A. J. Kovacs, A. Gonthier, and C. Straupe,"Isothermal growth, thickening, and melting of poly(ethylene oxide) single crystals in the bulk," *J. Polym. Sci., Polym. Symp.* **50**, 283 (1975); A. J. Kovacs, C. Straupe, and A. Gonthier, "Isothermal growth, thickening, and melting of poly(ethylene oxide) single crystals in the bulk. II," *ibid*, **59**, 31 (1977).

152. B. G. Sumpter, D. W. Noid, and B. Wunderlich, "Infrared laser induced ablation and melting in model polymer crystals," in "Laser Ablation Mechanisms and Applications," J. C. Miller and R. F. Haglund edts., Pgs. 334-342. "Lecture Notes in Physics," Proceedings of the Workshop and Laser Ablation Mechanisms and Applications. Speinger Verlag, New York, NY, 1991.

153. N. G. Mccrum, B. E. Read, and G. Williams, "Anelastic and Dielectric Effects in Polymeric Solids," Wiley, New York, 1967.

154. R. J. Meakins, "Progress in Dielectrics," Heywood, London, 1961, Vol 3, P. 153.

155. R. J. Meakins, "Relationships of rate process parameters for dielectric absorption in crystalline long-chain compounds," *Trans. Faraday Soc.*, **55**, 1694 (1959); "The magnitude of the dielectric absorption in solid aliphatic long-chain compounds," *ibid*, 1701 (1959).

156. C. R. Ashcraft and R. H. Boyd, "A dielectric study of molecular relaxation in oxidized and clorinated polyethylenes," *J. Polym. Sci. Polym. Phys. Ed.*, **14**, 2153 (1976).

157. H. Fröhlich, "Dielectric loss in paraffin-wax solutions," *Proc. Phys. Soc. Lond.*, **54**, 422 (1942).

158. H. Fröhlich, "Theory of Dielectrics," 2nd Ed., Oxford U. P., Oxford, 1958.

159. R. H. Boyd and J. A. Sayre, "Dielectric evidence for thermal creation of defects in polyethylene crystals," *J. Polym. Sci.: Polym. Phys. Eds.*, **17**, 1627 (1979).

160. J.-P. Ryckaert and M. L. Klein, "Translational and rotational disorder in solid n-alkanes: Constant temperature-constant pressure molecular dynamics calculations using infinitely long flexible chains," *J. Chem. Phys.*, **85** (3), 1613 (1986).

161. J.-P. Ryckaert, M. L. Klein, and I. R. McDonald, "Disorder at the bilayer interface in the pseudohexagonal rotator phase of solid n-alkanes," *Phys. Rev. Lett.*, **58** (7), 698 (1987).

162. (a). D. E. Williams, "Nonbonded potential parameters derived from crystalline hydrocarbons," *J. Chem. Phys.*, **47**, 4680 (1967); (b). D. E. Williams and S. R. Cox, "Nonbonded potentials for azahydrocarbons: the importance of the coulombic interaction," *Acta Cryst.*, **B40**, 404 (1984).

163. (a) P. Bergé, Y. Pomeau, and C. Vidal, "Order within Chaos. Towards a Deterministic Approach to Turbulence," Hermann, Paris, 1984; (b) J. M. T. Thompson and H. B. Stewart, "Nonlinear Dynamics and Chaos," John Wiley and Sons, Chichester, 1986.

164. D. W. Noid, M. L. Koszykowski, and R. A. Marcus, "Quasiperiodic and stochastic behavior in molecules," *Ann. Rev. Phys. Chem.*, **32**, 267 (1981).

165. B. Peng, V. Petrov, and K. Showatter, "Controlling chemical chaos," *J. Phys. Chem.*, **95**, 4957 (1991).

166. A. Monge, E. G. D. Cohen, and J. J. Erpenbeck, "Equipartition of energy in a one-dimensional model of diatomic molecules. II. Maximal Lyapunov exponent and phase-space trajectory separation," *Phys. Rev.*, **43**, 2031 (1991).

167. N. Karasawa, S. Dasgupta, and W. A. Goddard III, "Mechanical properties and force field parameters for polyethylene crystal," *J. Phys. Chem.*, **95**, 2260 (1991).

168. S. Nosé, "A molecular dynamics method for simulations in the canonical ensemble," *Mol. Phys.* **52**, 255 (1984).

# APPENDICES

# APPENDIX A

# FIGURES

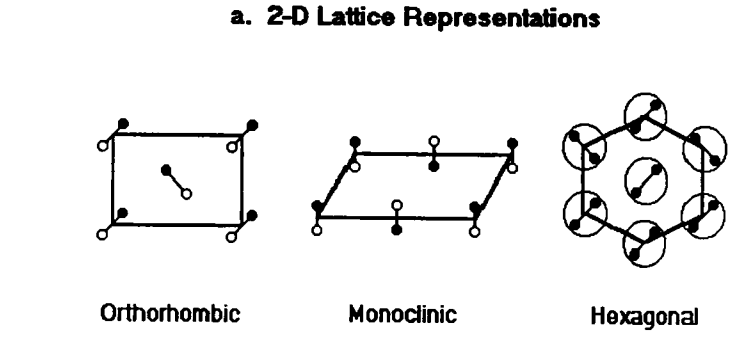


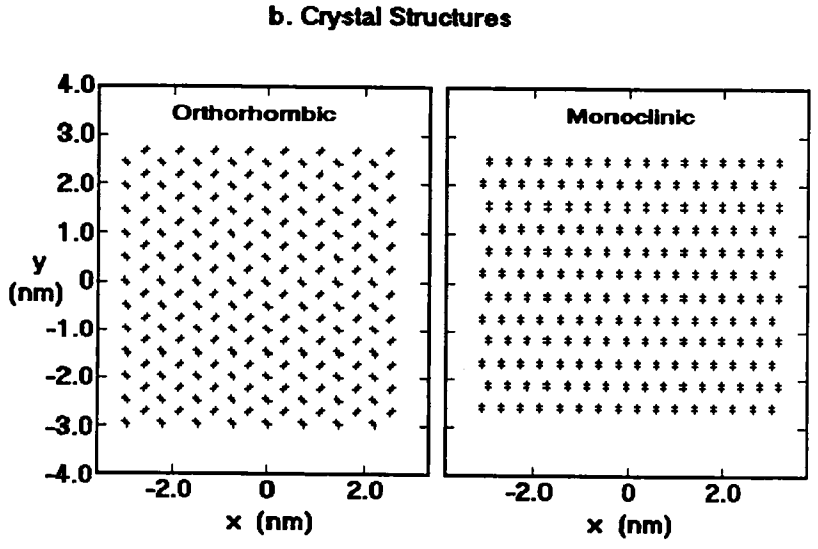


**Figure 1** The 2-D lattice representations (a) and the initial crystal structures (b). In (b), each cross represents the carbon position and each chain contains 50 $CH_2$-groups.

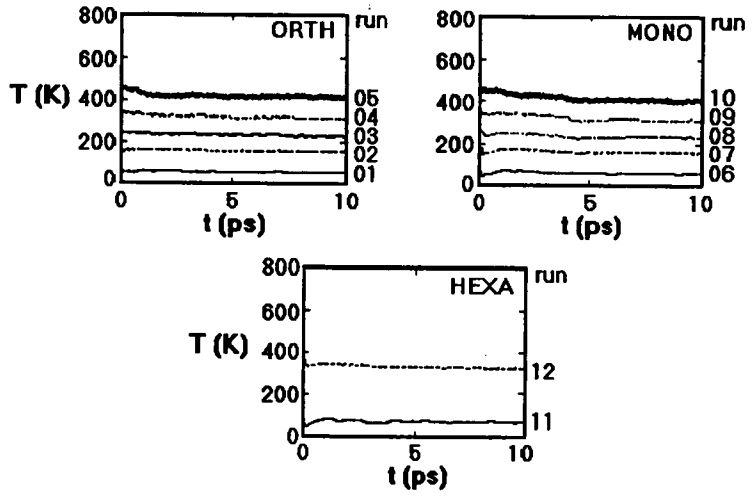


**Figure 2** Fluctuation of temperature as functions of time and initial crystal structure.

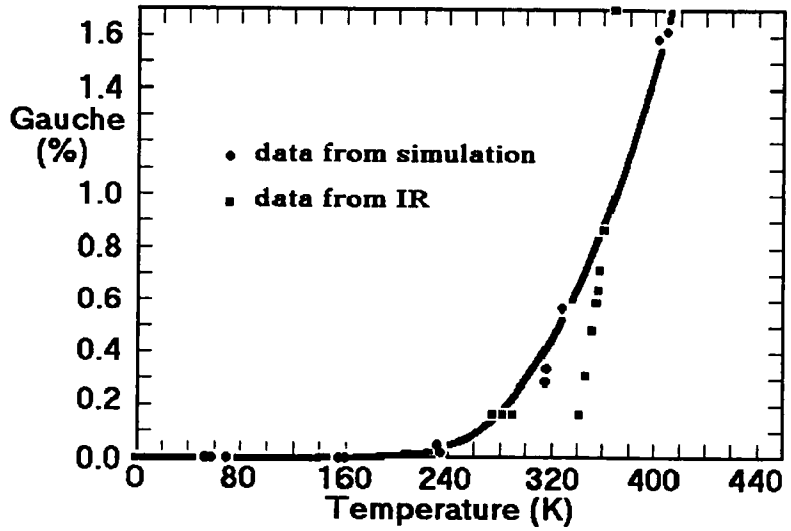


**Figure 3** Concentration of *gauche* bonds as a function of temperature. The simulations are given by circles and the IR measurement by the squares (from ref. 35).

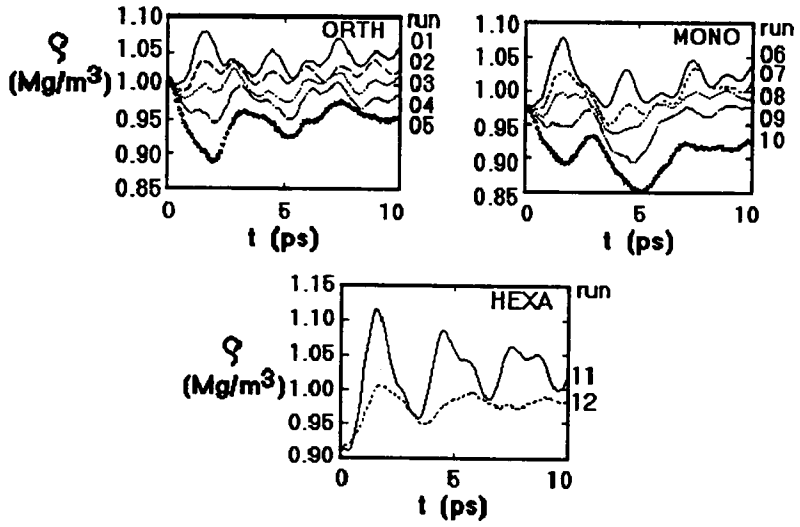


**Figure 4** Fluctuation of density as functions of time and initial structure.

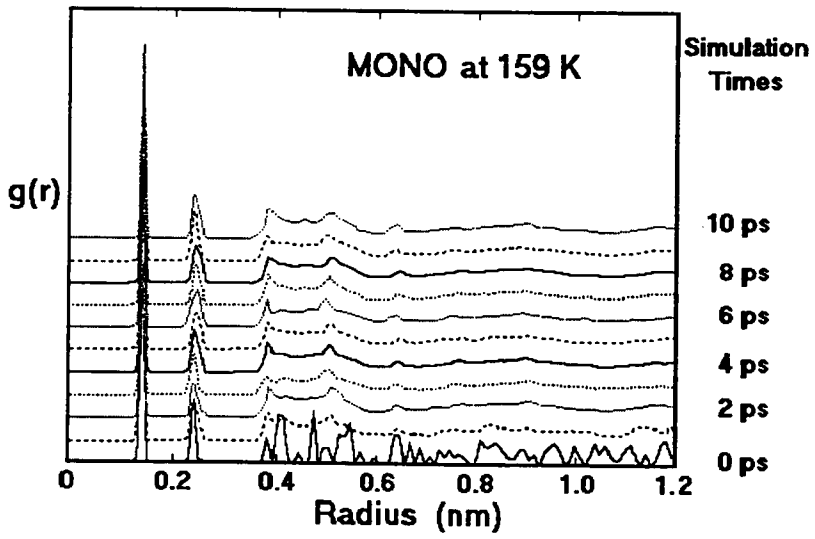


**Figure 5** Radial distribution function of the MONO crystal versus time.

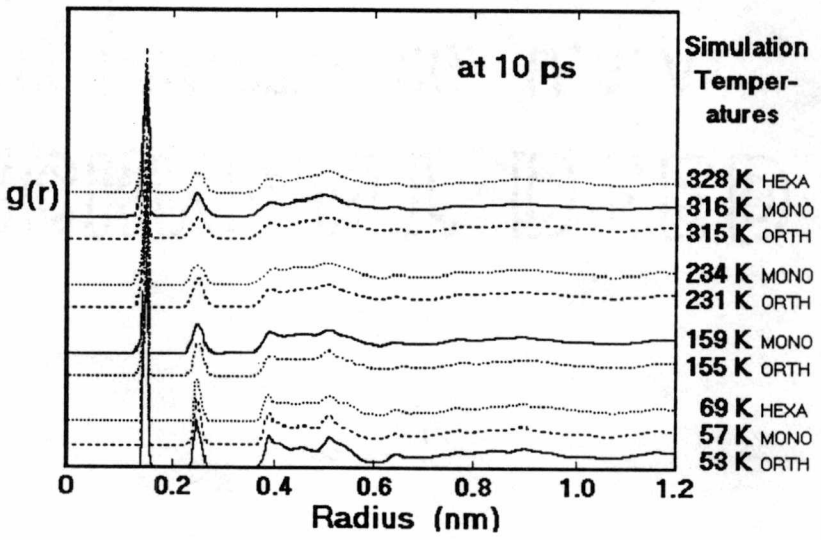


**Figure 6** Radial distribution functions at different temperatures and initial structures.

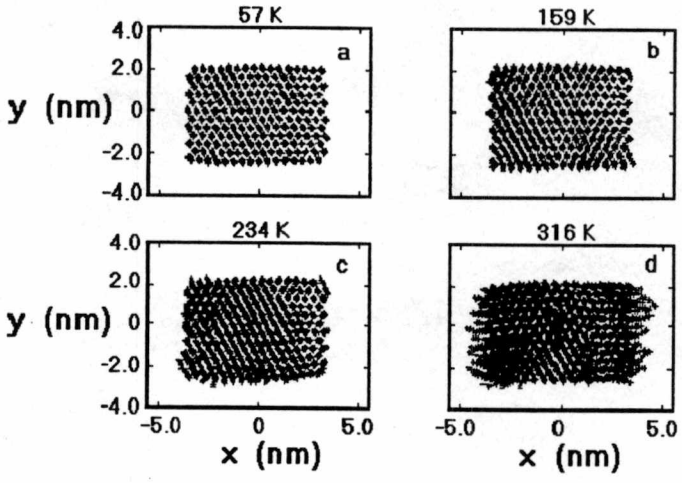


**Figure 7** Structures of the MONO crystal in the *x*-*y* projection at different temperatures after 10 ps of simulation.

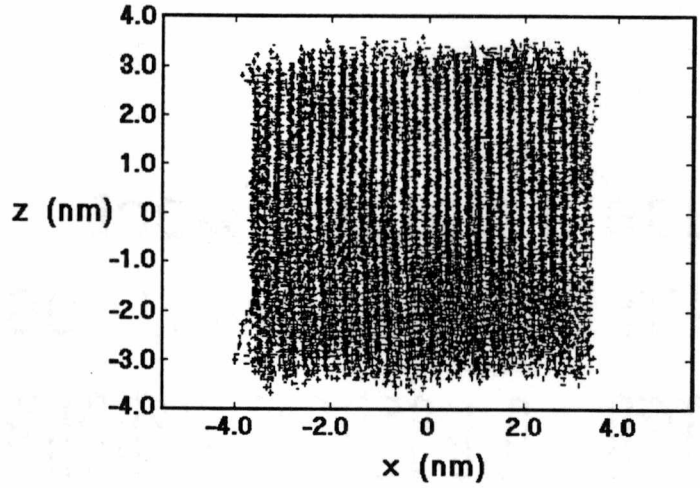


**Figure 8** Structure of the MONO crystal in the *x*-*z* projection at 10 ps and 234 K.

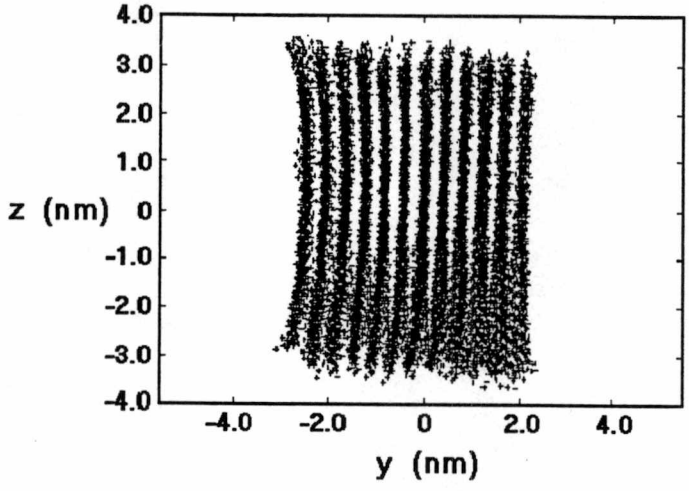


**Figure 9** Structure of the MONO crystal in the *y*-*z* projection at 10 ps and 234 K.

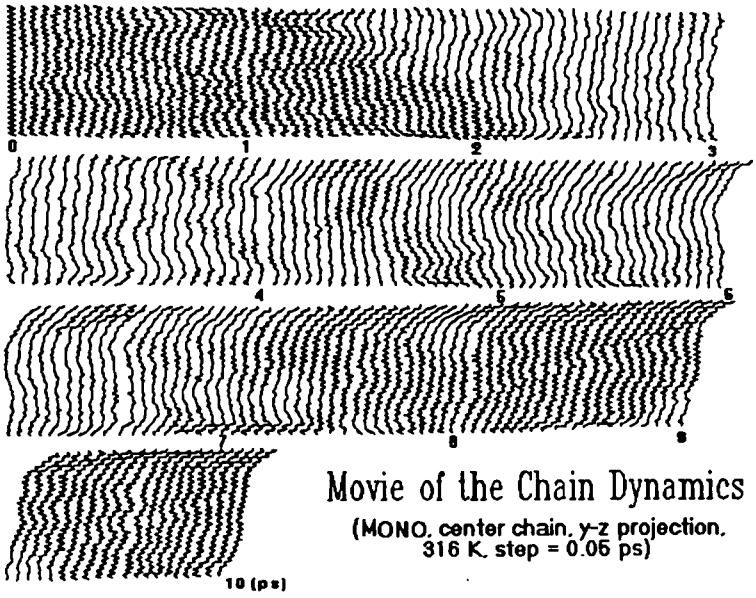


**Figure 10** The time evolution of the dynamics of the center chain in the MONO crystal at T = 316 K from 0 to 10 ps.

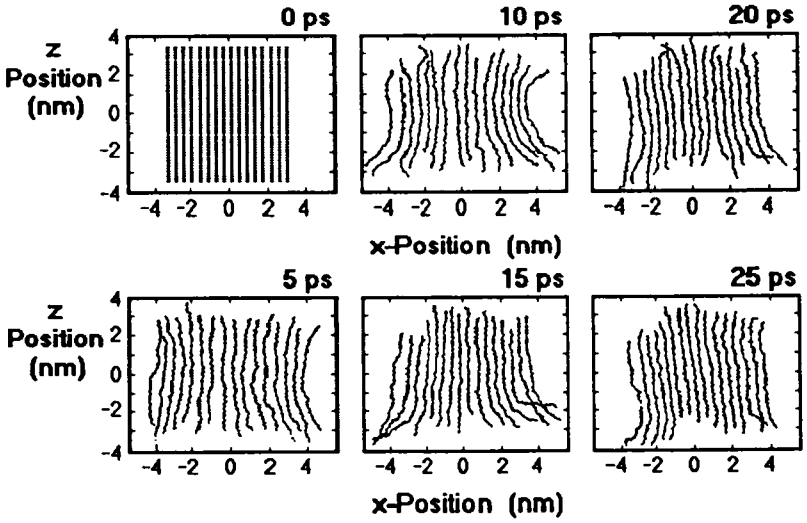


**Figure 11** The dynamics and coupling of chain motion in a surface layer of the MONO crystal at 403 K.

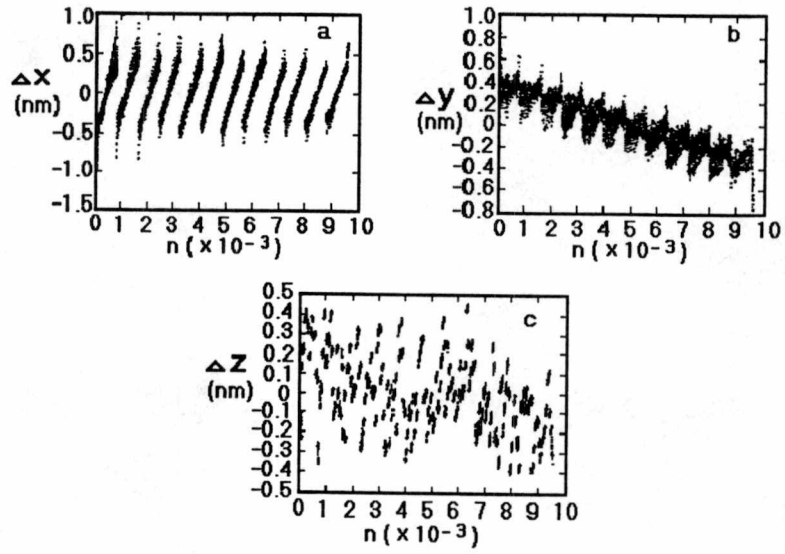


**Figure 12** The positional difference of each atom in a MONO crystal taken from time averaged coordinates (between 5 and 10 ps) at 234 K and initial coordinates. The abscissa represents the number of the atom, and the ordinate represents the difference in $x$ (a), $y$ (b), and $z$ (c) dimension.

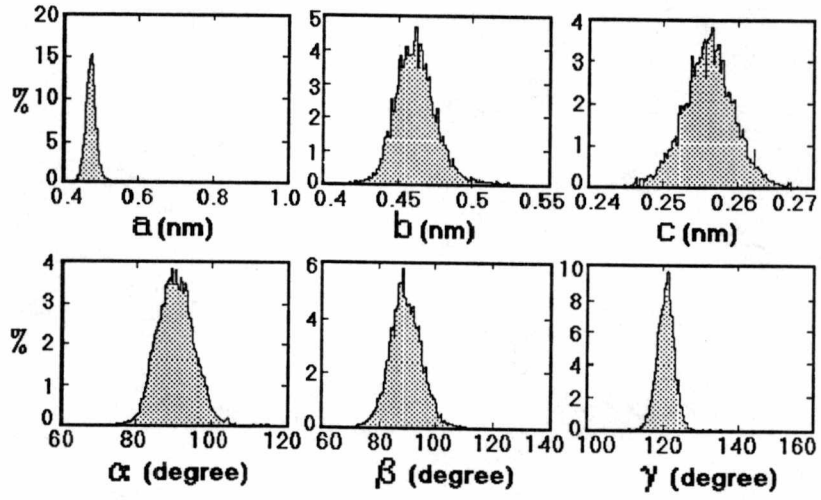


**Figure 13** Histogram of lattice parameters of the MONO crystal at 234 K (steady-state average between 5 and 10 ps).

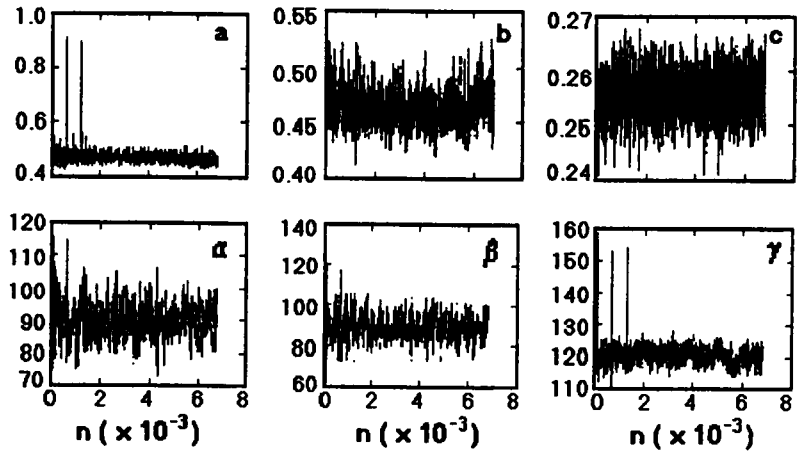


**Figure 14** Lattice parameters as functions of lattice position $n$ under the same condition as Figs. 12 and 13.

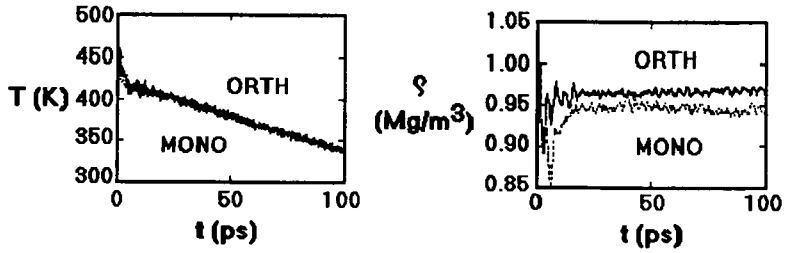


**Figure 15** Temperature and density as a function of time in the unconstrained crystals. Solid line: ORTH (Run D05 in Table 7), dotted line: MONO (Run D10 in Table 7).

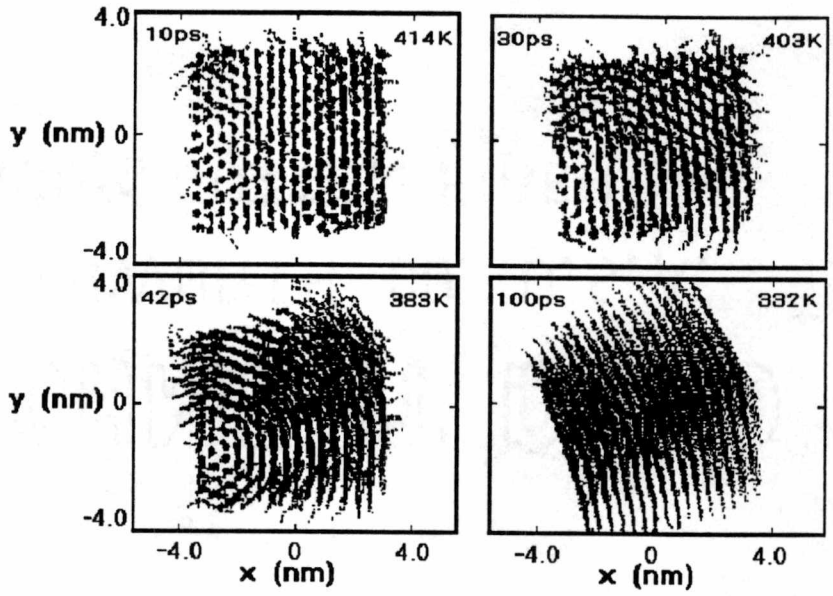


**Figure 16** The *x-y* projection of the unconstrained ORTH as functions of time and temperature (Run D05 in Table 7).

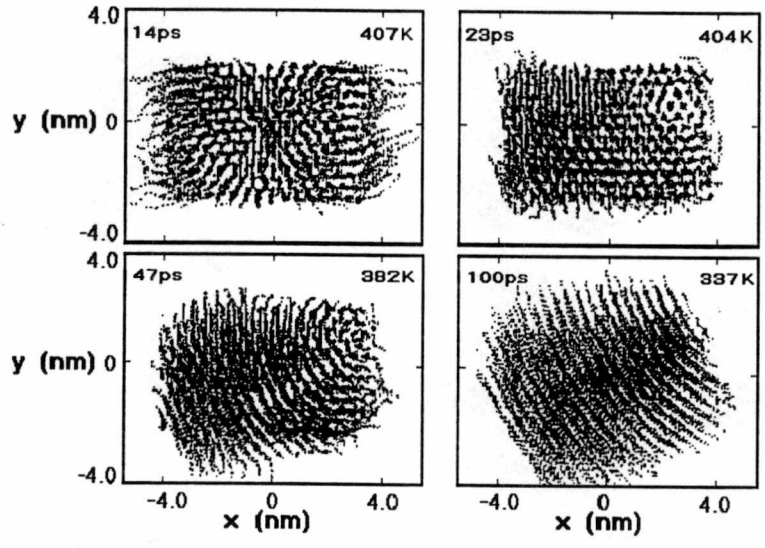


**Figure 17** The *x-y* projection of the unconstrained MONO as functions of time and temperature (Run D10 in Table 7).

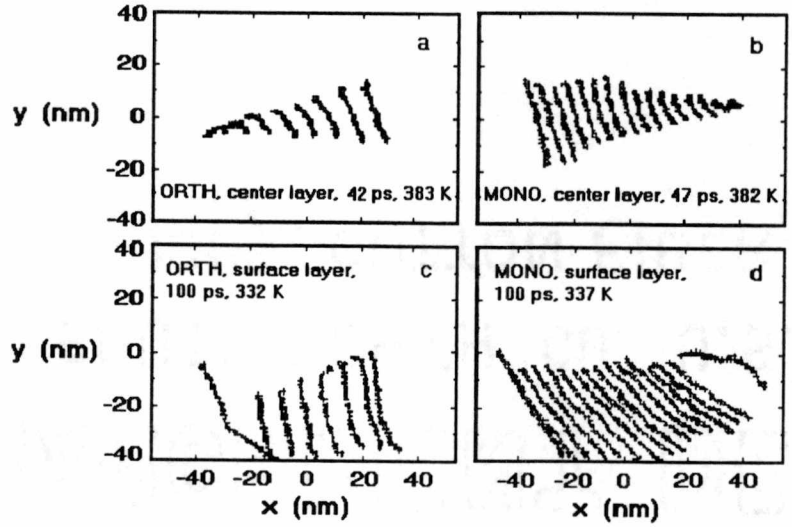


**Figure 18** The orientation of molecules in a single layer in the *x*-*y* projections (ORTH: Run D05 in Table 7; MONO: Run D10 in Table 7).

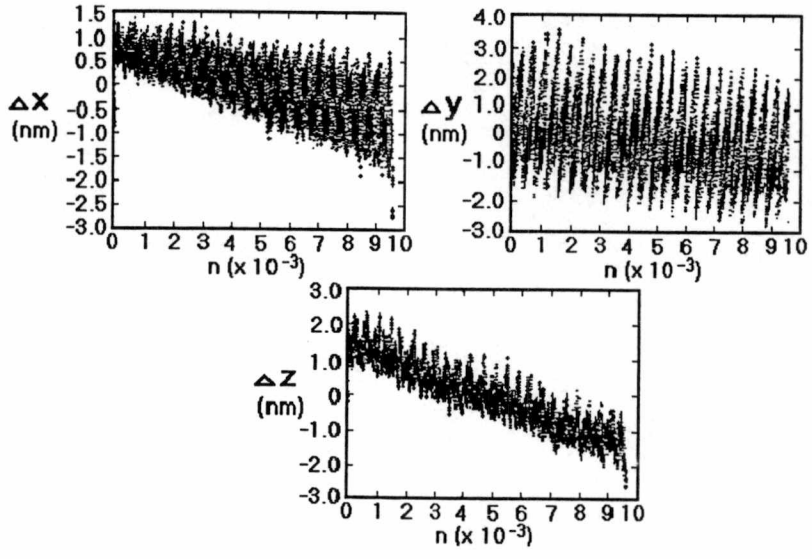


**Figure 19** Shift of the 9600 $CH_2$-units in the unconstrained ORTH crystal after 100 ps simulation at 332 K (Run D05 in Table 7). (Note that after 400 steps one layer is completed).

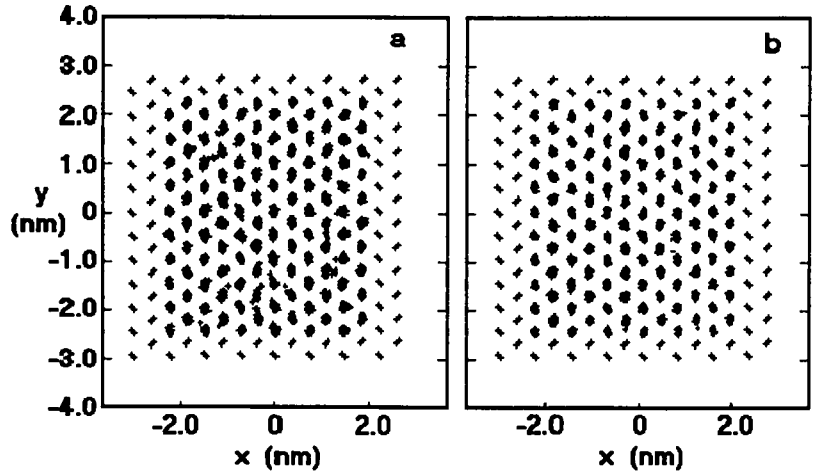


**Figure 20** The *x*-*y* projections of 4-SC ORTH crystal (Run S14, 340–227 K in Table 7), (a) after 10 and (b) after 66 ps of simulations.

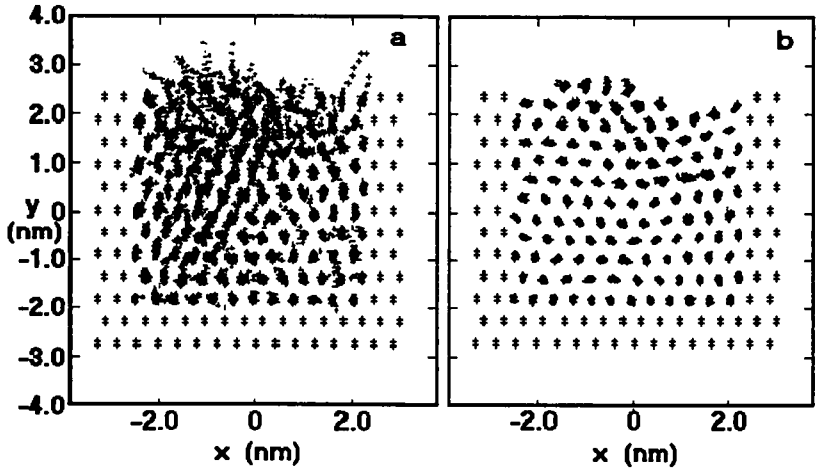


**Figure 21** The *x*-*y* projections of 3-SC MONO crystal (Run S11, 442–255 K in Table 7), (a) after 5 and (b) after 100 ps of simulations.

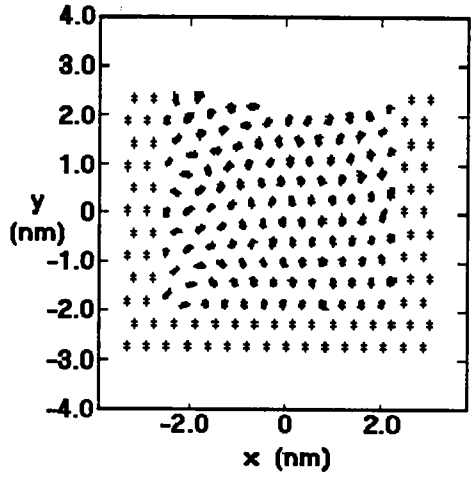


**Figure 22** The *x*-*y* projection of 3-SC MONO crystal (Run S12 in Table 7) after 100 ps of simulation (144 K).

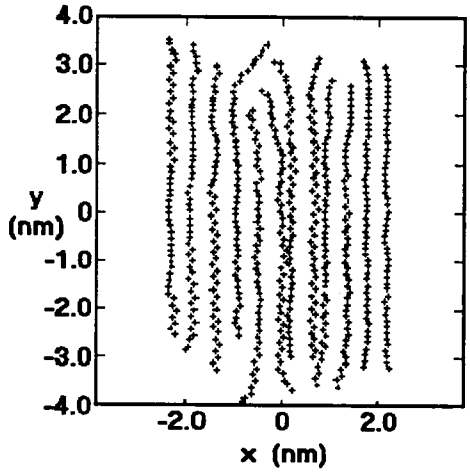


**Figure 23** The *x*-*z* projection of the dynamic chains in the eighth layer of 4-SC MONO crystal (Run S10 in Table 7) after 10 ps of simulation.

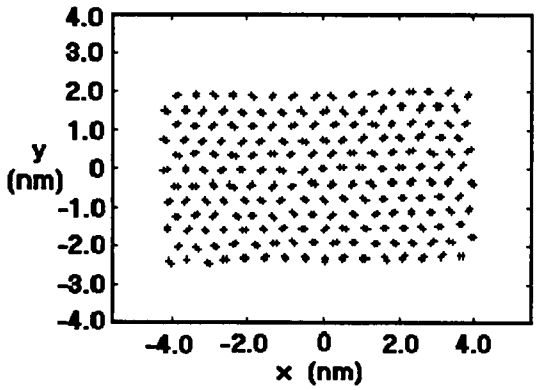


**Figure 24** Average setting angle in the MONO crystal at 316 K (Run 9 in Table 3) after 5 ps of simulation.

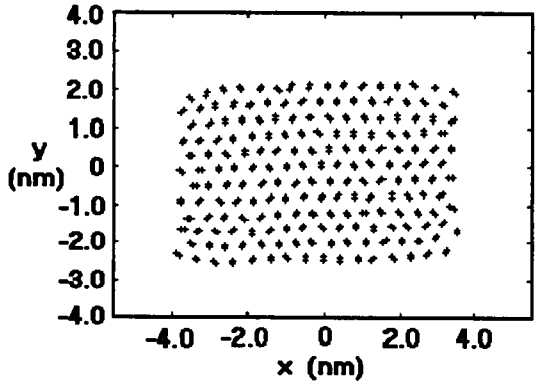


**Figure 25** Average setting angle in the MONO crystal at 316 K (Run 9 in Table 3) after 10 ps of simulation.

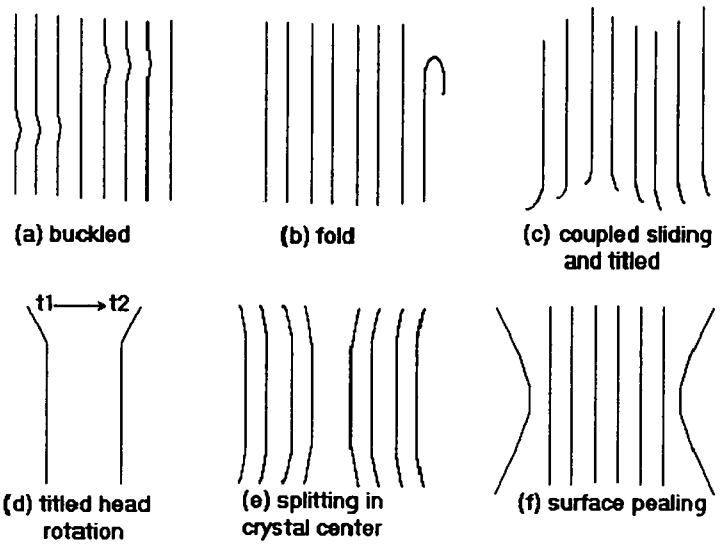


**Figure 26** Schematical illustration for various types of defects found in the simulations.

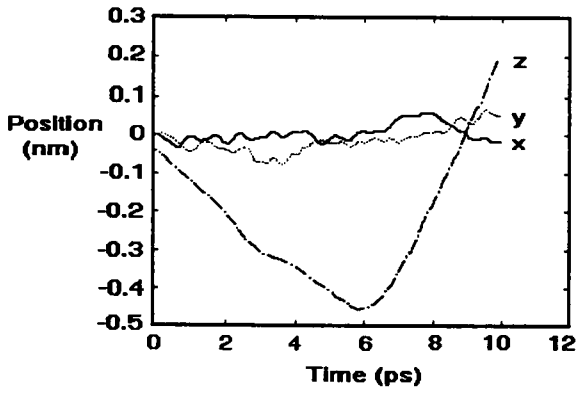


**Figure 27** Center of mass coordinates (solid line: $x$, dotted line: $y$, dash line: $z$) of the center chain in the MONO crystal at 316 K (Run 9 in Table 3) as a function of time.

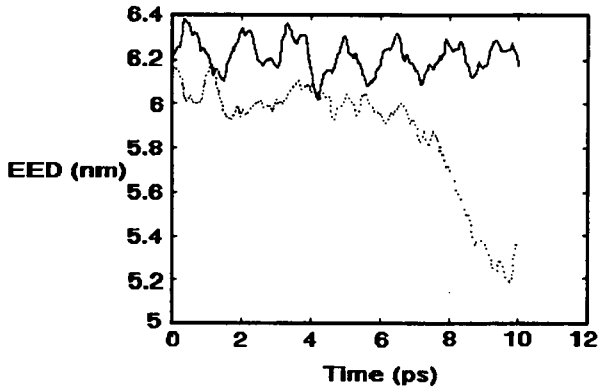


**Figure 28** End-to-end distance of the center chain (solid line) and the edge chain (dotted line) in the MONO crystal at 316 K (Run 9 in Table 3) as a function of time.

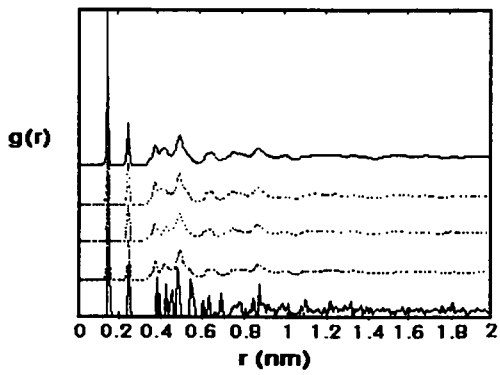


**Figure 29** Radial distribution function versus time (from the bottom to the top: 0, 2, 3, 4, and 5 ps) in the simulation XR01 (Table 10).

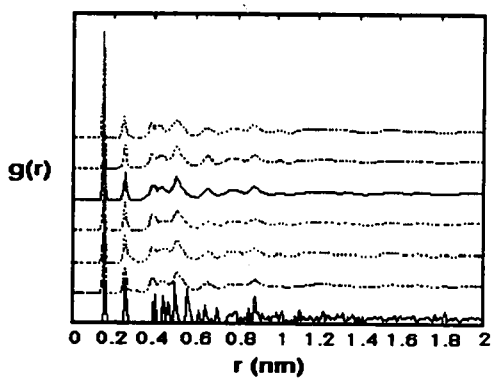


**Figure 30** Radial distribution function versus time (from the bottom to the top: 0, 5, 6, 7, 8, 9, and 10 ps) in the simulation XR02 (Table 10).

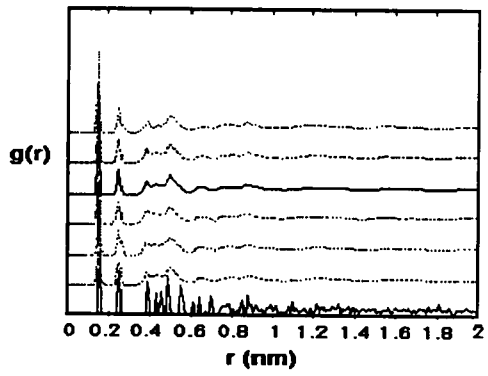


**Figure 31** Radial distribution function versus time (from the bottom to the top: 0, 2, 3, 4, 5, 6, and 7 ps) in the simulation XR04 (Table 10).

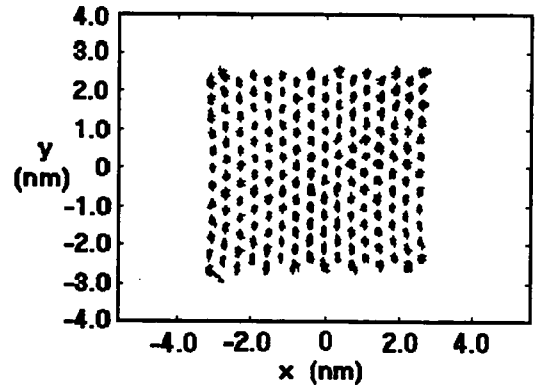


**Figure 32** The *x*-*y* projection of the crystal at 112 K after 5 ps of simulation in the run XR01 (Table 10).

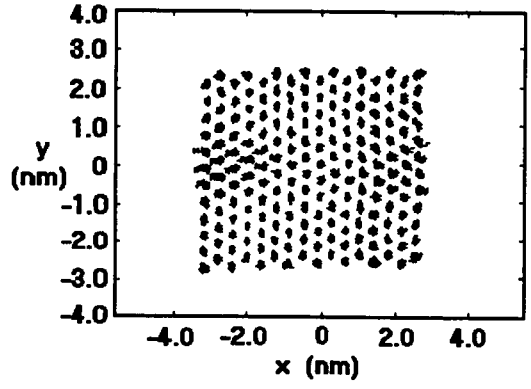


**Figure 33** The *x*-*y* projection of the crystal at 247 K after 6 ps of simulation in the run XR02 (Table 10).

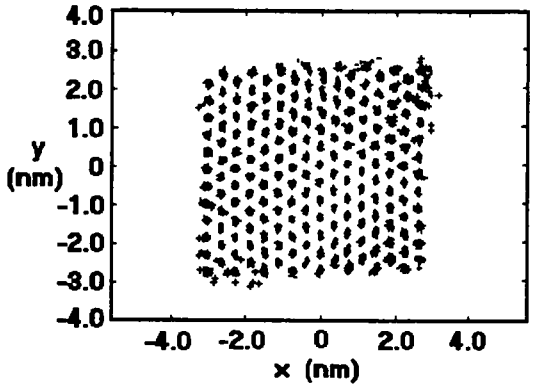


**Figure 34** The *x*-*y* projection of the crystal at 309 K after 7 ps of simulation in the run XR04 (Table 10).

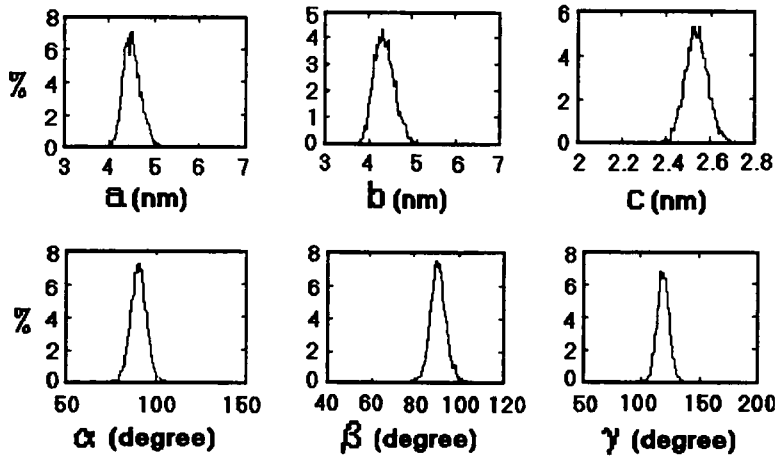


**Figure 35** Lattice parameter distribution in the ORTH crystal at 309 K after 7 ps of simulation in the run XR04 (Table 10).

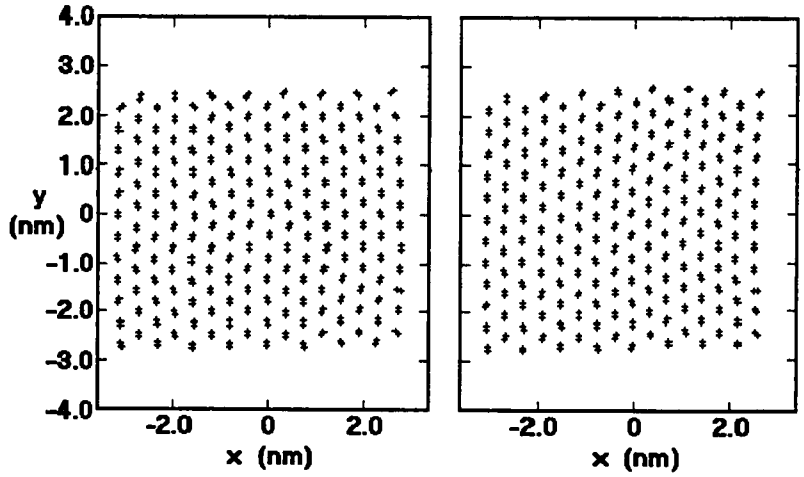


**Figure 36** Average setting angle in the crystal at about 310 K (Run XR04 in Table 10) after 2 (a) and 7 (b) ps of simulations.

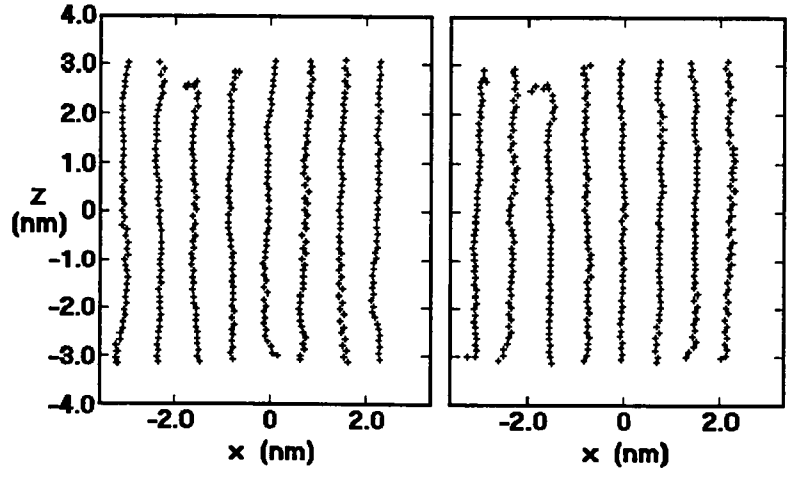


**Figure 37** The *x*-*z* projection of the surface layer in the crystal at about 310 K (Run XR04 in Table 10) as a function of time (left: after 2 ps, right: after 7 ps).

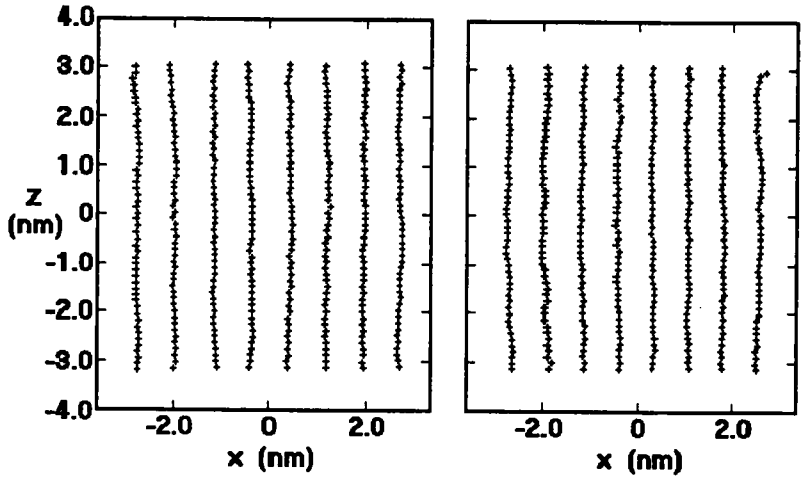


**Figure 38.** The $x$-$z$ projection of the center layer in the crystal at about 310 K (Run XR04 in Table 10) as a function of time (left: after 2 ps, right: after 7 ps).

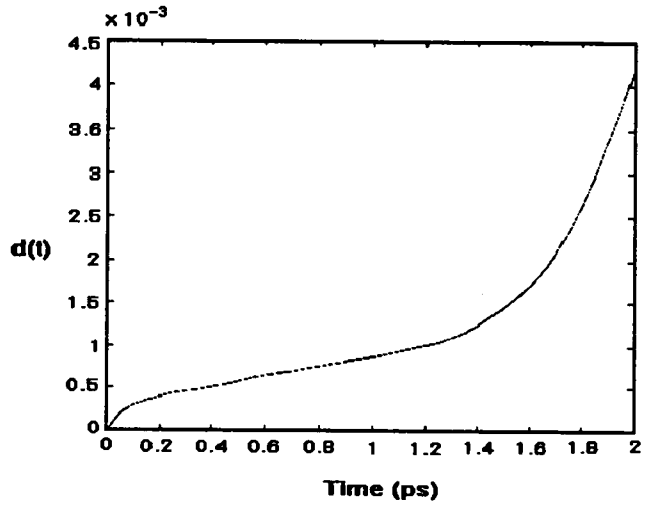


**Figure 39** Trajectory separation as a function of time.

# APPENDIX B

# SUMMARY OF EXPERIMENTAL GAUCHE BOND DETERMINATION

## Raman and IR Measurements

In 1981 Zerbi *et al.*[1] measured the concentration of *gauche* defects in solid *n*-nonadecane ($C_{19}H_{40}$) via IR and Raman spectroscopy on both nondeuterated and selectively deuterated samples. The measurements were based on the shifts in the vibrational spectrum caused by the type of geometrical defects introduced.[1] The conformational defects were analyzed by comparing the observed spectra with predictions based on normal mode calculations using a force field derived by Snyder.[2]

In the nondeuterated sample at low temperature with all *trans* packing, a strong LAM1 mode at 124.5 $cm^{-1}$ was observed. Besides other observations, at temperatures between the solid-solid phase transition (295.95 K) and melting (305.15 K) the Raman peak of LAM1 has a frequency shift from 124.5 to 123.2 $cm^{-1}$ and in the melt the LAM1 mode disappears completely and is replaced by the so-called "pseudo-LAM" which is broad and week near 220 $cm^{-1}$, common to all liquid *n*-alkanes and polyethylene. It was suggested that the downward shift of the LAM peak indicates the weakening of the interlamellar forces due to the increase in the lamellar distance at the phase transition.[1] This increase of interlamellar distance was further interpreted as the results of the sliding of chains in the chain direction and the formation of end *gauche* conformation (the penultimate bond is *gauche* and adjacent to consecutive *trans* bonds).

A quantitative estimation of the concentration of *gauche* defects was obtained by plotting the intensity ratio of the LAM1 band to the Raman line at 1300 $cm^{-1}$ ($CH_2$ twist mode) as a function of temperature and the total population of chains with twisted head (end-*gauche*) in the "rotator phase"[1] was estimated to be of the order 10–15%, which means that the *gauche*-bond concentration is of the order of 0.63–0.94%. The *gauche*-bond concentration is defined as the number of *gauche* bonds per 100 bonds able to rotate about.

To probe the defect position in the crystal, Zerbi and coworkers analyzed the infrared spectra of the sample selectively deuterated at the positions of the second and the tenth carbon atoms.[1] Based on the normal-mode calculation, the CHD and $CD_2$ rocking modes show strong dependence on the conformation of neighboring bonds. The calculations showed that in all-*trans* samples the $CD_2$ rocking mode occurs at 615 $cm^{-1}$. This frequency shifts if *gauche* bonds are introduced depending on the position and the type of defect (*gauche*, *kink*, or double-*gauche*).[1] No peaks were observed corresponding to the calculated peaks for *kink*, double-*gauche*, and interior *gauche* conformations. All *gauche* peaks were observed to be in the bonds between the 2-3 carbons. By plotting the integrated intensity of the $CD_2$ rocking modes as a function of the temperature, the observed drop of the intensity of about 15% was accounted for by the *gauche* conformation at bonds between carbons 2-3 which yielded the same amount of *gauche* concentration as was estimated for the nondeuterated sample.[1]

Zerbi and coworkers believe that their results agree with the Raman work by Barnes and Fanconi[3] and do not support the "kink" model proposed by Pechhold.[4] The later

measurements on fatty acid by Zerbi *et al.* in 1987 showed that the hydrocarbon chain does not undergo significant conformational disordering until the temperature of the sample is within 2 K of the melting point.[5]

Reports on the vibrational spectroscopic determination of conformational defect in *n*-nonadecane and other odd *n*-alkane solids were also made by Snyder *et al.* in 1981 and 1982.[6,7] It has been known that the solid-solid phase transitions, or premelting, occur for all odd *n*-alkanes between $C_9$ and $C_{45}$.[6] The longer *n*-alkanes, $C_{25}$–$C_{45}$, have more than two solid-solid phase transitions.[6,7] The DSC and IR study by Snyder and coworkers showed that there are discontinuous changes in the IR spectra that occur exactly at the DSC transition temperatures. However, there is no quantitative results of dependence of conformational defects on temperature. Contrary to the work by Zerbi *et al.*[1], *gauche* conformations were found to exist in the interior of the crystal, and *kinks* and double *gauche* conformations were also detected. The results were proposed to support the *kink*-block model.[7] A more quantitative result on the conformational defect concentration during premelting were calculated and summarized below.[7]

Infrared bands were assigned through normal mode calculation for *gt* (1341 $cm^{-1}$), *gtg'* (1306 $cm^{-1}$) and *gg* (1353 $cm^{-1}$). The intensity measurements at these frequencies were reported to have error of ±20%. The concentration of various conformational defects were calculated based on the ratio, *r*, of the measured intensities of solid to liquid, assuming the measured intensities to be unaffected by the state of the sample. The number of defects (*gt*, *gtg'*, or *gg*) in the liquid state were calculated based on the rotational isomeric state model using a *gauche-trans* energy difference of 2.092 kJ/mol

(seems to be too low). For $C_{27}$ in the liquid the calculated averaged number of defects per molecule, $n_{liquid}$, containing *gt*, *gtg'*, and *gg* are 0.624, 2.55, 2.34, respectively, which correspond to a total *gauche* concentration of 43.35% (there are total of 24 torsional bonds in each molecule of $C_{27}$). The average number of each type of conformational defects in one molecules in the solid, $n_{solid}$, was given by multiplication of intensity ratio *r* by $n_{liquid}$ of the same kind of defects in the liquid state. Since it was estimated that the percentage of molecules containing conformational defects for $C_{17}$ and $C_{29}$ is 10% and 70% respectively, one can convert the data presented in ref. 7 to the total *gauche* bond concentration in the "rotator phases" at temperature of 1 K below $T_m$:

| *n*-alkanes | $C_{17}$ | $C_{19}$ | $C_{21}$ | $C_{23}$ | $C_{25}$ | $C_{27}$ | $C_{29}$ |
|---|---|---|---|---|---|---|---|
| $T_m$ – 1 K | 294.1 | 304.2 | 313.3 | 319.7 | 325.7 | 331.0 | 335.6 |
| molecule % | 10 | 20 | 30 | 40 | 50 | 60 | 70 |
| *gauche* % | 0.15 | 0.56 | 1.13 | 1.88 | 2.55 | 3.37 | 4.27 |

where molecule-% is the percentage of molecules estimated to have conformational defects. Based on this estimation, the *gauche* concentration in the "rotator phases" increases as the chain length increases.

Longer-chain alkanes were reported to have more *kink* defects than shorter ones. For $C_{27}$ and $C_{29}$ it was estimated that among all the defects, 20–30% of defects are end-*gauche* defects and 60–70% are *kink* defects, while the double *gauche* defects are ≤0.2%.[7]

The distribution of *gauche* bonds along the chain of $C_{21}$ and $C_{29}$ was further reported by Snyder *et al.*[9,10] These experiments were conducted with IR measurement of selectively deuterated samples. For the 2-3 carbon-carbon bond, the band at 658 $cm^{-1}$ is

associated with the *gauche* conformation and 622 $cm^{-1}$ with the *trans* conformation. The peak at 650 $cm^{-1}$ is assigned to the *gauche* conformations for other carbon-carbon bonds. In the quantitative analyses, the ratio of the intensities of the 658 and 622 $cm^{-1}$ bands was taken to be proportional to the ratio of the number of *gauche* to *trans* bonds at 2-3 position, and the ratio of the intensities of the 650 and 622 $cm^{-1}$ bands was taken to be proportional to the ratio of the number of *gauche* to *trans* bonds at other positions.[10] The results showed that there is an exponential increase of conformational defects toward the chain ends and the distribution depends on temperature and chain length. Increasing temperature or chain length increased the tendency of toward-chain-end distribution. However, this technique can not distinguish whether those non-end *gauche* bonds exist in the surface chains or interior chains. These measurements yield no information on the total *gauche* concentration since only one carbon in a chain was deuterated at a time in the sample. When the measurement was carried out for different positions, the total *gauche* concentration might be estimated, as is discussed below.

Maroncelli *et al.* indicated that this study yields a different kind of conformational data from the previous study[7] and that they are not directly comparable because the $CD_2$ technique yield the fraction of *gauche* bonds at a specific site while the previous work measures the overall concentrations of specific kinds of defects.[10] In the $CD_2$ measurements, only the $CD_2$ rocking modes were measured, other $CH_2$ rocking mode intensities were not included in the quantitative calculation, so that the *gauche* fraction can best represent the fraction of molecules that have *gauche* conformations. To convert it to the overall concentration of *gauche* bonds, one must sum up the possibilities of

*gauche* fractions along the chain and divide it by the number of total possible of torsional bonds. In case of $C_{21}$ assuming all bonds at carbons 2, 4, 6, 10, 15, 17, and 18 can have *gauche* bonds at the same time, with the defect molecule population provided by ref. 10 (so-called fraction gauche %),[10] one can calculate the overall *gauche* concentration being 1.57% at 312.15K (1 K below melting) and 0.91% at 305.15 K (1 K after solid-solid transition to the hexagonal phase). For $C_{29}$, by adding up all possibilities of *gauche* bonds at carbons 2, 4, 6, 8, 10, 14, 18, 22, and 26, one can calculate the overall *gauche* concentration being 1.84% at 336.15 K (1 K below melting). According the Maroncelli *et al.*, the overall *gauche* concentrations for $C_{21}$ were estimated to be about 2% (there is no explanation of how this was estimated).[10] Maroncelli *et al.* also pointed out that this measurement may have a higher value than the previous one[7] (actually not), and suggested that the samples used in their $CD_2$ measurement are less pure and there is a band at 661 $cm^{-1}$ which is due to a CHD impurity that is often comparable to that of the 650 $cm^{-1}$.[10]

Recent reports by Kim[11] and Snyder[12] indicate that much of the work reported earlier that involves the quantitative measurement of disorder suffers from the neglect of two factors that have only recently been characterized. One factor is that the effect of temperature on intrinsic infrared intensities can be very large. Another factor is that disorder and infrared intensity are usually not linearly related because conformational disorder is normally measured on a local basis, whereas the intensities of the modes used to measure consist of contributions spread over many units of the chain. By avoiding these factors new infrared measurements on nondeuterated samples of $C_{17}$, $C_{25}$, $C_{36}$, $C_{50}$, and $C_{60}$ have been reported in 1989.[11] The results showed that the disorder becomes

measurable at the temperature of 10–40 K below the melting point. There is no solid-solid phase transition before melting in $C_{50}$ and $C_{60}$ because their *gauche* concentrations increase gradually with temperature. In ref. [11] the *gauche* concentrations were given as the number of *gauche* bonds per chain. By converting the number of *gauche* bonds per chain to overall *gauche* concentration, the maximum *gauche* concentration before melting from the highest measured data point (Measured) presented in the ref. 11 and the *gauche* concentration by extrapolating (Extrapl.) the measured curves to the melting temperature are:

Overall Gauche% (Temp. K)

| | $C_{17}$ | $C_{25}$ | $C_{36}$ | $C_{50}$ | $C_{60}$ |
|---|---|---|---|---|---|
| Measured | 12.9 (295) | 6.1 (326) | 6.7 (348) | 1.7 (365) | 4.9 (372) |
| Extropl. | 12.9 (295.1) | 9.1 (326.7) | 12.1 (349.1) | 6.8 (365.6) | 5.6 (372.6) |

Note that, the *gauche* concentration does not show clear dependence on the chain length and is higher than the previous estimations using nondeuderated technique.[7]

Based on the information in Fig. 6 of ref. [11], the *gauche* concentration and temperature for $C_{50}$ have following relation and was plotted in Fig. 3 in Appendix b:

| Temp (K) | 273 | 278 | 283 | 288 | 343 | 351 | 356 | 358 | 361 | 363 | 365 | 365.2 |
|---|---|---|---|---|---|---|---|---|---|---|---|---|
| *g* / chain | .08 | .08 | .08 | .08 | .08 | .15 | .22 | .28 | .30 | .35 | .40 | .80 |
| *g* % | .17 | .17 | .17 | .17 | .17 | .32 | .47 | .60 | .64 | .74 | .85 | 1.70 |

Some quantitative studies on vibrational spectrum measurements of conformational defects on the high-pressure phase of polyethylene (PE) was reported. In 1980 Tanaka

and Takemura[13] reported a Raman spectroscopic study for the high-pressure phase of PE. Tanaka and Takemura compared the Raman spectra of PE under 5000 kg/cm$^2$ at the temperatures from 298.15 K (orthorhombic phase) to 534.15 K (liquid phase) in the regions of 3000–2800 cm$^{-1}$ and 1500–1000 cm$^{-1}$. From the observed intensity change and irregular shifts of the skeletal vibration band 1067 and 1135 cm$^{-1}$, they suggested that the high-pressure "rotator phase" is a liquid crystal and the molecular chains in it must contain many *gauche* bonds, similarly to the liquid phase. No further quantitative characterization was provided.[13]

**NMR Measurements**

In 1986 Möller *et al.*[14] reported the results of variable temperature magic angle spinning (MAS) $^{13}C$ solid state NMR measurements of conformational defects on $C_{19}$, $C_{36}$, $C_{168}$, and PE. The technique allowed the observation of up to six carbon atoms at the chain ends near the surface of the lamellar crystals. The conformational information on the bonds beyond sixth carbon atoms are not detectable by this technique. It was observed that there were spectrum upfield shifts in the second ($\alpha$), the third ($\beta$), the fourth ($\gamma$), the fifth ($\delta$), and the sixth ($\varepsilon$) carbons. Based on the information provided by IR measurements in which the fraction of *gauche* bonds at the chain ends increases with increasing length of the *n*-alkanes,[7,10] it was proposed that the different upfield shifts give the degree to which the chain segment of a specific carbon is conformationally disordered.[14] A rough estimation to which degree the conformational disorder is liquid-like was derived from the comparison of the "rotator phase" spectrum with the melt

spectrum. In the case of $C_{36}$ at 349 K, the percentages in the specific bonds, the second, third, fourth, and the fifth bonds, which are *gauche* were estimated to be 65%, 44%, 33%, and 13%, respectively. Dividing these numbers by 33 (there are 33 torsional bonds in each molecule) and then summating them, these numbers correspond to the overall concentration of *gauche* bonds of 4.7% from the NMR measurements. Since at high temperature the interior *gauche* bonds become negligible, 4.7% is close to the maximum *gauche* concentration in the "rotator phase".

The conformation of penultimate bonds ($C_2$–$C_3$ bonds) in *n*-alkanes and PE can be determinate based on γ-methyl substituent effect on δ $^{13}C$, so-called γ-*gauche* shielding effects.[15] For *n*-butane, the γ-*gauche* effect is predicted to have chemical shift of –5.2 ppm if 46% of the $C_2$–$C_3$ bonds have *gauche* conformation.[15] For longer chain alkanes ($n \geq 14$) and PE, the characterization of the conformation in the interior bonds becomes difficult. The determination of overall *gauche* concentration is not yet available using solid state $^{13}C$ NMR technique.

In summary, two different results were given by vibrational spectroscopy: (a). no *kinks* were measured and the *gauche* bonds are all end-*gauche* as reported by Zerbi *et al.*; (b). some *kinks* and double-*gauche* bonds were observed and *gauche* concentration increases exponentially toward the chain ends as reported by Snyder *et al.*, however, the estimated total *gauche* concentration does not agree for the different measurements. The following Table summarizes the estimated total *gauche* concentrations for different paraffins from different measurements.

| Paraffins | Gauche Concentration | Temperature (K) | References |
|---|---|---|---|
| $C_{17}H_{36}$ | 0.15% | 294.1 | [7] |
| | 12.9% | 295 | [11] |
| $C_{19}H_{40}$ | 0.63–0.94% | 295.95–305.15 | [1] |
| | 0.56% | 304.2 | [7] |
| $C_{21}H_{44}$ | 1.13% | 313.3 | [7] |
| | 0.91% | 305.2 | [10] |
| | 1.57% | 312.2 | [10] |
| $C_{23}H_{48}$ | 1.88% | 319.7 | [7] |
| $C_{25}H_{52}$ | 2.55% | 325.7 | [7] |
| | 6.1% | 326 | [11] |
| $C_{27}H_{56}$ | 3.37% | 331.0 | [7] |
| $C_{29}H_{60}$ | 4.27% | 335.6 | [7] |
| | 1.84% | 336.2 | [10] |
| $C_{36}H_{74}$ | 6.7% | 348 | [11] |
| | 4.7% | 349 | [14] |
| $C_{50}H_{102}$ | 1.7% | 365.2 | [11] |
| $C_{60}H_{122}$ | 4.9% | 372 | [11] |

## References


1. G. Zerbi, R. Magni, M. Gussoni, K. H. Moritz, A. Bigotto, and S. Sirlikov, *J. Chem. Phys.* **75**, 3175 (1981).

2. R. G. Snyder, *J. Chem. Phys.* **47**, 1316 (1967).

3. J. D. Barnes and B. M. Fanconi, *J. Chem. Phys.* **56**, 5190 (1972).

4. W. Pechhold, *Kolloid Z. Z. Polym.* **228**, 1 (1968).

5. G. Zerbi, G. Conti, G. Minoni, S. Pison, and A. Bigotto, *J. Phys. Chem.* **91**, 2386 (1987).

6. R. G. Snyder, M. Maroncelli, S. P. Qi, and H. L. Strauss, *Science* **214**, 188 (1981).

7. M. Maroncelli, S. P. Qi, H. L. Strauss, and R. G. Snyder, *J. Am. Chem. Soc.* **104**, 6237 (1982).

8. M. G. Broadhurst, *J. Res. Natl. Bur. Stand., Sect. A.* **66**, 241 (1962).

9. R. G. Snyder, M. Maroncelli, and H. L. Strauss, *J. Am. Chem. Soc.* **105**, 133 (1983).

10. M. Maroncelli, H. L. Strauss, and R. G. Snyder, *J. Chem. Phys.* **82**, 2811 (1985).

11. Y. Kim, H. L. Strauss, and R. G. Snyder, *J. Phys. Chem.* **93**, 7520 (1989).

12. R. G. Snyder, *Macromolecules* **23**, 2081 (1990).

13. H. Tanaka and T. Takemura, *Polym. J.* **12**, 355 (1980).

14. M. Möller, H.-J. Cantow, H. Drotloff, D. Emeis, K.-S. Lee, and G. Wegner, *Makromol. Chem.* **187**, 1237 (1986).

15. A. E. Tonelli, "NMR Spectroscopy and Polymer Microstructure: The Conformational Connection," VCH Publishers, Inc., New York, 1989.

## APPENDIX C

## TABLES

**Table 1** Force field parameters for the united-atom simulations.

| *Two-body interactions* | | | *Four-body interactions* | | |
|---|---|---|---|---|---|
| $D$ | = | 334.72 kJ/mol | $a$ | = | 18.41 kJ/mol |
| $r_e$ | = | 0.153 nm | $b$ | = | 26.78 kJ/mol |
| $\alpha$ | = | 19.9 $nm^{-1}$ | | | |
| *Three-body interactions* | | | *Nonbonding interactions* | | |
| $K_\theta$ | = | 130.22 kJ/mol | $\varepsilon$ | = | 0.477 kJ/mol |
| $\theta_0$ | = | 113° | $\sigma$ | = | 0.398 nm |

**Table 2** Computer simulation units and conversion to SI units

| Items | Simulation Units | Conversion to SI units |
|---|---|---|
| Energy | kcal/mol | multiply with 4.18 to get kJ/mol |
| Distance | ångstrom | multiply with 0.1 to get nm |
| Mass | amu | equal to $1.66 \times 10^{-27}$ kg |
| Time | 1/20.45 ps | multiply with $20.45 \times 10^{12}$ to get s |
| Force | mdyne | multiply with $10^{-8}$ to get N |
| Pressure | 1/148.9 GPa | no conversion necessary |
| Gas constant $R$ | $1.98717 \times 10^{-3}$ kcal/(K mol) | SI units: 8.31441 J/(K mol) |

**Table 3** Average density and *gauche* concentration as functions of time and temperature.

| Run Number | Crystal Type | Temperature (K)[a] | Density ($Mg/m^3$)[a] | Gauche %[a] | Run Time (ps) |
|---|---|---|---|---|---|
| 1 | ORTH | 53 | 1.04 | 0.00 | 10 |
| 2 | ORTH | 155 | 1.02 | 0.00 | 10 |
| 3 | ORTH | 231 | 1.00 | 0.05 | 10 |
| 4 | ORTH | 315 | 0.98 | 0.29 | 25 |
| 5 | ORTH | 410 | 0.95 | 1.62 | 10 |
| 6 | MONO | 57 | 1.01 | 0.00 | 10 |
| 7 | MONO | 159 | 1.00 | 0.00 | 10 |
| 8 | MONO | 234 | 0.99 | 0.02 | 10 |
| 9 | MONO | 316 | 0.96 | 0.34 | 25 |
| 10 | MONO | 403 | 0.90 | 1.59 | 10 |
| 11 | HEXA | 69 | 1.03 | 0.00 | 10 |
| 12 | HEXA | 328 | 0.98 | 0.57 | 10 |

[a]Average between 5 to 10 ps.

**Table 4** Standard deviations of the positions of the $CH_2$-groups in nm as a function of temperature.

| Number | Crystal | Temp (K) | Δx | Δy | Δz | Δxyz | Δr |
|---|---|---|---|---|---|---|---|
| 1 | ORTH | 53 | 0.15 | 0.20 | 0.08 | 0.43 | 0.26 |
| 2 | ORTH | 155 | 0.17 | 0.18 | 0.12 | 0.47 | 0.27 |
| 3 | ORTH | 231 | 0.17 | 0.15 | 0.16 | 0.48 | 0.28 |
| 4 | ORTH | 315 | 0.17 | 0.11 | 0.23 | 0.51 | 0.31 |
| 6 | MONO | 57 | 0.20 | 0.25 | 0.12 | 0.57 | 0.34 |
| 7 | MONO | 159 | 0.24 | 0.23 | 0.15 | 0.62 | 0.36 |
| 8 | MONO | 234 | 0.27 | 0.23 | 0.19 | 0.69 | 0.40 |
| 9 | MONO | 316 | 0.42 | 0.24 | 0.24 | 0.91 | 0.54 |

**Table 5** Lattice parameters as functions of initial structure and temperature*

| | *a* (nm) | *b* (nm) | *c* (nm) | α (deg) | β (deg) | γ (deg) | Crystal (Temp) |
|---|---|---|---|---|---|---|---|
| MAX | 0.4829 | 0.4938 | 0.2634 | 100.3 | 101.5 | 129.4 | ORTH (53 K) |
| MIN | 0.4061 | 0.4210 | 0.2505 | 80.8 | 78.8 | 110.6 | |
| MEAN | 0.4367 | 0.4604 | 0.2568 | 89.9 | 89.8 | 118.8 | |
| STD | 0.0117 | 0.0103 | 0.0016 | 2.6 | 3.3 | 2.6 | |
| MAX | 0.5037 | 0.5128 | 0.2677 | 102.5 | 101.2 | 127.3 | ORTH (155 K) |
| MIN | 0.4080 | 0.4146 | 0.2450 | 78.7 | 76.5 | 107.4 | |
| MEAN | 0.4431 | 0.4626 | 0.2564 | 90.8 | 88.9 | 118.3 | |
| STD | 0.0122 | 0.0109 | 0.0027 | 3.5 | 4.2 | 2.8 | |
| MAX | 0.5786 | 0.5369 | 0.2665 | 106.2 | 102.4 | 172.5 | ORTH (231 K) |
| MIN | 0.4093 | 0.4174 | 0.2414 | 77.7 | 72.3 | 103.0 | |
| MEAN | 0.4516 | 0.4650 | 0.2560 | 90.3 | 89.8 | 118.7 | |
| STD | 0.0133 | 0.0122 | 0.0033 | 4.1 | 4.3 | 3.2 | |
| MAX | 0.6159 | 0.7271 | 0.2707 | 112.0 | 105.5 | 141.2 | ORTH (315 K) |
| MIN | 0.4166 | 0.4096 | 0.2287 | 73.6 | 70.7 | 78.5 | |
| MEAN | 0.4686 | 0.4696 | 0.2552 | 91.1 | 88.7 | 119.7 | |
| STD | 0.0169 | 0.0163 | 0.0042 | 5.1 | 5.0 | 3.4 | |
| MAX | 0.9098 | 1.0399 | 0.2713 | 160.1 | 110.8 | 177.9 | ORTH (410 K) |
| MIN | 0.4006 | 0.4127 | 0.1602 | 50.0 | 53.5 | 60.9 | |
| MEAN | 0.4794 | 0.4834 | 0.2541 | 91.3 | 87.7 | 120.0 | |
| STD | 0.0249 | 0.0374 | 0.0058 | 8.2 | 6.3 | 6.3 | |
| MAX | 0.4983 | 0.4951 | 0.2623 | 100.3 | 104.3 | 127.8 | MONO (57 K) |
| MIN | 0.4148 | 0.4071 | 0.2507 | 78.5 | 76.8 | 113.3 | |
| MEAN | 0.4546 | 0.4510 | 0.2569 | 89.6 | 89.7 | 120.3 | |
| STD | 0.0109 | 0.0127 | 0.0016 | 4.0 | 4.2 | 2.5 | |
| MAX | 0.8166 | 0.5075 | 0.2665 | 114.4 | 122.8 | 148.9 | MONO (159 K) |
| MIN | 0.4188 | 0.4115 | 0.2405 | 70.3 | 60.5 | 110.9 | |
| MEAN | 0.4620 | 0.4565 | 0.2563 | 89.7 | 89.9 | 120.3 | |
| STD | 0.0154 | 0.0124 | 0.0026 | 4.6 | 5.4 | 2.5 | |
| MAX | 0.9145 | 0.5466 | 0.2679 | 118.2 | 128.7 | 159.6 | MONO (234 K) |
| MIN | 0.4218 | 0.4115 | 0.2407 | 72.8 | 60.6 | 110.5 | |
| MEAN | 0.4688 | 0.4611 | 0.2558 | 90.4 | 89.2 | 120.5 | |
| STD | 0.0262 | 0.0139 | 0.0034 | 4.9 | 5.8 | 2.9 | |
| MAX | 1.0249 | 0.8035 | 0.2691 | 130.2 | 133.1 | 177.9 | MONO (316 K) |
| MIN | 0.4238 | 0.3971 | 0.2267 | 53.8 | 49.8 | 110.3 | |
| MEAN | 0.4944 | 0.4724 | 0.2547 | 90.1 | 89.9 | 121.7 | |
| STD | 0.0604 | 0.0211 | 0.0044 | 8.4 | 11.5 | 5.0 | |
| MAX | 1.2806 | 1.1672 | 0.2695 | 144.4 | 152.3 | 167.5 | MONO (403 K) |
| MIN | 0.4204 | 0.3943 | 0.2006 | 33.8 | 34.2 | 45.5 | |
| MEAN | 0.5400 | 0.4857 | 0.2530 | 90.3 | 89.8 | 123.8 | |
| STD | 0.1000 | 0.0417 | 0.0059 | 11.1 | 16.2 | 8.7 | |

*The lattice parameters were calculated from the time-averaged coordinates between 5 and 10 ps of the indicated structure and temperature (see Table 3). MAX, maximum; MIN, minimum; MEAN, average; STD, standard deviation. There are from 5600 to 7000 unit cells sampled for each crystal.

**Table 6** Lattice parameters (Run 8: MONO, 234 K) as a function of time (ps)*

| | *a* (nm) | *b* (nm) | *c* (nm) | α (deg) | β (deg) | γ (deg) | Time |
|---|---|---|---|---|---|---|---|
| MAX | 0.5465 | 0.7754 | 0.2862 | 129.0 | 115.1 | 137.8 | 1 |
| MIN | 0.3760 | 0.3990 | 0.2330 | 59.0 | 66.8 | 70.7 | |
| MEAN | 0.4344 | 0.4885 | 0.2575 | 90.1 | 90.1 | 115.2 | |
| STD | 0.0234 | 0.0370 | 0.0076 | 6.9 | 6.8 | 5.8 | |
| MAX | 0.6539 | 0.6935 | 0.2836 | 128.4 | 115.1 | 140.4 | 2 |
| MIN | 0.3631 | 0.3834 | 0.2315 | 54.8 | 59.0 | 90.4 | |
| MEAN | 0.4594 | 0.4655 | 0.2585 | 90.2 | 89.9 | 119.6 | |
| STD | 0.0282 | 0.0292 | 0.0077 | 6.8 | 7.1 | 4.8 | |
| MAX | 0.6465 | 0.6250 | 0.2861 | 123.2 | 122.2 | 140.5 | 3 |
| MIN | 0.3729 | 0.3770 | 0.2341 | 66.7 | 55.9 | 102.9 | |
| MEAN | 0.4831 | 0.4531 | 0.2560 | 89.7 | 89.7 | 122.1 | |
| STD | 0.0314 | 0.0278 | 0.0075 | 6.6 | 6.9 | 4.8 | |
| MAX | 0.8420 | 0.7045 | 0.2864 | 119.6 | 141.8 | 155.5 | 4 |
| MIN | 0.3971 | 0.3648 | 0.2315 | 45.8 | 48.8 | 102.5 | |
| MEAN | 0.4999 | 0.4577 | 0.2575 | 90.0 | 89.5 | 123.1 | |
| STD | 0.0384 | 0.0295 | 0.0075 | 6.5 | 7.2 | 5.0 | |
| MAX | 0.9486 | 0.7221 | 0.2896 | 114.3 | 122.9 | 155.5 | 5 |
| MIN | 0.3995 | 0.3747 | 0.2285 | 49.5 | 47.1 | 100.4 | |
| MEAN | 0.4994 | 0.4567 | 0.2581 | 89.8 | 89.6 | 123.3 | |
| STD | 0.0380 | 0.0292 | 0.0076 | 7.1 | 7.9 | 4.9 | |
| MAX | 0.9577 | 0.6762 | 0.2821 | 125.9 | 133.0 | 164.1 | 6 |
| MIN | 0.3753 | 0.3727 | 0.2266 | 55.6 | 46.8 | 75.9 | |
| MEAN | 0.4898 | 0.4563 | 0.2563 | 90.4 | 90.1 | 122.6 | |
| STD | 0.0392 | 0.0293 | 0.0076 | 7.1 | 8.6 | 5.1 | |
| MAX | 1.0553 | 0.7150 | 0.2833 | 136.3 | 140.6 | 167.7 | 7 |
| MIN | 0.3828 | 0.3729 | 0.2314 | 58.5 | 52.3 | 102.4 | |
| MEAN | 0.4750 | 0.4590 | 0.2578 | 89.7 | 89.7 | 121.2 | |
| STD | 0.0378 | 0.0286 | 0.0076 | 6.9 | 8.4 | 5.3 | |
| MAX | 1.3623 | 0.8541 | 0.2866 | 145.2 | 148.9 | 175.5 | 8 |
| MIN | 0.3803 | 0.3747 | 0.2323 | 66.1 | 60.8 | 91.4 | |
| MEAN | 0.4631 | 0.4641 | 0.2583 | 89.9 | 89.8 | 120.0 | |
| STD | 0.0472 | 0.0308 | 0.0075 | 6.9 | 7.6 | 5.7 | |
| MAX | 1.0019 | 0.7217 | 0.2826 | 124.4 | 148.9 | 162.3 | 9 |
| MIN | 0.3756 | 0.3764 | 0.2284 | 56.4 | 53.6 | 84.7 | |
| MEAN | 0.4509 | 0.4693 | 0.2567 | 90.2 | 89.5 | 118.6 | |
| STD | 0.0401 | 0.0298 | 0.0077 | 6.9 | 7.5 | 5.7 | |
| MAX | 0.8679 | 0.6761 | 0.2825 | 123.8 | 125.4 | 155.6 | 10 |
| MIN | 0.3669 | 0.3847 | 0.2305 | 60.2 | 50.7 | 89.0 | |
| MEAN | 0.4454 | 0.4733 | 0.2575 | 90.3 | 89.9 | 117.9 | |
| STD | 0.0348 | 0.0297 | 0.0075 | 6.7 | 7.1 | 5.3 | |

*MAX, maximum; MIN, minimum; MEAN, average; STD, standard deviation. The lattice parameters at time zero are of single values: 0.4100 (*a*), 0.4800 (*b*), 0.2536 (*c*), 90.0 (α, β), 108.2 (γ).

**Table 7** Time and temperature range in the simulations of superheated and constrained crystals.

| Run Code | Crystal Type | Constraint Type | Time (ps) | Initial* Temp.(K) | Final* Temp.(K) |
|---|---|---|---|---|---|
| D05 | ORTH | NONE | 100 | 465 | 332 |
| D10 | MONO | NONE | 100 | 456 | 337 |
| S10 | MONO | 4-SC | 20 | 480 | 446 |
| S11 | MONO | 3-SC | 100 | 442 | 255 |
| S12 | MONO | 3-SC | 100 | 222 | 144 |
| S13 | ORTH | 3-SC | 33 | 457 | 359 |
| S14 | ORTH | 4-SC | 66 | 340 | 227 |
| S15 | ORTH | 2-SC | 15 | 435 | 379 |

*After 0.1 ps (at which the initial temperature is listed), the temperature decreases gradually. The final temperature is the temperature at which the simulation was stopped (corresponding to the given simulation time).

**Table 8** The lattice parameters of a four-side-constrained ORTH crystal (Run S14 in Table 7) as a function of time.

| | *a* | *b* | *c* | α | β | γ | *t*(ps) |
|---|---|---|---|---|---|---|---|
| MAX | 0.6676 | 0.5430 | 0.2934 | 107.3 | 113.5 | 144.1 | 1 |
| MIN | 0.3966 | 0.3698 | 0.2269 | 70.2 | 62.7 | 102.2 | 1 |
| MEAN | 0.4940 | 0.4462 | 0.2583 | 89.7 | 90.0 | 123.4 | 1 |
| STD | 0.0350 | 0.0257 | 0.0094 | 6.2 | 6.3 | 6.5 | 1 |
| MAX | 0.6296 | 0.5881 | 0.2942 | 110.2 | 120.3 | 154.5 | 5 |
| MIN | 0.3953 | 0.3737 | 0.2277 | 68.7 | 63.4 | 92.1 | 5 |
| MEAN | 0.4939 | 0.4465 | 0.2586 | 90.3 | 89.5 | 123.4 | 5 |
| STD | 0.0317 | 0.0267 | 0.0090 | 6.2 | 6.3 | 6.2 | 5 |
| MAX | 2.1115 | 2.1464 | 0.2914 | 111.6 | 115.2 | 169.8 | 10 |
| MIN | 0.4082 | 0.3738 | 0.2284 | 65.0 | 68.6 | 19.8 | 10 |
| MEAN | 0.4951 | 0.4477 | 0.2583 | 89.8 | 89.8 | 123.2 | 10 |
| STD | 0.0529 | 0.0527 | 0.0090 | 5.9 | 6.4 | 6.8 | 10 |
| MAX | 0.6056 | 0.5540 | 0.2844 | 128.0 | 112.4 | 154.0 | 15 |
| MIN | 0.3993 | 0.3760 | 0.2288 | 68.2 | 64.5 | 103.4 | 15 |
| MEAN | 0.4927 | 0.4471 | 0.2565 | 89.7 | 89.6 | 123.3 | 15 |
| STD | 0.0305 | 0.0255 | 0.0087 | 6.3 | 6.2 | 5.9 | 15 |
| MAX | 0.6307 | 0.5414 | 0.2871 | 113.8 | 113.1 | 114.4 | 20 |
| MIN | 0.4128 | 0.3580 | 0.2309 | 61.1 | 68.8 | 101.2 | 20 |
| MEAN | 0.4935 | 0.4468 | 0.2581 | 90.0 | 90.3 | 123.4 | 20 |
| STD | 0.0322 | 0.0253 | 0.0081 | 6.2 | 6.4 | 6.0 | 20 |

**Table 9** Flipping time (ps) of the dipole in various conditions

| Run Number | Temp (K) | $V_{ex}$ (kJ/mol) | Dipole Position | $t_f$ (ps) |
|---|---|---|---|---|
| 101 | 55 | 2.092 | A | NF |
| 102 | 55 | 4.184 | A | NF |
| 103 | 55 | 8.368 | A | NF |
| 104 | 55 | 16.736 | A | NF |
| 105 | 156 | 2.092 | A | NF |
| 107 | 156 | 8.368 | A | 2.6 |
| 108 | 156 | 16.736 | A | 1.2 |
| 109 | 230 | 2.092 | A | 3.2 |
| 110 | 230 | 4.184 | A | 2.6 |
| 111 | 230 | 8.368 | A | 2.6 |
| 112 | 230 | 16.736 | A | 0.5 |
| 113 | 330 | 2.092 | A | 1.3 |
| 114 | 330 | 4.184 | A | 1.3 |
| 115 | 330 | 8.368 | A | 1.3 |
| 116 | 330 | 16.736 | A | 0.5 |
| 117 | 55 | 2.092 | B | 2.5 |
| 119 | 55 | 4.184 | B | 2.2 |
| 121 | 55 | 8.368 | B | 0.8 |
| 123 | 55 | 16.736 | B | 0.5 |
| 125 | 156 | 2.092 | B | 2.4 |
| 127 | 156 | 4.184 | B | 1.3 |
| 129 | 156 | 8.368 | B | 1.0 |
| 131 | 156 | 16.736 | B | 0.5 |
| 133 | 230 | 2.092 | B | 1.8 |
| 135 | 230 | 4.184 | B | 1.7 |
| 137 | 230 | 8.368 | B | 1.4 |
| 139 | 230 | 16.736 | B | 0.5 |
| 141 | 330 | 2.092 | B | 1.9 |
| 143 | 330 | 4.184 | B | 1.6 |
| 145 | 330 | 8.368 | B | 1.4 |
| 147 | 330 | 16.736 | B | 0.6 |
| 118 | 55 | 2.092 | C | 5.0 |
| 120 | 55 | 4.184 | C | 1.3 |
| 122 | 55 | 8.368 | C | 1.1 |
| 124 | 55 | 16.736 | C | 0.8 |
| 126 | 156 | 2.096 | C | NF |
| 128 | 156 | 4.184 | C | NF |
| 132 | 156 | 16.736 | C | 2.3 |
| 134 | 230 | 2.092 | C | NF |
| 136 | 230 | 4.184 | C | NF |
| 138 | 230 | 8.368 | C | 1.8 |
| 140 | 230 | 16.736 | C | 1.2 |
| 142 | 330 | 2.092 | C | NF |
| 144 | 330 | 4.184 | C | 1.5 |
| 146 | 330 | 8.368 | C | 1.7 |
| 148 | 330 | 16.736 | C | 1.3 |

**Table 10** Temperature, density, and *gauche* concentration as a function of time in the full atom simulations.

| Run Number | Time (ps) | Temp (K) | Density ($Mg/m^3$) | Gauche (%) |
|---|---|---|---|---|
| XR01 | 1 | 110 | 1.1767 | 0.00 |
| | 2 | 105 | 1.0663 | 0.00 |
| | 3 | 114 | 1.1459 | 0.00 |
| | 4 | 112 | 1.1296 | 0.00 |
| | 5 | 112 | 1.1369 | 0.00 |
| XR02 | 5 | 245 | 1.0986 | 0.00 |
| | 6 | 247 | 1.1198 | 0.04 |
| | 7 | 246 | 1.1057 | 0.03 |
| | 8 | 248 | 1.1225 | 0.02 |
| | 9 | 245 | 1.1085 | 0.01 |
| | 10 | 247 | 1.1312 | 0.00 |
| XR04 | 2 | 313 | 1.0701 | 0.18 |
| | 3 | 310 | 1.0898 | 0.29 |
| | 4 | 313 | 1.1112 | 0.38 |
| | 5 | 307 | 1.0921 | 0.47 |
| | 6 | 313 | 1.1112 | 0.42 |
| | 7 | 309 | 1.0980 | 0.51 |

**Table 11** Time averaged volume and densities calculated with two different methods.

| Run Number[a] | Time (ps) | Lattice Method | | Box-Sampling Mathod |
|---|---|---|---|---|
| | | Volume[b] ($\times 10^{-3}$ nm$^3$) | Density (Mg/m$^3$) | Density (Mg/m$^3$) |
| ORTH | 0 | 45.33 | 1.03 | 1.01 |
| MONO | 0 | 47.41 | 0.98 | 0.98 |
| XR01 | 2–5 | 42.38 | 1.11 | 1.12 |
| XR02 | 5–10 | 42.53 | 1.10 | 1.13 |
| XR04 | 2–7 | 43.31 | 1.08 | 1.10 |
| D01 | 5–10 | 45.24 | 1.03 | 1.04 |
| D02 | 5–10 | 46.27 | 1.01 | 1.02 |
| D03 | 5–10 | 47.15 | 0.99 | 1.00 |
| D04 | 5–10 | 48.77 | 0.96 | 0.98 |
| D05 | 5–10 | 50.96 | 0.91 | 0.95 |
| D06 | 5–10 | 45.47 | 1.02 | 1.01 |
| D07 | 5–10 | 46.67 | 1.00 | 1.00 |
| D08 | 5–10 | 47.64 | 0.98 | 0.99 |
| D09 | 5–10 | 50.61 | 0.92 | 0.96 |
| D10 | 5–10 | 55.14 | 0.85 | 0.90 |

[a]The numbers start with D are the sumulations numbered in Table 3.
[b]Time and position average, the volume of one primary unit cell consisting of 2 $CH_2$ units.

**Table 12** Standard deviations (nm) from initial structure in the full atom simulations.

| Run Number | ΔX | ΔY | ΔZ | ΔXYZ | ΔR | |
|---|---|---|---|---|---|---|
| XR01[a] | 0.06 | 0.19 | | 0.01 | 0.27 | 0.20 |
| XR02[b] | 0.06 | 0.18 | | 0.01 | 0.26 | 0.19 |
| XR04[c] | 0.08 | 0.16 | | 0.02 | 0.26 | 0.18 |

[a]Time averaged structure between 2 to 5 ps.
[b]Time averaged structure between 5 to 10 ps.
[c]Time averaged structure between 2 to 7 ps.

**Table 13** Lattice parameter distributions as a function of time in the full atom simulation XR01.*

| | *a* | *b* | *c* | α | β | γ | t (ps) |
|---|---|---|---|---|---|---|---|
| MAX | 0.5221 | 0.4969 | 0.2648 | 100.10 | 102.0 | 136.5 | 1 |
| MIN | 0.3907 | 0.3614 | 0.2426 | 81.1 | 79.2 | 106.5 | 1 |
| MEAN | 0.4453 | 0.4171 | 0.2540 | 89.8 | 90.0 | 122.1 | 1 |
| STD | 0.0155 | 0.0179 | 0.0030 | 2.3 | 2.1 | 4.3 | 1 |
| MAX | 0.5836 | 0.5617 | 0.2634 | 101.6 | 100.2 | 142.0 | 2 |
| MIN | 0.3914 | 0.3799 | 0.2410 | 71.9 | 80.9 | 91.1 | 2 |
| MEAN | 0.4404 | 0.4524 | 0.2524 | 89.8 | 90.2 | 118.9 | 2 |
| STD | 0.0215 | 0.0283 | 0.0030 | 2.8 | 2.4 | 6.7 | 2 |
| MAX | 0.5069 | 0.9567 | 0.2627 | 119.5 | 103.6 | 152.6 | 3 |
| MIN | 0.3864 | 0.3622 | 0.2412 | 72.4 | 80.8 | 37.1 | 3 |
| MEAN | 0.4314 | 0.4376 | 0.2520 | 90.1 | 90.0 | 118.4 | 3 |
| STD | 0.0140 | 0.0386 | 0.0031 | 3.2 | 2.3 | 8.4 | 3 |
| MAX | 0.6265 | 0.5169 | 0.2644 | 105.9 | 103.8 | 138.2 | 4 |
| MIN | 0.3986 | 0.3584 | 0.2399 | 75.0 | 79.5 | 96.1 | 4 |
| MEAN | 0.4421 | 0.4305 | 0.2523 | 90.0 | 90.0 | 119.9 | 4 |
| STD | 0.0189 | 0.0225 | 0.0032 | 2.9 | 2.6 | 5.2 | 4 |
| MAX | 0.5254 | 0.5451 | 0.2665 | 105.5 | 105.8 | 136.9 | 5 |
| MIN | 0.3782 | 0.3691 | 0.2420 | 78.4 | 78.8 | 95.9 | 5 |
| MEAN | 0.4354 | 0.4309 | 0.2532 | 89.6 | 90.1 | 118.4 | 5 |
| STD | 0.0146 | 0.0219 | 0.0033 | 2.8 | 2.6 | 5.1 | 5 |

*Lattice parameters *a*, *b*, *c*, α, β, and γ for initial ORTH crystal are 0.4900, 0.4400, 0.2536 nm, and 90, 90, 124°, respectively.

**Table 14** Lattice parameter distribution as a function of time in the full atom simulation XR02.

| | *a* | *b* | *c* | α | β | γ | t (ps) |
|---|---|---|---|---|---|---|---|
| MAX | 0.5798 | 0.5076 | 0.2726 | 108.3 | 107.2 | 147.5 | 1 |
| MIN | 0.3750 | 0.3442 | 0.2356 | 66.5 | 75.9 | 101.1 | 1 |
| MEAN | 0.4562 | 0.4270 | 0.2541 | 89.7 | 90.1 | 122.0 | 1 |
| STD | 0.0230 | 0.0203 | 0.0049 | 4.1 | 4.0 | 5.4 | 1 |
| MAX | 0.5883 | 0.5748 | 0.2731 | 106.5 | 106.9 | 140.5 | 2 |
| MIN | 0.3800 | 0.3736 | 0.2284 | 65.0 | 76.4 | 95.0 | 2 |
| MEAN | 0.4418 | 0.4499 | 0.2529 | 89.7 | 90.0 | 119.0 | 2 |
| STD | 0.0193 | 0.0258 | 0.0047 | 4.01 | 3.4 | 6.1 | 2 |
| MAX | 0.5589 | 0.5515 | 0.2697 | 105.7 | 101.4 | 142.2 | 5 |
| MIN | 0.3777 | 0.3680 | 0.2370 | 68.6 | 74.7 | 97.7 | 5 |
| MEAN | 0.4452 | 0.4384 | 0.2527 | 89.6 | 89.9 | 118.3 | 5 |
| STD | 0.0189 | 0.0243 | 0.0046 | 4.0 | 3.3 | 5.7 | 5 |
| MAX | 0.5120 | 0.5956 | 0.2711 | 104.9 | 105.6 | 140.0 | 6 |
| MIN | 0.3799 | 0.3468 | 0.2307 | 65.1 | 79.1 | 87.5 | 6 |
| MEAN | 0.4358 | 0.4319 | 0.2536 | 89.5 | 90.1 | 117.6 | 6 |
| STD | 0.0158 | 0.0240 | 0.0046 | 4.0 | 3.0 | 5.4 | 6 |
| MAX | 0.5581 | 0.6530 | 0.2732 | 118.7 | 112.6 | 150.4 | 7 |
| MIN | 0.3922 | 0.3634 | 0.2336 | 70.1 | 75.1 | 82.5 | 7 |
| MEAN | 0.4465 | 0.4286 | 0.2540 | 89.9 | 90.0 | 118.7 | 7 |
| STD | 0.0185 | 0.0221 | 0.0046 | 3.7 | 3.2 | 5.3 | 7 |
| MAX | 0.5159 | 0.5462 | 0.2691 | 107.6 | 105.7 | 139.8 | 8 |
| MIN | 0.3813 | 0.3513 | 0.2385 | 72.0 | 79.4 | 99.2 | 8 |
| MEAN | 0.4351 | 0.4305 | 0.2537 | 90.3 | 89.9 | 117.2 | 8 |
| STD | 0.0158 | 0.0215 | 0.0046 | 3.6 | 2.9 | 5.0 | 8 |
| MAX | 0.5220 | 0.5186 | 0.2686 | 101.3 | 102.3 | 145.4 | 9 |
| MIN | 0.3843 | 0.3686 | 0.2359 | 74.5 | 77.8 | 99.4 | 9 |
| MEAN | 0.4421 | 0.4299 | 0.2531 | 89.9 | 90.0 | 117.5 | 9 |
| STD | 0.0161 | 0.0219 | 0.0044 | 3.7 | 3.0 | 5.0 | 9 |
| MAX | 0.5122 | 0.5675 | 0.2680 | 104.5 | 101.3 | 140.1 | 10 |
| MIN | 0.3835 | 0.3542 | 0.2361 | 73.8 | 78.6 | 94.1 | 10 |
| MEAN | 0.4385 | 0.4251 | 0.2528 | 89.5 | 90.2 | 117.3 | 10 |

**Table 15** Lattice parameter distribution as a functions of time in full atom simulation XR04.

| | *a* | *b* | *c* | α | β | γ | t (ps) |
|---|---|---|---|---|---|---|---|
| MAX | 0.6246 | 0.6254 | 0.2738 | 128.9 | 115.4 | 168.0 | 2 |
| MIN | 0.3742 | 0.3112 | 0.2085 | 57.6 | 35.6 | 88.9 | 2 |
| MEAN | 0.4443 | 0.4501 | 0.2085 | 89.7 | 90.0 | 119.1 | 2 |
| STD | 0.0209 | 0.0269 | 0.0055 | 4.6 | 4.0 | 6.4 | 2 |
| MAX | 0.6043 | 0.7114 | 0.2729 | 125.5 | 119.7 | 157.9 | 3 |
| MIN | 0.3505 | 0.3590 | 0.2075 | 23.3 | 40.5 | 75.7 | 3 |
| MEAN | 0.4451 | 0.4516 | 0.2525 | 90.6 | 90.0 | 119.3 | 3 |
| STD | 0.0209 | 0.0304 | 0.0054 | 5.3 | 4.1 | 6.8 | 3 |
| MAX | 0.6582 | 0.5604 | 0.2717 | 118.3 | 128.0 | 172.0 | 4 |
| MIN | 0.3814 | 0.3574 | 0.2047 | 55.6 | 28.6 | 87.4 | 4 |
| MEAN | 0.4476 | 0.4345 | 0.2522 | 90.6 | 89.8 | 120.6 | 4 |
| STD | 0.0219 | 0.0269 | 0.0053 | 4.4 | 3.9 | 5.9 | 4 |
| MAX | 0.6732 | 0.7520 | 0.2725 | 126.7 | 122.3 | 157.0 | 5 |
| MIN | 0.3809 | 0.3634 | 0.2133 | 7.3 | 40.8 | 69.3 | 5 |
| MEAN | 0.4479 | 0.4425 | 0.2524 | 89.9 | 90.0 | 118.9 | 5 |
| STD | 0.0217 | 0.0266 | 0.0052 | 4.9 | 4.1 | 6.0 | 5 |
| MAX | 0.8669 | 0.5933 | 0.2730 | 150.9 | 108.3 | 154.9 | 6 |
| MIN | 0.3370 | 0.3545 | 0.2140 | 51.4 | 54.9 | 87.4 | 6 |
| MEAN | 0.4413 | 0.4359 | 0.2532 | 89.3 | 90.1 | 117.9 | 6 |
| STD | 0.0210 | 0.0260 | 0.0054 | 4.7 | 3.6 | 5.9 | 6 |
| MAX | 0.6907 | 0.6053 | 0.2725 | 126.5 | 116.7 | 175.5 | 7 |
| MIN | 0.3711 | 0.3621 | 0.2086 | 51.2 | 54.2 | 85.6 | 7 |
| MEAN | 0.4492 | 0.4327 | 0.2536 | 89.7 | 90.1 | 118.6 | 7 |
| STD | 0.0212 | 0.0237 | 0.0053 | 4.5 | 3.6 | 5.5 | 7 |

**Table 16** Location of *gauche* bonds in the crystal of XR04 at different times*

| *n* | *ix* | *iy* | *iz* | *gg* | *kink* |
|---|---|---|---|---|---|
| Time = 2 ps: | | | | | |
| 145 | 3 | 1 | 45 | *gg* | |
| 146 | 3 | 1 | 46 | | |
| 197 | 4 | 1 | 47 | | |
| 402 | 1 | 2 | 2 | | |
| 897 | 2 | 3 | 47 | | |
| 1352 | 4 | 4 | 2 | | |
| 2402 | 1 | 7 | 2 | | |
| 2497 | 2 | 7 | 47 | | |
| 3297 | 2 | 9 | 47 | | |
| 3597 | 8 | 9 | 47 | | |
| 3996 | 8 | 10 | 46 | | |
| 5697 | 2 | 15 | 47 | | |
| 7301 | 3 | 19 | 1 | | |
| 8201 | 5 | 21 | 1 | | |
| 8247 | 5 | 21 | 47 | | |
| 8947 | 3 | 23 | 47 | | |
| Time = 3 ps: | | | | | |
| 145 | 3 | 1 | 45 | *gg* | |
| 146 | 3 | 1 | 46 | | |
| 197 | 4 | 1 | 47 | | |
| 301 | 7 | 1 | 1 | | |
| 402 | 1 | 2 | 2 | | |
| 897 | 2 | 3 | 47 | | |
| 1352 | 4 | 4 | 2 | | |
| 1626 | 1 | 5 | 26 | | *k* |
| 1628 | 1 | 5 | 28 | | |
| 1901 | 7 | 5 | 1 | | |
| 2402 | 1 | 7 | 2 | | |
| 2646 | 5 | 7 | 46 | | |
| 3297 | 2 | 9 | 47 | | |
| 3597 | 8 | 9 | 47 | | |
| 3645 | 1 | 10 | 45 | | |
| 3996 | 8 | 10 | 46 | | |
| 5347 | 3 | 14 | 47 | | |
| 5901 | 7 | 15 | 1 | | |
| 7102 | 7 | 18 | 2 | | |
| 7301 | 3 | 19 | 1 | | |
| 7951 | 8 | 20 | 1 | | |

(Continued)

**Table 16** Location of *gauche* bonds in the crystal of XR04 in different time, continued

| *n* | *ix* | *iy* | *iz* | *gg* | *kink* |
|---|---|---|---|---|---|
| 8294 | 6 | 21 | 44 | *gg* | |
| 8296 | 6 | 21 | 46 | | |
| 8947 | 3 | 23 | 47 | | |
| 9351 | 4 | 24 | 1 | | |
| 9595 | 8 | 24 | 45 | | |
| Time = 4 ps: | | | | | |
| 45 | 1 | 1 | 45 | | *k* |
| 47 | 1 | 1 | 47 | | |
| 96 | 2 | 1 | 46 | | |
| 145 | 3 | 1 | 45 | *gg* | |
| 146 | 3 | 1 | 46 | | |
| 197 | 4 | 1 | 47 | | |
| 301 | 7 | 1 | 1 | | |
| 351 | 8 | 1 | 1 | | |
| 402 | 1 | 2 | 2 | | |
| 897 | 2 | 3 | 47 | | |
| 1047 | 5 | 3 | 47 | | |
| 1051 | 6 | 3 | 1 | | |
| 1901 | 7 | 5 | 1 | | |
| 2351 | 8 | 6 | 1 | | |
| 2402 | 1 | 7 | 2 | | |
| 2497 | 2 | 7 | 47 | | |
| 3151 | 8 | 8 | 1 | | |
| 3196 | 8 | 8 | 46 | | |
| 3297 | 2 | 9 | 47 | | |
| 3597 | 8 | 9 | 47 | | |
| 5901 | 7 | 15 | 1 | | |
| 6391 | 8 | 16 | 41 | | *k* |
| 6393 | 8 | 16 | 43 | | *k* |
| 6395 | 8 | 16 | 45 | | |
| 7951 | 8 | 20 | 1 | | |
| 8294 | 6 | 21 | 44 | | *k* |
| 8296 | 6 | 21 | 46 | | |
| 8647 | 5 | 22 | 47 | | |
| 9096 | 6 | 23 | 46 | | |
| 9291 | 2 | 24 | 41 | | *k* |
| 9293 | 2 | 24 | 43 | | |
| 9329 | 3 | 24 | 29 | | |
| 9594 | 8 | 24 | 44 | *gg* | |
| 9595 | 8 | 24 | 45 | | |

(Continued)

**Table 16** Location of *gauche* bonds in the crystal of XR04 in different time, continued

| *n* | *ix* | *iy* | *iz* | *gg* | *kink* |
|---|---|---|---|---|---|
| Time = 5 ps: | | | | | |
| 1 | 1 | 1 | 1 | | |
| 45 | 1 | 1 | 45 | | *k* |
| 47 | 1 | 1 | 47 | | |
| 96 | 2 | 1 | 46 | | |
| 97 | 2 | 1 | 47 | | |
| 145 | 3 | 1 | 45 | *gg* | |
| 146 | 3 | 1 | 46 | | |
| 197 | 4 | 1 | 47 | | |
| 301 | 7 | 1 | 1 | | |
| 351 | 8 | 1 | 1 | | |
| 402 | 1 | 2 | 2 | | |
| 1047 | 5 | 3 | 47 | | |
| 1626 | 1 | 5 | 26 | | *k* |
| 1628 | 1 | 5 | 28 | | |
| 1751 | 4 | 5 | 1 | | |
| 1901 | 7 | 5 | 1 | | |
| 2351 | 8 | 6 | 1 | | |
| 2402 | 1 | 7 | 2 | | |
| 2497 | 2 | 7 | 47 | | |
| 3151 | 8 | 8 | 1 | | |
| 3196 | 8 | 8 | 46 | | |
| 3201 | 1 | 9 | 1 | | |
| 3597 | 8 | 9 | 47 | | |
| 5851 | 6 | 15 | 1 | | |
| 6393 | 8 | 16 | 43 | | *k* |
| 6395 | 8 | 16 | 45 | | |
| 7197 | 8 | 18 | 47 | | |
| 7951 | 8 | 20 | 1 | | |
| 8294 | 6 | 21 | 44 | | *k* |
| 8296 | 6 | 21 | 46 | | |
| 8647 | 5 | 22 | 47 | | |
| 8751 | 8 | 22 | 1 | | |
| 9095 | 6 | 23 | 45 | *gg* | |
| 9096 | 6 | 23 | 46 | | |
| 9291 | 2 | 24 | 41 | | *k* |
| 9293 | 2 | 24 | 43 | | |
| 9453 | 6 | 24 | 3 | | |
| 9558 | 8 | 24 | 8 | | |
| 9588 | 8 | 24 | 38 | | |
| 9594 | 8 | 24 | 44 | *gg* | |
| 9595 | 8 | 24 | 45 | | *k* |
| 9597 | 8 | 24 | 47 | | |

(Continued)

**Table 16** Location of *gauche* bonds in the crystal of XR04 in different time, continued

| *n* | *ix* | *iy* | *iz* | *gg* | *kink* |
|---|---|---|---|---|---|
| Time = 6 ps: | | | | | |
| 1 | 1 | 1 | 1 | | |
| 45 | 1 | 1 | 45 | | |
| 97 | 2 | 1 | 47 | | |
| 145 | 3 | 1 | 45 | *gg* | |
| 146 | 3 | 1 | 46 | | |
| 197 | 4 | 1 | 47 | | |
| 302 | 7 | 1 | 2 | | |
| 351 | 8 | 1 | 1 | | |
| 797 | 8 | 2 | 47 | | |
| 1626 | 1 | 5 | 26 | | *k* |
| 1628 | 1 | 5 | 28 | | |
| 1751 | 4 | 5 | 1 | | |
| 2351 | 8 | 6 | 1 | | |
| 2402 | 1 | 7 | 2 | | |
| 2497 | 2 | 7 | 47 | | |
| 3196 | 8 | 8 | 46 | | |
| 3201 | 1 | 9 | 1 | | |
| 4797 | 8 | 12 | 47 | | |
| 5851 | 6 | 15 | 1 | | |
| 6393 | 8 | 16 | 43 | | *k* |
| 6395 | 8 | 16 | 45 | | |
| 7951 | 8 | 20 | 1 | | |
| 8045 | 1 | 21 | 45 | | |
| 8294 | 6 | 21 | 44 | | *k* |
| 8296 | 6 | 21 | 46 | | |
| 8751 | 8 | 22 | 1 | | |
| 8797 | 8 | 22 | 47 | | |
| 9096 | 6 | 23 | 46 | | |
| 9291 | 2 | 24 | 41 | | *k* |
| 9293 | 2 | 24 | 43 | | |
| 9494 | 6 | 24 | 44 | | |
| 9558 | 8 | 24 | 8 | | *k* |
| 9560 | 8 | 24 | 10 | | |
| 9586 | 8 | 24 | 36 | | *k* |
| 9588 | 8 | 24 | 38 | | |
| 9594 | 8 | 24 | 44 | *gg* | |
| 9595 | 8 | 24 | 45 | | *k* |
| 9597 | 8 | 24 | 47 | | |

(Continued)

**Table 16** Location of *gauche* bonds in the crystal of XR04 in different time, continued

| *n* | *ix* | *iy* | *iz* | *gg* | *kink* |
|---|---|---|---|---|---|
| Time = 7 ps: | | | | | |
| 1 | 1 | 1 | 1 | | |
| 45 | 1 | 1 | 45 | | *k* |
| 47 | 1 | 1 | 47 | | |
| 97 | 2 | 1 | 47 | | |
| 145 | 3 | 1 | 45 | | |
| 197 | 4 | 1 | 47 | | |
| 302 | 7 | 1 | 2 | | |
| 351 | 8 | 1 | 1 | | |
| 497 | 2 | 2 | 47 | | |
| 797 | 8 | 2 | 47 | | |
| 897 | 2 | 3 | 47 | | |
| 1626 | 1 | 5 | 26 | | *k* |
| 1628 | 1 | 5 | 28 | | |
| 1751 | 4 | 5 | 1 | | |
| 2351 | 8 | 6 | 1 | | |
| 2396 | 8 | 6 | 46 | *gg* | |
| 2397 | 8 | 6 | 47 | | |
| 2497 | 2 | 7 | 47 | | |
| 3196 | 8 | 8 | 46 | | |
| 3201 | 1 | 9 | 1 | | |
| 4797 | 8 | 12 | 47 | | |
| 6393 | 8 | 16 | 43 | | k |
| 6395 | 8 | 16 | 45 | | |
| 6651 | 6 | 17 | 1 | | |
| 6897 | 2 | 18 | 47 | | |
| 7196 | 8 | 18 | 46 | *gg* | |
| 7197 | 8 | 18 | 47 | | |
| 7946 | 7 | 20 | 46 | | |
| 7997 | 8 | 20 | 47 | | |
| 8045 | 1 | 21 | 45 | | |
| 8294 | 6 | 21 | 44 | | |
| 8296 | 6 | 21 | 46 | | |
| 8751 | 8 | 22 | 1 | | *k* |
| 8753 | 8 | 22 | 3 | | |
| 8797 | 8 | 22 | 47 | | |
| 9095 | 6 | 23 | 45 | *gg* | |
| 9096 | 6 | 23 | 46 | | |
| 9201 | 1 | 24 | 1 | | |
| 9494 | 6 | 24 | 44 | | |
| 9551 | 8 | 24 | 1 | | |
| 9558 | 8 | 24 | 8 | | |
| 9586 | 8 | 24 | 36 | | *k* |

(Continued)

**Table 16** Location of *gauche* bonds in the crystal of XR04 in different time, continued

| *n* | *ix* | *iy* | *iz* | *gg* | *kink* |
|---|---|---|---|---|---|
| 9588 | 8 | 24 | 38 | | |
| 9594 | 8 | 24 | 44 | | *k* |
| 9595 | 8 | 24 | 45 | | *k* |
| 9597 | 8 | 24 | 47 | | |

*There are 9024 torsional bonds in a crystal. The index *n* is the sequent number of the carbon position that construct a torsional bond with next consective 3 carbons, *ix* and *iy* are the two-dimensional matrix indices to label the chain position in Fig. 1b, *iz* is the first carbon position of a *gauche* bond in the chain corresponding to *ix* and *iy*, *gg* indicates a double *gauche*, and *k* indicates a *kink* (*gauche-trans-gauche*).

# APPENDIX D

## A FORTRAN PROGRAM FOR THE CALCULATION OF CRYSTAL LATTICE PARAMETERS

```
c*****************************************************************************************
      program lattice
c     VAX/VMS version
c=====
c           PROGRAM IDENTIFICATION
c=====
c           Calculation of crystal lattice parameters a, b, c, alpha, beta, and gamma from
c     the data-set of the carbon coordinates.
c           This code is input data-set oriented.  The array in the carbon position data-set
c     is specified in the subroutine in Appendix E.  Each variable is identified below:
c
c     Arrays and Variables              Identification
c
c     xyz(3, 9600)                      Cartesian coordinates of carbon atoms
c     abc(3, 9600)                      Lattice dimensions a, b, and c
c     alpha, beta, gamma                Lattice angles
c     itype                             Type of crystal (see Appendix E)
c     nth                               Number of carbon atoms in each chain
c     icx                               Number of chains in the x-dimension
c     icy                               Number of chains in the y-dimension
c     n                                 Total number of carbon atoms in the crystal
c
c*****************************************************************************************
c
     implicit real*8 (a-h, o-z)
     dimension xyz(3,9600),alpha(9600),beta(9600),gamma(9600)
     dimension abc(3,9600),xyz1(3,9600)
c
c Statement function for spatial distance
c
      r(x1,y1,z1,x2,y2,z2) = sqrt((x2-x1)**2 +
    $      (y2-y1)**2 + (z2-z1)**2)
c
c Statement function for angle in degree
c
      angl(x1,y1,z1,x2,y2,z2,x3,y3,z3) = (180.0/3.141516)*acos(
    $      -((x2-x1)*(x3-x1)+(y2-y1)*(y3-y1)+(z2-z1)*
    1      (z3-z1))/(sqrt((x2-x1)**2+(y2-y1)**2+(z2-z1)**2)*
    2      sqrt((x3-x1)**2+(y3-y1)**2+(z3-z1)**2)))
c
c     open(unit=5,file='mytape:[]d8006t10.',status = 'old')
      open(unit=5,file='[luke.d8dat]d809b.ave',status = 'old')
      open(unit=8,file='abc.',status = 'unknown')
      open(unit=9,file='ang.',status = 'unknown')
c
```

```
      write(8,*) 'unit 8, ip and unit cell a, b, c'
      write(9,*) 'unit 9, unit cell alpha, beta, gamma'
c
c     ??? Cryatal Type Input: ???
c
      write(8,*) 'itpye=?'
c
c     itype = 111 (mono) 16x12x50
c     itype = 222 (orth,b) 8x24x50
c     itype = 333 (orth,a) 12x16x50
c
      itype = 111
c
      write(8,*) 'itype=', itype
c
      if(itype.eq.111) then
          nth = 50
          icx = 16
          icy = 12
c
      else if(itype.eq.222) then
c
          nth = 50
          icx = 8
          icy = 24
c
      else
c
          nth = 50
          icx = 12
          icy = 16
      end if
c
      n = icx * icy * nth
c
      do 1 ip = 1,9600
          xyz(1,ip) = 0.0d0
          xyz(2,ip) = 0.0d0
          xyz(3,ip) = 0.0d0
          abc(1,ip) = 0.0d0
          abc(2,ip) = 0.0d0
          abc(3,ip) = 0.0d0
          alpha(ip) = 0.0d0
          beta(ip) = 0.0d0
          gamma(ip) = 0.0d0
 1    continue
c
    do 10 j = 1,n
          read (5,*) xyz1(1,j),xyz1(2,j),xyz1(3,j)
 10  continue
```

```
c
c       Calculate the mid-point coordinates of each bond
c
        m = 0
c
      do 11 k = 1, n-1
c
            if(mod(k,nth).eq.0) go to 11
c
            m = m + 1
            xyz(1,m) = 0.5d0 * (xyz1(1,k) + xyz1(1,k+1))
            xyz(2,m) = 0.5d0 * (xyz1(2,k) + xyz1(2,k+1))
            xyz(3,m) = 0.5d0 * (xyz1(3,k) + xyz1(3,k+1))
            write(8,102) m,xyz(1,k),xyz(2,k),xyz(3,k)
 11   continue
c
        if(itype.ne.111) goto 222
c
        nl = 0
c       number of latices nl
c
        ip = 0
        icym1 = icy - 1
        nthm1 = nth - 1
c
20      continue
c
      do 21 iy = 1,icym1
            do 22 ix = 1,icx
                  do 23 iz = 1,nthm1
                        ip = ip + 1
c
c Avoid two bottom atoms and the right edge chains
c
                        if(mod(ip+1,nthm1).eq.0.or.mod(ip,nthm1)
     $                    .eq.0) goto 24
                        if(ip.gt.(nthm1*(icx-1)+(iy-1)*nthm1*icx)
     $                    .and.ip.lt.(nthm1*icx+1+(iy-1)*nthm1*icx)) goto 24
c
                        x0 = 0.0d0
                        y0 = 0.0d0
                        z0 = 0.0d0
                        xa = 0.0d0
                        ya = 0.0d0
                        za = 0.0d0
                        xb = 0.0d0
                        yb = 0.0d0
                        zb = 0.0d0
                        xc = 0.0d0
                        yc = 0.0d0
                        zc = 0.0d0
```

```
c
                ia = 0
                ib = 0
c
                if(iy.ne.2*(iy/2)) then
c
                    do 25 i = 1,nthm1
c
                        if(abs(xyz(3,ip)-xyz(3,ix*nthm1+icx
     $                    *nthm1*(iy-1)+i)).lt.0.6) ia=i
c
                        if(abs(xyz(3,ip)-xyz(3,(ix-1)*nthm1
     $                    +nthm1*icx*iy+i)).lt.0.6) ib=i
c
  25                continue
c
                if(ia.eq.0.or.ib.eq.0) goto 23
                x0 = xyz(1,ip)
                y0 = xyz(2,ip)
                z0 = xyz(3,ip)
                xa = xyz(1,(ix*nthm1+icx*nthm1*(iy-1)+ia))
                ya = xyz(2,(ix*nthm1+icx*nthm1*(iy-1)+ia))
                za = xyz(3,(ix*nthm1+icx*nthm1*(iy-1)+ia))
                xb = xyz(1,((ix-1)*nthm1+nthm1*icx*iy+ib))
                yb = xyz(2,((ix-1)*nthm1+nthm1*icx*iy+ib))
                zb = xyz(3,((ix-1)*nthm1+nthm1*icx*iy+ib))
                xc = xyz(1,(ip+2))
                yc = xyz(2,(ip+2))
                zc = xyz(3,(ip+2))
c
                else
c
                    do 26 i = 1,nthm1
c
                        if(abs(xyz(3,ip)-xyz(3,ix*nthm1+
     $                    nthm1*icx*iy+i)).lt.0.6) ia=i
                        if(abs(xyz(3,ip)-xyz(3,(ix-1)*nthm1
     $                    +nthm1*icx*iy+i)).lt.0.6) ib=i
c
  26                continue
c
                if(ia.eq.0.or.ib.eq.0) goto 23
                xb = xyz(1,ip)
                yb = xyz(2,ip)
                zb = xyz(3,ip)
                xa = xyz(1,(ix*nthm1+icx*nthm1*iy+ia))
                ya = xyz(2,(ix*nthm1+icx*nthm1*iy+ia))
                za = xyz(3,(ix*nthm1+icx*nthm1*iy+ia))
                x0 = xyz(1,((ix-1)*nthm1+nthm1*icx*iy+ib))
                y0 = xyz(2,((ix-1)*nthm1+nthm1*icx*iy+ib))
                z0 = xyz(3,((ix-1)*nthm1+nthm1*icx*iy+ib))
```

```
                    xc = xyz(1,((ix-1)*nthm1+nthm1*icx*iy+ib+2))
                    yc = xyz(2,((ix-1)*nthm1+nthm1*icx*iy+ib+2))
                    zc = xyz(3,((ix-1)*nthm1+nthm1*icx*iy+ib+2))
c
                    ccc = r(x0,y0,z0,xc,yc,zc)
c
                    if(ccc.gt.4.0) goto 23
c
                    endif
c
c       Calculate a, b, c in Angstom
c
                    nl = nl + 1
                    abc(1,nl) = r(x0,y0,z0,xa,ya,za)
                    abc(2,nl) = r(x0,y0,z0,xb,yb,zb)
                    abc(3,nl) = r(x0,y0,z0,xc,yc,zc)
c
                    write(8,102) nl,abc(1,nl),abc(2,nl),abc(3,nl)
 102    format(' ',i4, 3e20.10)
c
 19     continue
c
                    alpha(nl) = angl(x0,y0,z0,xb,yb,zb,xc,yc,zc)
c
                    beta(nl) = angl(x0,y0,z0,xa,ya,za,xc,yc,zc)
c
                    gamma(nl) = angl(x0,y0,z0,xb,yb,zb,xa,ya,za)
c
                    write(9,*) alpha(nl),beta(nl),gamma(nl)
24                  continue
  23              continue
  22          continue
  21    continue
c
222     continue
c
        nl = 0
c       number of latices nl
c
        ip = 0
        icym2 = icy - 2
        nthm1 = nth - 1
c
      do 31 iy = 1,icym2
           do 32 ix = 1,icx
                do 33 iz = 1,nthm1
                    ip = ip + 1
c
                    if(iy.eq.1.or.ix.eq.(icx-1)) goto 34
```

```
c
c Avoid two bottom atoms (and the right edge chains)
c
                    if(mod(ip+1,nthm1).eq.0.or.mod(ip,nthm1).eq.0) goto 34
                    if(ip.gt.(nthm1*(icx-1)+(iy-1)*nthm1*icx).and.
     $                ip.lt.(nthm1*icx+1+(iy-1)*nthm1*icx)) goto 34
c
                    x0 = 0.0d0
                    y0 = 0.0d0
                    z0 = 0.0d0
                    xa = 0.0d0
                    ya = 0.0d0
                    za = 0.0d0
                    xb = 0.0d0
                    yb = 0.0d0
                    zb = 0.0d0
                    xc = 0.0d0
                    yc = 0.0d0
                    zc = 0.0d0
c
                    ia = 0
                    ib = 0
c
                    if(iy.eq.2*(iy/2)) then
c
c       when iy is even-numbered
c
                        ipa = (iy+1)*icx*nthm1 + (ix-1)*nthm1
                        ipb = (iy-2)*icx*nthm1 + ix*nthm1
c
                    else
c       when iy is odd-numbered
c
                        ipa = (iy+1)*icx*nthm1 + (ix-1)*nthm1
                        ipb = (iy-2)*icx*nthm1 + (ix-1)*nthm1
                    end if
c
                        do 35 i = 1,nthm1
c
                          if(abs(xyz(3,ip)-xyz(3,ipa +i)).lt.0.6) ia=i
c
                          if(abs(xyz(3,ip)-xyz(3,ipb +i)).lt.0.6) ib=i
c
 35                     continue
c
                    if(ia.eq.0.or.ib.eq.0) goto 33
                    x0 = xyz(1,ip)
                    y0 = xyz(2,ip)
                    z0 = xyz(3,ip)
                    xa = xyz(1,(ipa + ia))
                    ya = xyz(2,(ipa + ia))
```

```
                za = xyz(3,(ipa + ia))
                xb = xyz(1,(ipb + ib))
                yb = xyz(2,(ipb + ib))
                zb = xyz(3,(ipb + ib))
                xc = xyz(1,(ip+2))
                yc = xyz(2,(ip+2))
                zc = xyz(3,(ip+2))
c
                ccc = r(x0,y0,z0,xc,yc,zc)
                if(ccc.gt.4.0) goto 33
c
c       Lattice dimension in Angstom
c
                nl = nl + 1
                abc(1,nl) = r(x0,y0,z0,xa,ya,za)
                abc(2,nl) = r(x0,y0,z0,xb,yb,zb)
                abc(3,nl) = r(x0,y0,z0,xc,yc,zc)
c
                write(8,102) nl,abc(1,nl),abc(2,nl),abc(3,nl)
c
                alpha(nl) = 180.0 - angl(x0,y0,z0,xb,yb,zb,xc,yc,zc)
c
                beta(nl) = 180.0 - angl(x0,y0,z0,xa,ya,za,xc,yc,zc)
c
                gamma(nl) = 180.0 - angl(x0,y0,z0,xb,yb,zb,xa,ya,za)
c
                write(9,*) alpha(nl),beta(nl),gamma(nl)
34      continue
 33           continue
 32       continue
 31   continue
      stop
      end
```

# APPENDIX E

## A FORTRAN SUBROUTINE TO GENERATE ATOM COORDINATES IN INITIAL CRYSTALS

```
c*****************************************************************************************
      subroutine xtal(yc,n,nth,icx,icy,itype)
c
c       Variouble Identification:
c               yc              - a 3-dimenaional array for the Cartesion coordinates of
c                                 carbons (1:9600), hydrogen a (9601:19200), and
c                                 hydrogen b (19201:28800)
c               n               - total number of carbon atoms in the crystal
c               nth             - number of carbons in each chain, z-dimension
c               icx             - number of chains in the x-dimension
c               icy             - number of chains in the y-dimension
c               itype           - type of initial crystal structure
c
c*****************************************************************************************
      implicit real*8(a-h,o-z)
c
      dimension yc(3,29000)
      dimension xyd(3,10000)
c
c               Choose crystal type
c
        if (itype.eq.111) go to 111
        if (itype.eq.222) go to 222
        if (itype.eq.333) go to 333
c
c********
c Block 1: Extended chain
c********
        write(10,*) ' extended  chain  '
c
        yc(1, 1) = -0.4287
        yc(2, 1) =  0.0
        yc(3, 1) =   -0.5*float(n)*1.2685
c
        yc(1, 2) = 0.4287
        yc(2, 2) = 0.0
        yc(3, 2) = yc(3,1)  +   1.268502144
c
        do 34 ip=3,n
c
           yc(1,ip) = yc(1,ip-2)
           yc(2,ip) = yc(2,ip-2)
           yc(3,ip) = yc(3,ip-1) + 1.268502144
c
 34     continue
```

```
c
          go to 999
c
c*********
c Block 2: Monoclinic crystal
c*********
c
  111     continue
c
          write(10,*) ' monoclinic '
c
c                     a => x
c                     b => y
c                     c => z
c
          a = 4.1
          b = 4.8
c
          ip = 0
c
          do 100 iy=1,icy
c
             aoff = 0.0
             if (iy.eq.2*(iy/2)) aoff = 1.5
c
             do 110 ix=1,icx
c
                 coff = 0.0
c
                    do 120 ia=1,nth
c
                       ip = ip + 1
c
                       xyd(1,ip) = a*float(ix-1-icx/2) + aoff
                       xyd(2,ip) = sqrt(b**2 - 1.5**2)*float(iy-1-icy/2)
                       xyd(3,ip) = coff
c
 120                continue
 110         continue
 100      continue
c
      ip = 0
c
          do 130 iy=1,icy
             do 132 ix=1,icx
c
             if (ix.eq.2*(ix/2)) then
c
                 ip = ip + 1
c
                 yc(1,ip) =  0.0
```

```
                yc(2,ip) =  -0.4287
                yc(3,ip) = 0.0
c
                ip = ip + 1
c
                yc(1,ip) = 0.0
                yc(2,ip) = 0.4287
                yc(3,ip) = 1.268502144
c
            else
c
                ip = ip + 1
c
                yc(1,ip) =  0.0
                yc(2,ip) =  0.4287
                yc(3,ip) = 0.0
c
                ip = ip + 1
c
                yc(1,ip) = 0.0
                yc(2,ip) = -0.4287
                yc(3,ip) = 1.268502144
c
            endif
c
                do 134 ia=3,nth
c
                    ip = ip + 1
c
                    yc(1,ip) = yc(1,ip-2)
                    yc(2,ip) = yc(2,ip-2)
                    yc(3,ip) = yc(3,ip-1) + 1.268502144
 134            continue
 132        continue
 130    continue
c
        do 138 ip=1,n
           yc(1,ip) = yc(1,ip) + xyd(1,ip)
           yc(2,ip) = yc(2,ip) + xyd(2,ip)
           yc(3,ip) = yc(3,ip) + xyd(3,ip)  - 0.5*float(nth)*1.26
 138    continue
c
        go to 999
c
c*********
c Block 3: Orthorhomic crystal
c*********
 222    continue
c
        write(10,*) ' orthorhombic '
c
```

```
c                   a => x
c                   b => y
c                   c => z
c
        a = 7.4
        b = 4.9
c
        ip = 0
c
        sign = 1.0
c
        do 200 iy=1,icy
c
           sign = -sign
c
           aoff = 0.0
           if (iy.eq.2*(iy/2)) aoff = a/2.0
c
                do 210 ix=1,icx
                   do 220 ia=1,nth
c
                      ip = ip + 1
c
                      xyd(1,ip) = a*float(ix-1-icx/2) + aoff
                      xyd(2,ip) = 0.5*b*float(iy-1-icy/2)
                      xyd(3,ip) = sign
c
 220                continue
 210             continue
 200     continue
c
        ip = 0
c
        do 230 iy=1,icy
           do 232 ix=1,icx
c
              ip = ip + 1
c
              yc(1,ip) = -0.3031
              yc(2,ip) = -0.3031
              yc(3,ip) = 0.0
c
              ip = ip + 1
c
              yc(1,ip) = 0.3031
              yc(2,ip) = 0.3031
              yc(3,ip) = 1.268502144
c
                 do 234 ia=3,nth
c
                    ip = ip + 1
```

```
c
                        yc(1,ip) = yc(1,ip-2)
                        yc(2,ip) = yc(2,ip-2)
                        yc(3,ip) = yc(3,ip-1) + 1.268502144
c
 234                 continue
 232            continue
 230        continue
c
            do 238 ip=1,n
               yc(1,ip) = yc(1,ip)*xyd(3,ip) + xyd(1,ip)
               yc(2,ip) = yc(2,ip)           + xyd(2,ip)
               yc(3,ip) = yc(3,ip) - 0.5*float(nth)*1.26
 238        continue
c
            go to 999
c
c*********
c Block 4: Hexagonal Cryatal
c*********
c
 333        continue
c
            write(10,*) ' hexagonal '
c
c                       a => x
c                       b => y
c                       c => z
c
            a = 4.8
            b = 8.314
c
c
            ip = 0
c
            sign = 1.0
c
            do 300 iy=1,icy
c
               sign = -sign
c
               aoff = 0.0
               if (iy.eq.2*(iy/2)) aoff = a/2.0
c
                   do 310 ix=1,icx
                      do 320 ia=1,nth
c
                         ip = ip + 1
                         xyd(1,ip) = a*float(ix-1-icx/2)  +  aoff
                         xyd(2,ip) = 0.5*b*float(iy-1-icy/2)
                         xyd(3,ip) = sign
```

```
c
 320                continue
 310             continue
 300     continue
c
         ip = 0
c
         do 330 iy=1,icy
            do 332 ix=1,icx
c
            ip = ip + 1
c
            yc(1,ip) = -0.3031
            yc(2,ip) = -0.3031
            yc(3,ip) = 0.0
c
            ip = ip + 1
c
            yc(1,ip) = 0.3031
            yc(2,ip) = 0.3031
            yc(3,ip) = 1.268502144
c
                do 334 ia=3,nth
c
                   ip = ip + 1
c
                   yc(1,ip) = yc(1,ip-2)
                   yc(2,ip) = yc(2,ip-2)
                   yc(3,ip) = yc(3,ip-1) + 1.268502144
c
 334            continue
 332         continue
 330     continue
c
         pi = 3.141592654d0
         twopi = 2.0d0 * pi
         ip = 0
         do 336 i336 = 1,n,nth
            ang = twopi*(ran(1234567) - pi)
            do 337 i337 = 1,nth
                ip = ip + 1
                yc1=yc(1,ip)
                yc2=yc(2,ip)
                yc(1,ip) = cos(ang) * yc1- sin(ang) * yc2
                yc(2,ip) = sin(ang) * yc1 + cos(ang) * yc2
 337        continue
 336     continue
c
         do 338 ip=1,n
            yc(1,ip) = yc(1,ip) + xyd(1,ip)
            yc(2,ip) = yc(2,ip)           + xyd(2,ip)
```

```
            yc(3,ip) = yc(3,ip) - 0.5*float(nth)*1.26
 338      continue
c
 999      continue
c
c*********
c Block 5: Adding hydrogens to carbons
c*********
c
          call hydrogen(yc,n,nth,icx,icy)
c
          return
          end
c
c*************************************************************
c
      subroutine hydrogen(yc,n,nth,icx,icy)
c
c*************************************************************
c
          implicit real*8 (a-h,o-z)
          dimension yc(3,29000)
c
c      C-H bond length = 1.069, H-C-H bond angle = 107 degree. (Polymer Handbook
c      1989)
c
          xa(pi,ra0,r20,x0,y0,z0,x2,y2,z2) =
         1   ra0*(sin(1.311111*pi)*(y2-y0)/(r20*sqrt(1-(z2-z0)**2/r20**2))
         2   +cos(1.311111*pi)*(x2-x0)/(r20*sqrt(1-(z2-z0)**2/r20**2)))+x0
c
          ya(pi,ra0,r20,x0,y0,z0,x2,y2,z2) =
         1  -ra0*(sin(1.311111*pi)*(x2-x0)/(r20*sqrt(1-(z2-z0)**2/r20**2))
         2  -cos(1.311111*pi)*(y2-y0)/(r20*sqrt(1-(z2-z0)**2/r20**2)))+y0
c
          xb(pi,rb0,r20,x0,y0,z0,x2,y2,z2) =
         1  rb0*(sin(0.69*pi)*(y2-y0)/(r20*sqrt(1-(z2-z0)**2/r20**2))+cos
         2  (0.69*pi)*(x2-x0)/(r20*sqrt(1-(z2-z0)**2/r20**2)))+x0
c
          yb(pi,rb0,r20,x0,y0,z0,x2,y2,z2) =
         1  -rb0*(sin(0.69*pi)*(x2-x0)/(r20*sqrt(1-(z2-z0)**2/r20**2))-cos
         2  (0.69*PI)*(Y2-Y0)/(R20*SQRT(1-(Z2-Z0)**2/R20**2)))+Y0
c
c
          pi = 3.1416e0
          ra0 = 1.069e0
          rb0 = 1.069e0
          r10 = 1.53e0
          r20 = 1.53e0
```

```
c*****************************************************************************
c
c      C1   Hb        Method C: Spherical coordinate approach with coordinates
c       \ /          transformation: translation, origin at C0; rotation,
c        C0           hydrogen a and b are on local x-y plane while carbons
c       / \          are on the plane normal to x-y plane.
c     C2    Ha        Bonding parameters from POLYMER HANDBOOK (1989)
c
c  ra0 and rb0 are C-H bond-lengths, r20 is bond-length of C2-C0 and r10 for
c  that of C1-C0 which are subjected to change at time being non-zero
c
c*****************************************************************************
c
        do 678 ip = 1, n
c
           if(mod(ip,nth).ne.0) then
c
           yc(1,n+ip) = xa(pi,ra0,r20,yc(1,ip),yc(2,ip),yc(3,ip),
     1       yc(1,ip+1),yc(2,ip+1),yc(3,ip+1))
           yc(2,n+ip) = ya(pi,ra0,r20,yc(1,ip),yc(2,ip),yc(3,ip),
     1       yc(1,ip+1),yc(2,ip+1),yc(3,ip+1))
           yc(3,n+ip) = yc(3,ip)
c
           yc(1,2*n+ip) = xb(pi,rb0,r20,yc(1,ip),yc(2,ip),yc(3,ip),
     1       yc(1,ip+1),yc(2,ip+1),yc(3,ip+1))
           yc(2,2*n+ip) = yb(pi,rb0,r20,yc(1,ip),yc(2,ip),yc(3,ip),
     1       yc(1,ip+1),yc(2,ip+1),yc(3,ip+1))
           yc(3,2*n+ip) = yc(3,ip)
c
           else
c
           yc(1,n+ip) = xa(pi,ra0,r10,yc(1,ip),yc(2,ip),yc(3,ip),
     1       yc(1,ip-1),yc(2,ip-1),yc(3,ip-1))
           yc(2,n+ip) = ya(pi,ra0,r10,yc(1,ip),yc(2,ip),yc(3,ip),
     1       yc(1,ip-1),yc(2,ip-1),yc(3,ip-1))
           yc(3,n+ip) = yc(3,ip)
c
           yc(1,2*n+ip) = xb(pi,rb0,r10,yc(1,ip),yc(2,ip),yc(3,ip),
     1       yc(1,ip-1),yc(2,ip-1),yc(3,ip-1))
           yc(2,2*n+ip) = yb(pi,rb0,r10,yc(1,ip),yc(2,ip),yc(3,ip),
     1       yc(1,ip-1),yc(2,ip-1),yc(3,ip-1))
           yc(3,2*n+ip) = yc(3,ip)
c
           endif
c
 678    continue
        return
        end
```

# VITA

Guanghe "Luke" Liang was born on October 23, 1956 in Fujian China. He received his B.S. degree in Chemistry in January 1982 and M. S. degree in Polymer Science in January 1985 both from Fujian Normal University. From January 1985 to March 1987, he served as a full-time instructor in th Institute of Polymer Science, Fujian Normal University. In March 1987, he entered the University of Tennessee at Knoxville studying Polymer Engineering for six months, then he joined the graduate program in the Chemistry Department of the University of Tennessee at Knoxville working on polymer synthesis for three years, where he received his second M. S. degree in Chemistry in May 1990. He continued his study at the University of Tennessee at Knoxville where he found strong interest in molecular dynamics simulations of polymers and expects his Ph.D. in polymer chemistry in 1993.

He decided to continue his research in the fields of polymer science and molecular modeling after completing the degree requirements.